PhD thesis

Physical and numerical modelling of subaerial landslide generated waves

Andrea Panizzo

March 2004

Acknowledgements

This work was funded by the National Dam Office of the Italian Government (Registro Italiano Dighe, Presidenza del Consiglio dei Ministri, Servizi Tecnici Nazionali). Thanks are due to A. Petaccia, chief of the National Dam Hydraulic Office, and to A. Maistri, for the many useful discussions.

I would like to thank my advisor Prof. Paolo De Girolamo, who conceived and supervised this research. I am deeply grateful for his guidance and, above all, for his true friendship which significantly helped me in moments of health and scientific difficulties. Thanks to him, now I am a better scientist and man.

I also want to thank Prof A. Noli for the many useful discussion and for introducing me in the research field of Coastal Engineering. I am proud to be one of his students.

Prof. Robert A. Dalrymple is gratefully acknowledged for the visiting period I could spend working with him at the Johns Hopkins University of Baltimore, MD, USA. The excellence he demonstrates in the field of Coastal Engineering, and in the research on the SPH numerical model, gives me the will to keep working on these topics. I was really fortunate meeting him in my life.

I would also like to thank Eng. G. Bellotti and Eng. M. Di Risio, who were always available to discuss the research. Eng. S. Melotti is gratefully acknowledged for helping me performing the physical experiments. They are more than friends.

Thanks are also due to laboratory technicians Mario Nardi and Lucio Matergia. Their excellence in realizing hydraulic physical models was more than appreciated during three years of experimental studies.

I would like to thank also G. Di Carlo, who helped me to run my SPH code on parallel computer systems. Prof. P. Sammarco is gratefully acknowledged for carefully reading this manuscript.

Background lifestyle is an essential component in a three years PhD research, and I have to thank my mother and my father, who always give an unconditional support in everything I do. Difficulties are sometimes part of human life, but I will always know they are *here* with me. This work is dedicated to them.

Abstract

Water waves generated by subaerial landslides are dangerous "tsunamis" events involving the safety of human communities living along ocean coasts or near an artificial reservoir. Starting from results presented by past studies, this work is intended to provide a characterization of subaerial landslide generated waves employing both physical and numerical models.

Experiments carried out on a two dimensional model are used to gain new insights on the dispersive features of subaerial landslide generated waves by means of the Wavelet Transform analysis of wave records. Observations from a three dimensional model are analyzed with the aim of defining formulations forecasting the principal features of the generated impulse waves as a function of the principal features of the landslide. Formulations show a good fit with experimental data, and the application to case studies demonstrate that they can be used in real cases with a satisfactorily accuracy.

The SPH numerical model is considered and implemented to simulate subaerial landslide generated waves. A parallel version of the original SPH algorithm is presented, implementing new computational strategies which optimize the performances of the model. SPH is applied to reproduce physical experiments carried out on a two dimensional model. Water flow fields simulated by the code agree well with considered experiments, showing very satisfactory results.

Contents

List of Figures

List of Tables

Chapter 1

Introduction

Tsunamis are large water waves triggered by a sudden disturbance of the ocean floor or the ocean surface, which is usually caused by earthquakes, landslides or volcanic eruptions. The word tsunamis comes from the Japanese, with the meaning "harbor wave", and is related to the excitation of harbors seiches induced by the large tsunamis wavelengths. Both energy and momentum can take tsunamis waves thousands of kilometers across open ocean, carrying destruction on far shores hours after the impulse generating event. In deep water conditions, they can travel at speeds of 600-800 kilometers per hour, presenting wave heights of the order of some centimeters, wavelengths of the order of hundreds of kilometers, while the wave period can vary from minutes to hours. This is why tsunamis are usually not detected in open seas. As a tsunamis approaches shallow water near a coast, it reduces the wave celerity and significantly increases the wave height, sometimes exceeding the value of 20 meters and thus becoming very destructive and dangerous for coastal communities.

Tsunamis waves have largely occurred in the Pacific Ocean, however very dangerous events have been also registered in the Mediterranean sea, such as that occurred the July 21th, AD 365, at Alexandria, which caused 50.000 deaths, and that one occurred the December 28th, 1908, at Messina, which caused 120.000 deaths. Regarding the Mediterranean sea, it is worth mentioning the very recent event occurred at the Stromboli volcano, on December 30, 2002. No human lives were lost, but the wave damaged properties along the shorelines of the Stromboli island and excited resonant modes of harbors along the coasts of Calabria.

Waves generated by subaerial landslides are a particular type of tsunamis waves. They are generated by landslide events in artificial reservoirs (Vajont valley, Italy, 1963) or natural lakes, or they are triggered by landslides occurring on sea shorelines (Lituya Bay, Alaska, 1958; Stromboli volcano, Italy, 2002). In these cases, differently from tsunamis waves trig-

gered by underwater mass movements, splashes and complex three dimensional water flows are generated close to the impact area. Then, the perturbation travels for long distances if in oceanic areas, causing disasters far away from the generation area, producing high wave runups on shorelines. In the case of artificial reservoirs the most dramatic consequences are the dam overtopping and the seiching waves of the basin. Sometimes landslide events in artificial reservoirs may be triggered by the filling up of the artificial reservoir itself, by virtue of the induced change in watershed. At present, in artificial basins where landslide risk exists, the water is kept well below the maximum possible level to minimize risk. As a consequence the dam and the basin potentialities are underutilized, causing great economic losses.

The understanding and the forecasting of landslide generated waves is important both for the safety of people and properties which are close to the reservoir or along sea shorelines, and for artificial reservoir and dam management. Past studies carried out on this topic presented mathematical theories (Stoker, 1957; Prins, 1958; Kranzer and Keller, 1960; Pezzoli, 1966, 1972; Le Méhauté and Wang, 1996), physical model experiments (Wiegel, 1955; Wiegel et al., 1970; Kamphuis and Bowering, 1972; Huber and Hager, 1997; Walder et al., 2003) and numerical simulations (Heinrich, 1992; Watts, 1997; Monaghan and Kos, 2000; Monaghan et al., 2003). However, despite this body of work, at present time no general method is available to accurately predict landslides generated waves.
The aim of the present work is to glean new insights in the characterization of subaerial landslide generated waves, on the basis of both physical and numerical models grounds. Physical model experiments have been carried out in order to reproduce and quantify the landslide generated waves principal features, using both two and three dimensional models. Data analyses from the physical model experiments have been used to understand the impulse wave nature and to define forecasting formulations able to predict their features while propagating in a three dimensional water body. Then, a numerical model has been implemented with the aim to gain insights from direct simulations and reproduce possible real different scenarios.

1.1 Physical evidences

The generation of impulse waves due to the impact of a subaerial landslide with water is a complex phenomenon, involving several physical aspects. Huber (1997) proposed a simplification of the considered phenomenon, individuating four distinct phases. With reference to Figure 1.1, at first (circle 1 in the Figure) the landslide starts moving, accelerates and then falls into water. The characterization and the forecasting of a landslide mechanism is a very

complex task, involving lots of different aspects and physical variables. The study of this part of the impulse waves generation process lies in the scientific field of geology and soil mechanics, and is not going to be treated in the present work. Step 2 sketches the impact of the landslide with water. This part of the process is at the bases of waves generation, due to the energy exchange mechanism between the landslide and the water. The principal landslide parameters, such as its volume, impact velocity, density, porosity, shape of the front, slope inclination angle, influence the features of the subsequent water wave motion. In phase 3 impulse waves propagate in the reservoir or in the open sea, presenting a wave energy dispersion which is both longitudinal and directional. Waves features change as a function of the water depth, and refraction, diffraction and shoaling may occur. Finally, phase 4 is related to the impulse wave interaction with shorelines or dams. The impulse wave runup may cause the flood of coastal areas, and, in the case of an artificial reservoir, the dam can be overtopped thus flooding downstream areas. Usually, seiches waves of the artificial water basin are also triggered.

As far as the generated water waves are concerned, they may present very different shapes and dispersive features. Prins (1958), Wiegel et al. (1970) and Noda (1970) performed several physical experiments generating impulse waves by the falling of a solid block in a two dimensional wave flume. They concluded that, depending on the local water depth, the energy exchange between the landslide and the water, and the landslide volume, impact waves present different characteristics. Their experimental observation can be summarized by Figure 1.2, which presents a map of different wave types observed during impulse waves generation due to the vertical fall of a box (λ is the box width, d is the local water depth, $Fr = v/\sqrt{gd}$ is the dimensionless box falling velocity). The typical time series of water surface elevation at a given point are represented on the right part of Figure 1.2. Basically four types of impact waves were observed by these authors: (A) leading wave with oscillatory wave characteristics, (B–C) leading wave with solitary wave characteristics, followed by a trough connecting it with the dispersive wave pattern, (D–E) leading wave being a single wave with solitary wave characteristics, separated by the dispersive wave pattern, (F) solitary wave with complex form (bore in the first stage). As a general rule the generated waves type vary from (A) to (F) gradually as the values of λ/d and Fr increase. When the dimensions of the falling body are large in comparison to water depth, solitary waves are to be expected, vice versa a train of dispersive waves is likely to be generated in relatively deep water.

In view of the above observations, the characterization of subaerial landslide generated

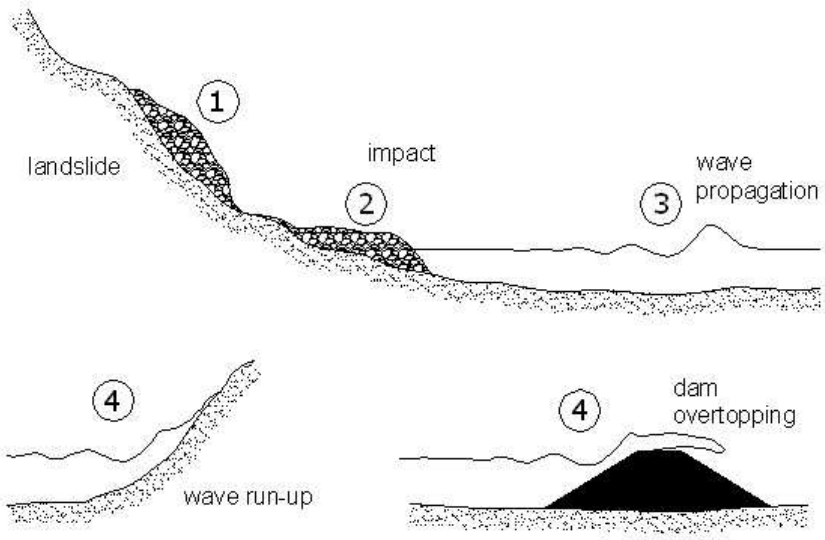

Figure 1.1: Principal phases in the phenomenon of subaerial landslide generated waves.

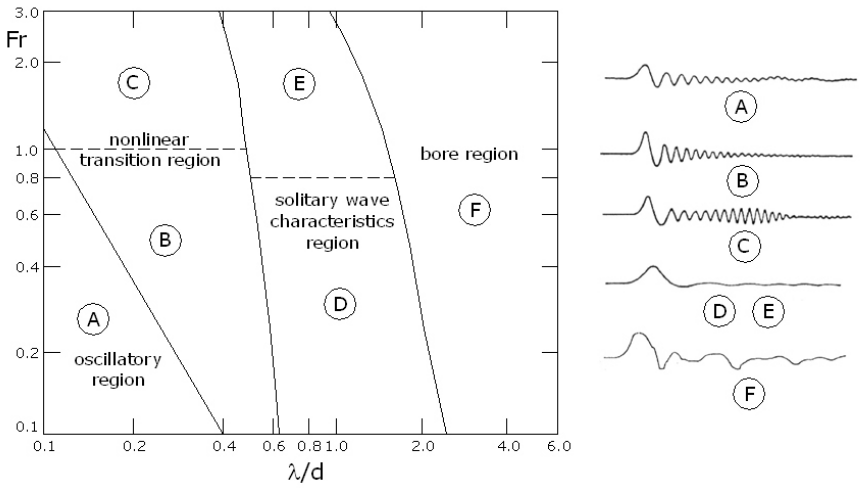

Figure 1.2: Different types of impulse waves defined as function of the landslide volume, represented by the dimensionless parameter λ/d, and the landslide velocity, represented by the Froud number Fr (picture taken from Noda, 1970).

water waves, which is the aim of the present work, has to be carried out making simplifying assumptions about the landslide principal parameters. Referring to Watts' works (Watts, 1997, 1998, 2000; Watts et al., 2001; Walder et al., 2003), the water wave field can be recognized to change from the *near field*, where the water motion is complex and three dimensional,

presenting splashes and bores, to the *far field*, where the water motion is dominated by propagating water waves, which can be classified within one of the four introduced types. Some further considerations can be made on the expected general aspects of the phenomenon considering the ratio between the volume of the landslide and that of the water body where the impulse flow takes place. Basically, three different cases may be recognized to exist. The first case (see panel A of Figure 1.3) is the case of a large landslide falling into a small reservoir: in this limit case the far-field may not exist. The second, intermediate case (panel B of Figure 1.3) consists of near and far-field of comparable extents, i.e. their dimensions having the same order of magnitude. In the last case (panel C on Figure 1.3) the far-field extension is several times the extension of the near-field. This is the case of small landslides falling into large reservoirs or into the sea.

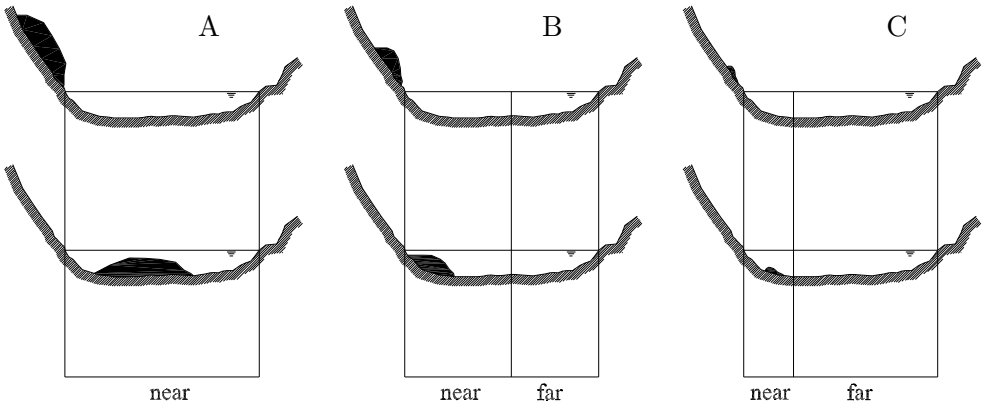

Figure 1.3: Three different main cases defined as a function of the ratio between the volume of the landslide and that of the water body.

So, it is important to consider which could be the dominant aspects of the phenomenon before modelling subaerial landslide generated waves. For example, when designing a physical model, the experimental facility has to be made in order to simulate the aspects of interests, employing landslide and waves measurement systems able to correctly describe the reproduced phenomenon. Similarly when numerical modelling is pursued, the choice of the proper model to implement is a very delicate point, as it can be a three dimensional model (such as the mesh–free Smoothed Particle Hydrodynamics - SPH) if the interest is on reproduction of the near field dynamics, or a wave propagation model (such as those based on Nonlinear Shallow Water Equations), if it is on the far field wave oscillation dynamics.
In the present work, physical experiments for the study of impulse waves propagating in

the near field and part of the far field are considered, while the SPH numerical approach is considered to model the near field wave generation.

1.2 Literature review

The interest of the scientific community in the study of subaerial landslide generated waves increased after some tragic events occurred in the middle of the last century (Lituya bay, Alaska, 1958; Vajont valley, Italy, 1963). Before those events, several studies had been conducted on the topic of the "water entry problem", with the task of modelling the flow field generated close to a body entering into water. Subsequently, the study of water waves generated by bodies falling into water was also faced. This section summarizes the principal works which can be found in subaerial landslide generated waves literature.

Wiegel (Wiegel, 1955; Wiegel et al., 1970) was one of the first coastal engineers interested in waves generated by subaerial landslide. He performed a series of experiments by releasing solid block landslides in a wave flume of constant depth. Solid blocks had different sizes, shapes, densities, submergences and were thrown into water along an incline which was 22° to 54° from horizontal. The experimental results showed that the wave amplitude increased with increasing block density, decreasing with initial block submergence, and increasing with incline angle. It was found that wave period increased with increasing the length of the submerged block. Moreover, Wiegel confirmed results obtained by Prins (1958) using a very similar experiment, identifying four different types of impulsively generated waves as a function of both the non dimensional initial block submergence and the non dimensional block length.

Kamphuis and Bowering (1972) performed a series of experiments in a wave channel, generating impulse waves by releasing solid block subaerial landslide models rolling down an inclined ramp. The experiments were conceived to have as little simplification as possible. Landslides were modelled using a solid tray with zero porosity. The front slope of the tray and the angle of the ramp with horizontal were adjustable. Different channel depths, landslide sizes, impact velocities, inclinations of both the ramp and the landslide front with the horizontal were considered in the experiments. Results were used to define a forecasting formulation for waves propagating in a two dimensional water body, and showed that impulse wave characteristics depend mainly on the slide volume and the impact velocity with water. Tests performed by Kamphuis and Bowering did not give a definitive answer but suggested

a valid method of investigation.

Huber and Hager (Huber, 1982, 1997; Huber and Hager, 1997) carried out a three dimensional experiment by considering granular landslide falling into a water tank. A forecasting formula, predicting the non dimensional wave height as a function of the landslide main parameters, the basin water depth, and the distance from the impact point, was set up on the basis of experimental results. As Huber and Hager considered very high impact velocities, the generated wave height was not expressed as a function of the impact Froude number (as in Kamphuis and Bowering study) but it depended mainly by the values of the non dimensional landslide volume. Moreover, results showed that the landslide density plays a minor role in the generation mechanism. The Authors found that the proposed forecasting formula presents a low approximation with experimental data, with errors up to the 30 %. Anyway, it is to be stressed that so far, Huber and Hager formula is the only available engineering forecasting tool for subaerial landslide generated waves.

Tinti (Tinti et al., 1994; Tinti and Maramai, 1996; Tinti et al., 1999) presented the application of two distinct numerical models reproducing the motion of a granular landslide and the subsequent wave propagation. The former was conceived on the basis of a lagrangian approach simulating the landslide falling down into water. The latter was based on shallow water wave equations, developed using a finite element numerical scheme. Some of his works dealt about tsunamis waves generation and propagation at the Stromboli volcano (Italy) due to the falling into water of solidified magma descending down the "Sciara del Fuoco" slope, which is a frequent event in Stromboli (f.i., December 30, 2003, tsunamis event).

Watts, after being interested in underwater landslide generated waves (Watts, 1997, 1998, 2000), characterized subaerial landslide generated waves (Walder et al., 2003) using a theoretical analysis based on non dimensional equations of the water flow and conducting two dimensional physical experiments. He highlighted the need for a tool to forecast the water elevation as a function of given realistic landslide motion. Indeed, his works constitute a continuation of Hammack's study (Hammack, 1973) on tsunamis waves generated by a given motion of a wavemaker landslide.

Monaghan and Kos (2000) and Monaghan et al. (2003) presented the application of a powerful numerical model, the lagrangian Smoothed Particle Hydrodynamics (SPH), to wave motion generated by impacts in a two dimensional water context. In particular, Monaghan

and Kos (2000) presented the modelling of the "Scott Russel wave generator", which is a weighted box falling vertically into water, while Monaghan et al. (2003) presented the modelling of the solid-liquid interaction of a solid block sliding down an inclined ramp. The SPH approach overcomes the limits of mathematical theories (Hammack, 1973; Watts, 1997) in the modelling of the near field excited by the falling of a subaerial landslide, which presents splashes, breaking waves and complex three dimensional water flows. Results from the work of Monaghan and Kos (2000) and Monaghan et al. (2003) showed a very satisfactorily agreement between numerical simulations and physical experiments.

1.3 Aims of the present work

Despite the large body of work introduced in the previous section, the battlefield of landslide generated waves modelling is still open to lots of solutions and improvements.
Considering experimental work found in the literature, at present time the only engineering tool to forecast in a simple and meaningful way subaerial landslide generated waves propagating in a three dimensional water body is the one proposed by Huber and Hager (1997). However, the fit of their formulation with their experimental data is low (Huber and Hager, 1997), while value of the landslide impact velocity with water is not taken into account, and few available experimental details can't provide information to reproduce their study. So, the first aim of the present work is to define a simple to use, meaningful and accurate engineering tool to forecast subaerial landslide generated waves propagating in a three dimensional water body. It is shown that the interpretation of experimental results also requires the development and application of modern techniques of data analysis, such as the Wavelet Transform (WT) and Artificial Neural Networks (ANN) analyses. The present work is going to introduce the applications of both the WT analysis and the ANN approach to experimental data, which constitute novel contributions to gain new insights in the considered phenomenon. Moreover, new formulations forecasting the principal features of subaerial landslide generated waves are here defined on the basis of experiments carried out on purpose. Defined formulations are compared to works of Kamphuis and Bowering (1972) and Huber and Hager (1997), and then applied to selected case studies.
The second aim of the present work is to individuate, implement and apply a numerical model able to provide detailed simulations of water waves generated by subaerial landslides. Past studies employing pure mathematical approaches showed limited success due to the intrinsic difficulty in properly simulating splashes, bores, and solid-liquid interaction. So, considering

results presented by Monaghan and Kos (2000) and Monaghan et al. (2003), the lagrangian Smoothed Particle Hydrodynamics (SPH) numerical model has been implemented. A new computational strategy to solve the problem of neighbor particles research is proposed in the present work, with the aim of reducing the wasting of computational time. Moreover, the SPH numerical model has been implemented using the OpenMP numerical libraries for parallel machines with shared memory architecture, and is currently running on an IBM supercomputer with 8 CPUs. In the present thesis, SPH simulations of landslide generated water waves are compared to laboratory two dimensional experiments, showing very satisfactorily agreements.

1.4 Thesis outline

In the followings, Chapter 2 provides an overview on the employed physical models simulating subaerial landslide generated waves. The experimental facilities used in the present studies are fully described.
Chapter 3 describes the methods of analysis used for the interpretation of experimental data, along with obtained results. A Wavelet Transform Analysis numerical code was implemented in order to characterize the transient aspects of the generated wave trains. An Artificial Neural Network numerical code was implemented to improve the accuracy of the forecasting model. The above mentioned analysis codes were implemented using both the Fortran and the Matlab computer languages.
Chapter 4 presents the details of the SPH numerical model, which was developed in order to get direct simulations of the considered phenomenon. The model was firstly verified by comparing simulations with literature experiments, then it was applied to reproduce the physical model experiments carried out within the present work.
Chapter 6 draws together conclusions and ongoing research.
Appendix A introduces some details about wavelet transform analysis. Appendix B provides details about the Gauss-Newton optimization method, used in the definition of forecasting formulations.

Chapter 2

Physical modelling of landslide generated waves

2.1 Preface

As demonstrated by past studies (Hammack, 1973; Watts, 1997), the principal features of a tsunamis wave can be mainly related to the features of the impulse generating event. So, in real cases a good characterization of the generation mechanism is important for tsunamis forecasting. In the study of landslide generated waves the momentum exchange between the landslide and the water acts as a wavemaker. In real cases, uncertainties are given by physical, rheological and kinematical features of the landslide. Further difficulties arise when the shape of the landslide front, its porosity and density upon impact with water, and the subsequent volume deformation are taken into account. Due to the large number of involved parameters, the present study is intended to provide a characterization of tsunamis waves produced by subaerial landslides with known and simple geometry. The characterization of the landslide kinematic and structural features constitute aims which are out of the purposes of the present work, as they relate more to geology and soil mechanics.

In order to define a formulation which can avoid the effects of the above mentioned uncertainties it is necessary to employ a simplified generation mechanisms. Watts (Watts, 1997, 1998, 2000) demonstrated in detail the role of the underwater landslide motion as a tsunamis *wavemaker*, finding correlations between the time series of the waves oscillations and that of the landslide motion. The assumption of a simplified landslide mechanism can improve the correlation between the water waves and the landslide parameters, thus giving reliability to the characterization of the considered phenomenon. So, in the present work, solid landslide models with zero porosity were employed in all the performed experiments.

The experimental programs of the two and the three dimensional models were defined on the basis of a dimensional analysis of landslide and waves parameters involved in the phenomenon as carried out by Kamphuis and Bowering (1972).

2.2 Description of the two dimensional model

The experimental study carried out using a two dimensional model was intended both to provide benchmark cases for numerical model calibration and to test the proper analysis method to employ in the characterization of subaerial landslide generated waves dispersive features. At the same time, part of the experimental campaign was dedicated to test an overflow structure, which was designed as wave absorbing structure to be set in the three dimensional model wave tank.

So, the realization of a simple model for the simulation of subaerial landslide generated waves in a two dimensional wave flume was firstly faced. The well known "Scott Russel wave generator" (SRWG), which is a box falling vertically into water thus generating impulse waves, was designed and realized in the LIAM laboratory of the DISAT department, at L'Aquila University. The wave flume (see Figures 2.1 and 2.2) was built using a frame of aluminum beams with square section of 0.04 m, while the flume walls and floor were made up of PVC. The flume was 4.00 m long, 0.11 m wide and 0.40 m deep. The boxes of the SRWG were realized in PVC, and their masses were adjusted by putting lead bricks in the box internal chamber. The motion of the box was constrained by vertical guide rails. At the right-end of the flume, at a distance equal to 3.40 m from the left-end, an overflow structure and a vertical fully reflecting wall were used. The first structure (refer to Figure 2.2 for shape and dimensions; β =0.10 m) was used in order to measure and quantify reflected waves and was then employed in the wave tank of the three dimensional model as wave absorbing facility. Surface elevations were measured at several sections of the flume by means of resistance wave gauges. The position of the gauges used in all the experiments is shown in Figure 2.1, where their names and distances from the left-end of the flume are summarized. Wave gauges signals were amplified in the range $\pm$10 Volts and then acquired by a 16 channels National Instruments analog to digital conversion board. The system of the gauges, the signal amplifier and the NI board introduced an instrumental noise less than 0.01% of the original acquired signals. A Metra–Mess CB41 mono–axial piezoelectric accelerometer, with instrumental noise less than 0.01%, was placed into the falling box in order to obtain, by integration, its trajectory. The water level data covered a time period of 20 seconds with a sampling frequency equal to 50 Hz. The acceleration data were collected for 20 seconds with

a sampling frequency of 1000 Hz. A Canon XM1 Pal digital-video-camcorder (video sensors 3CCD with 300.000 pixels and 25 Hz images acquisition frequency) was used to acquire images of the box falling into the water (see Figure 2.3).
As anticipated before, a dimensional analysis of the physical parameters involved in the problem at hand was carried out in order to individuate the principal variables influencing the considered phenomenon. Following the dimensional analysis presented by Kamphuis and Bowering (1972), in the SRWG model any property of the generated wave, namely A_W, can be expressed as a function of the following physical quantities:

$$A_W = f(V, d, d_1, p, \rho_s, \rho, \mu, r, t) \tag{2.1}$$

With reference to Figure 2.2, V is the volume of the falling box, which is a function of the box length λ, width w and height h, d is the water depth, d_1 is the initial distance between the bottom of the flume and the box base, p is the box porosity, ρ_s is the box density, ρ is the water density, μ is the water dynamic viscosity, r is the distance taken from the left-end side of the flume, and t is the elapsed time.
Eq. (2.1) can be rewritten in dimensionless form considering a length scaling parameter, which was assumed to be the water depth d, such as:

$$\Pi_W = f(\frac{h}{d}, \frac{w}{d}, \frac{\lambda}{d}, \frac{d_1}{d}, p, \frac{\rho_S}{\rho}, \frac{\rho d\sqrt{gd}}{\mu}, \frac{r}{d}, t\sqrt{\frac{g}{d}}) \tag{2.2}$$

where Π_W corresponds to A_W in dimensionless form. Notice that the drop velocity of the box does not directly appear into Equations (2.1) and (2.2) since it can be expressed as a function of:

$$v_{box} = f(\frac{\lambda}{d}, \frac{d_1}{d}, p, \frac{\rho_S}{\rho}, \frac{\rho d\sqrt{gd}}{\mu}) \tag{2.3}$$

Since the aims of the experimental study were both to investigate the features of waves using a proper mean of analysis and to provide test cases for the calibration of the numerical code, the number of physical variables was reduced, and some of them assumed constant values in the experiments. The value of the porosity was fixed to $p = 0.0$ in all the performed experiments, in order to deal with a simplified generation mechanism. The box width and height were fixed respectively to 0.11 m (equal to the channel width) and 0.10 m. Moreover, on the basis of results obtained by Kamphuis and Bowering (1972) and Huber and Hager (1997), the influence of the water viscosity μ was neglected, and consequently the Reynolds number. Thus, eq. (2.2) becomes:

$$\Pi_W = f(\frac{\lambda}{d}, \frac{d_1}{d}, \frac{\rho_S}{\rho}, \frac{r}{d}, t\sqrt{\frac{g}{d}}) \tag{2.4}$$

According to this, the experiments were run varying the length λ of the falling box, the box density ρ_s, the water depth d, and the box immersion $\xi = d_1 - d$, which was considered positive when the box was above the water level.

Referring to the above introduced results of Prins (1958), Wiegel et al. (1970) and Noda (1970), who individuated four different types of impulse waves as a function of the width of the falling box of the SRWG and its velocity when impacting water, different values of λ, d and d_1 were chosen in order to reproduce water oscillations ranging from oscillatory waves to solitary waves. The values imposed to λ, ρ_s, d, and ξ in the experiments with the overflow structure are summarized in Table 2.1; by combining all parameters 27 experiments were carried out. As far as the experiments with the vertical wall are concerned, 108 tests were performed by varying the parameters as indicated in Table 2.2. Notice that the box mass, rather than box density, is reported in tables.
Figures 2.3, 2.4 and 2.5 present pictures from the movies recorded during some of the experiments, showing the impact of the box with the water, the splash and the flow field generated in the $near field$, and part of the first impulse wave propagating toward the far field.

Figure 2.6 reports the time series, reconstructed by integration from the acceleration time series, of the parameter d_1.

Box length λ (m)	Water depth d (m)	Box immersion ξ (m)	Box mass (kg)
0.05	0.23	0.03	2.0
0.10		0.00	1.5
0.15		-0.03	1.0

Table 2.1: Two dimensional model experiment. Values of the parameters in the experiments with the overflow structure at the right-end of the flume.

Box length λ (m)	Water depth d (m)	Box immersion ξ (m)	Box mass (kg)
0.05	0.23	0.03	2
0.10	0.18	0.00	1.5
0.15	0.10	-0.03	1.0
	0.06		

Table 2.2: Two dimensional model experiment. Values of the parameters in the experiments with the vertical wall at the right-end of the flume.

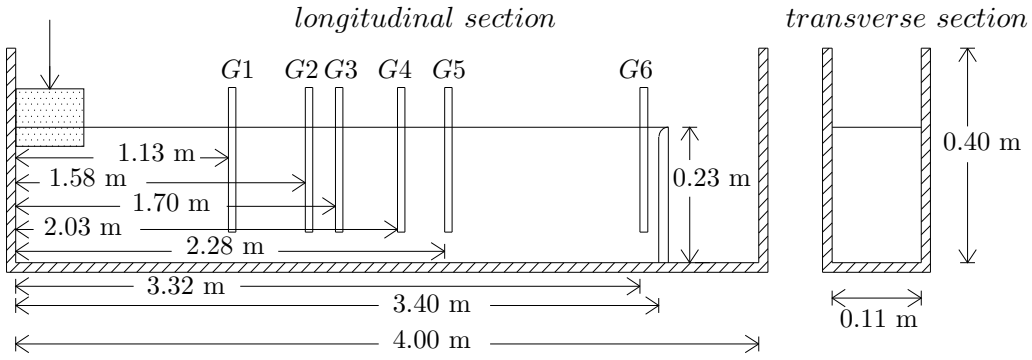

Figure 2.1: Wave flume dimensions and gauges name and positions. At the right-end of the flume the overflow structure is shown.

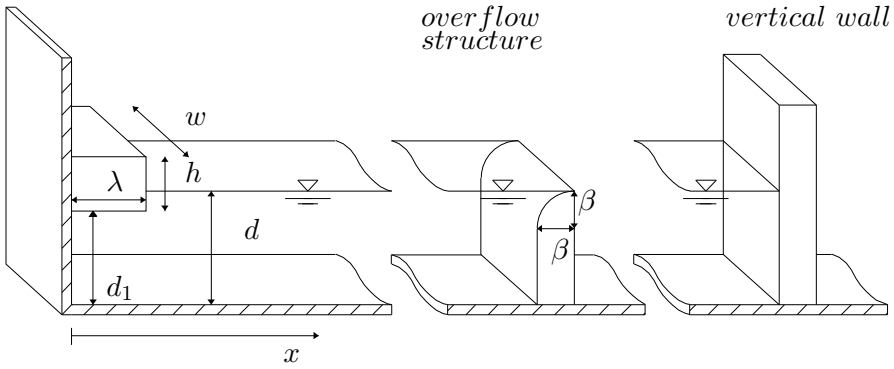

Figure 2.2: Sketch of the two dimensional experiment showing the box falling in the wave flume, the overflow structure and the vertical reflecting wall put at the right end of the flume.

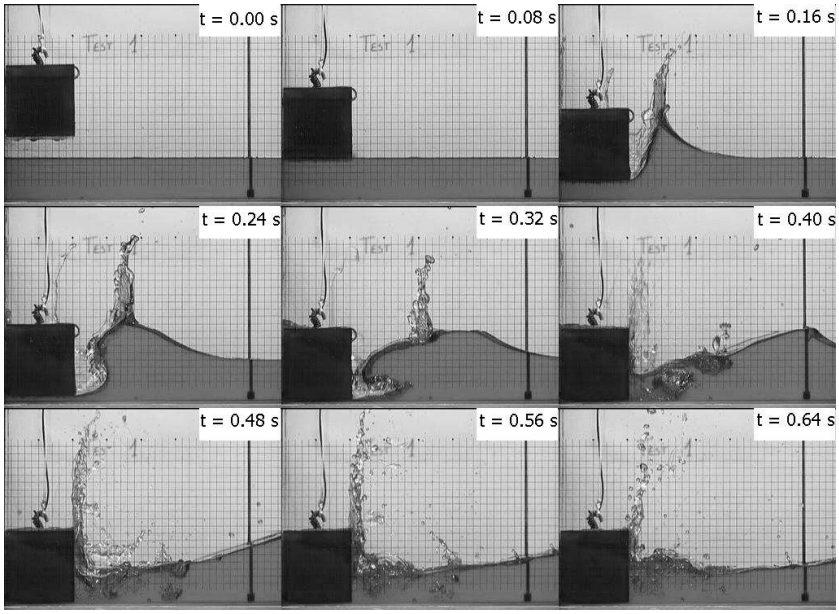

Figure 2.3: Sequence of frames showing one of the performed experiments. In this case $\lambda =$ 0.10 m; d = 0.06 m; $\xi = 0.03$ m; box mass equal to 1.5 Kg.

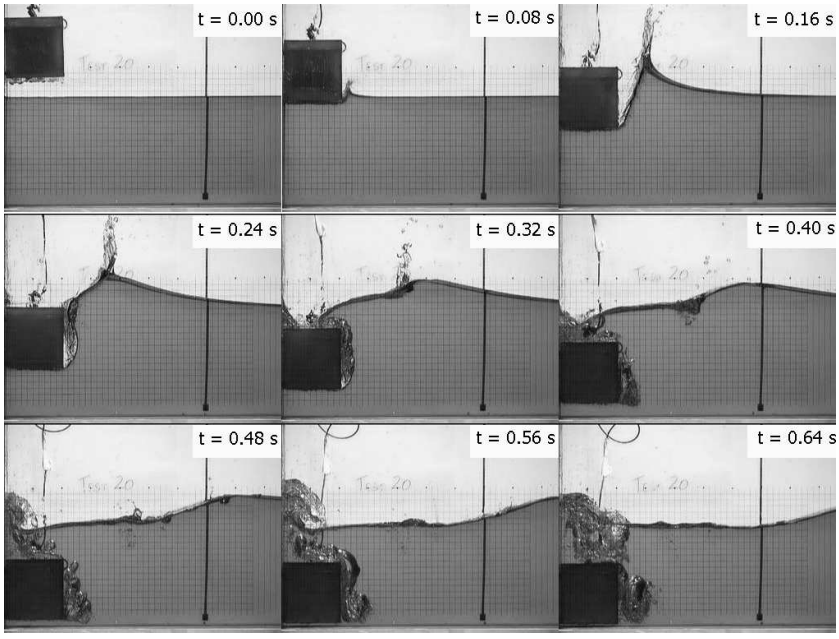

Figure 2.4: Sequence of frames showing one of the performed experiments. In this case $\lambda =$ 0.10 m; d = 0.18 m; $\xi = 0.03$ m; box mass equal to 1.5 Kg.

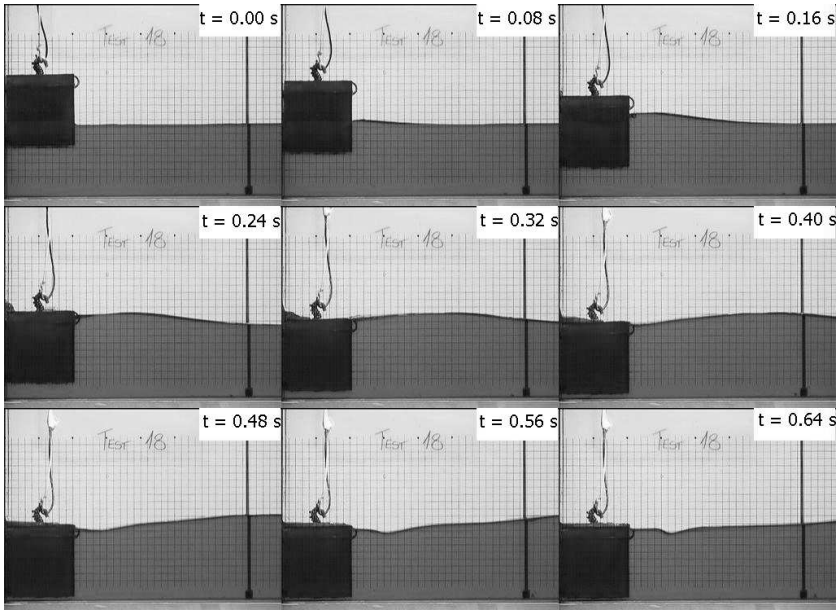

Figure 2.5: Sequence of frames showing one of the performed experiments. In this case λ = 0.10 m; d = 0.10 m; ξ = -0.03 m; box mass equal to 1.5 Kg.

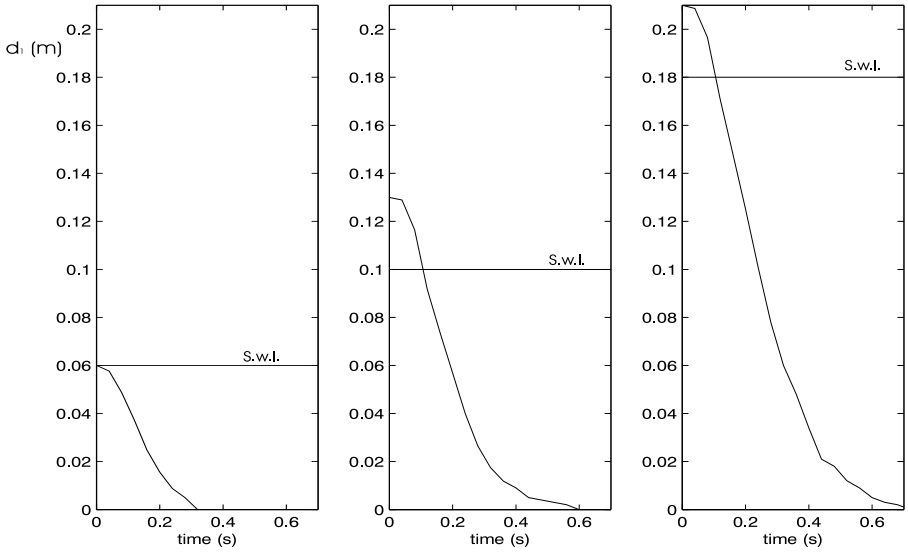

Figure 2.6: Time series of parameter d_1 (distance between the box base and the flume bottom). Left panel refers to an experiment with d=0.06 m and ξ = 0.0 m, central and right panels refer to d=0.10 m and ξ = 0.03 m, d=0.18 m and ξ = 0.03 m respectively. The box mass was equal to 1.5 Kg in all the represented experiments. The horizontal lines sketch the still water level.

2.3 Description of the three dimensional model

The study on the three dimensional model was carried out in order to define predicting formulations for the main parameters of impulse waves as a function of the landslide generating mechanism. Simple landslide mechanisms, modelled as rectangular shaped trolleys sliding down a ramp were designed and built in the LIAM laboratory of the DISAT department, L'Aquila University. Impulse waves were generated by the landslide impact with a three dimensional water body in a wave tank, which was realized on purpose employing the largest space which was available in the laboratory. The tank was large enough to study waves generated in the *near field* and propagating in part of the *far field*. The realized trolleys were made up of steel and concrete bricks, while the ramp was made up of steel. The angle of the ramp with the horizontal was adjustable using a system of winches. The wave tank was made up of concrete and bricks and it is 12.0 m long, 6.0 m large and 0.8 m deep.
An overflow structure was set on two sides of the wave tank in order to settle the water level and to absorb part of the incident wave energy. The absorption performance of the overflow structure had been previously tested using the wave flume experiments. Details about the reflection coefficient estimates are reported in the following Chapter 3.
Considering Figure 2.7, and referring to the horizontal plane of the water surface at rest, a system of polar coordinates (r, θ) is introduced. The origin of the system is located at the impact point of the landslide with the water. The anomaly θ is the angle between the horizontal component of the landslide velocity vector, and the position vector r.

Due to the fact that landslides were modelled using solid blocks presenting a symmetry of the front impacting water, the symmetry of the generated wave field due to the symmetry of the generation mechanism was considered when the experiments were programmed, with the aim of optimizing the surface of the realized wave tank (see Figure 2.8). In particular, assuming this approach, only half landslide falling close to the plane of symmetry of the water body (coincident with a wall of the tank) was simulated. Then, in order to measure water waves oscillations considering the highest values of r the wave tank can provide, two different model layout were defined (see Figure 2.9), with a wave gauges layout sketched in Figure 2.7. The wave gages were placed according to two main fixed directions, sloped one another by an angle equal to 30.0°. Therefore, with reference to Figure 2.9, Configuration A was employed to record waves propagating with $\theta = 0.0°$ and $\theta = 30.0°$, while, by using Configuration B, waves propagating with $\theta = 60.0°$ and $\theta = 90.0°$ were recorded.
In conclusion, by using the symmetry of the wavefield and the double configuration of the ramp for each experiment, a virtual rectangular tank, characterized by a surface four times

greater than the model wave tank surface, was effectively modelled in the experimental study. Figure 2.10 presents a picture of the wave tank and the landslide model, on the left, and a picture of one of the performed experiments, on the rigth.

Waves oscillations were measured by 10 resistance wave staffs, 0.8 m long, which signals were amplified in the range ±10 Volts. A Metra Mess CB41 mono-axial accelerometer was put on the back of the trolley in order to define both the impact velocity and the time series of the trolley acceleration. Both wave and acceleration signals were acquired by a 16 channels National Instruments analog to digital conversion board. The added instrumental noise was less than 0.01% than the original acquired signals. The wave records were 20.0 s long, with a sampling frequency of 50.0 Hz. The acceleration data were collected for 20 s with a sampling frequency of 1000 Hz.
A dimensional analysis of all involved parameters was carried out in order to chose the variable to test and to define the experimental program to run. Referring to the dimensional analysis presented in the previous section, any physical variable of the generated wave field can be expressed as:

$$A = f\left(l, w, h, d, v, \alpha, \beta, \theta, p, \rho_s, \rho_w, \mu, g, r, t\right) \tag{2.5}$$

Making reference to Figure 2.9, ρ_s is the density, p is the porosity, v is the impact velocity of the landslide; l, w, h are respectively the length, width and height of the modelled trolley landslide; β is the inclination angle of the landslide front with the ramp; d is the local water depth; α is the ramp inclination angle with the horizontal; μ and ρ are the water viscosity and density respectively; r and θ assume the above introduced meaning of polar coordinates; finally, t is the elapsed time.

It can be observed from Equation 2.5 that a large number of physical variables is involved in the experimental study of landslide generated waves in a three dimensional water body. First of all, on the basis of results obtained by Kamphuis and Bowering (1972) and by Huber & Hager (1997), the influence of the water viscosity μ was neglected, and consequently the Reynolds number. Moreover, the landslide porosity and density were kept at the constant values $p = 0.0$ and $\rho_s = 2200\ Kg/m^3$, while the angle of the landslide front β was fixed at the value 90°, as sketched in Figure 2.9.
With the assumed model simplifications, equation 2.5 can be rewritten by means of dimensionless groups by considering the water depth d as the length scaling parameter:

$$\Pi_A = f_A\left(\frac{l}{d}, \frac{w}{d}, \frac{h}{d}, \frac{v}{\sqrt{gd}}, \alpha, \theta, \frac{r}{d}, t\sqrt{\frac{g}{d}}\right) \tag{2.6}$$

By employing 10 resistance wave staffs set according to the layout sketched in Figure 2.7, and assuming two different model configurations A and B, it was possible to have 5 values of the distance r from the impact point, equal to $[1.05; 2.05; 3.05; 4.55; 6.05]$ m, and 4 different values of θ, equal to [0.0; 30.0; 60.0; 90.0]°. Finally, two values of the water depth d were assumed, equal to $[0.4; 0.8]$ m.

Table 2.3 reports the experimental program expressed by means of dimensional parameters. Due to the fact that 2 experimental values of parameters h, w and d, 3 experimental values were assumed for parameters v and α, 2 different model configurations were considered, and each test was repeated twice in order to reduce the experimental errors, 288 tests were carried out, thus producing a database of 2880 wave records.

Table 2.4 shows the values assumed by dimensionless groups.

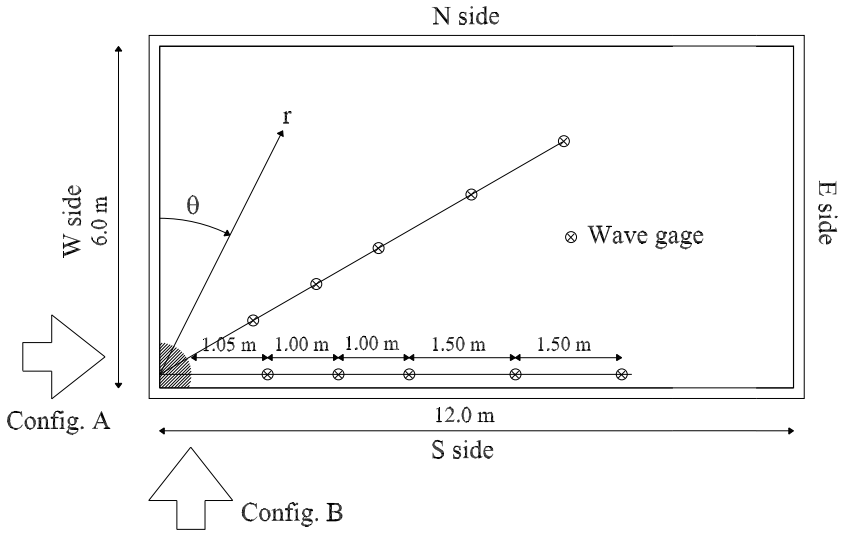

Figure 2.7: Sketch of the realized wave tank, the wave gauges layout, and the landslide impact directions assumed in Configuration A and B. The overflow structure for the reduction of wave reflection was realized along N and E sides.

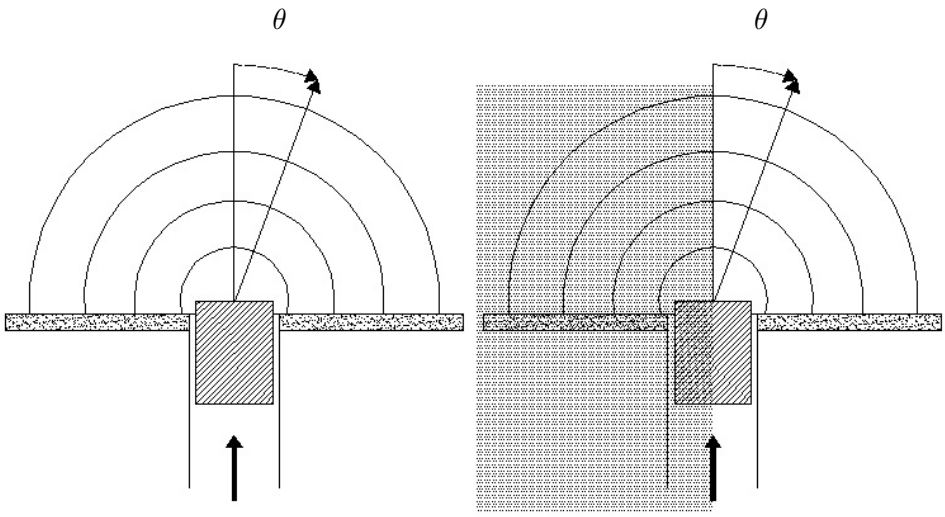

Figure 2.8: Symmetrical properties of the wave field obtained by employing a landslide model with a symmetrical geometry. On the left, generation of impulse waves in the range θ [-90; 90]°. On the right, reduction of the realized experimental model to the range θ [0; 90]°.

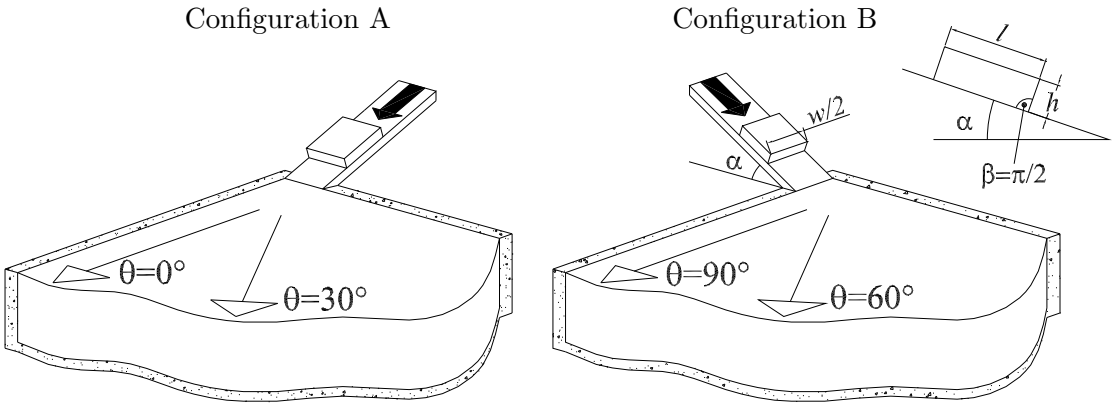

Figure 2.9: Configuration A and B of the three dimensional model for the generation of waves due to a subaerial landslide falling into water. The top right figure reports the trolley dimensions, the considered ramp inclination angle α, and the angle β of the landslide front.

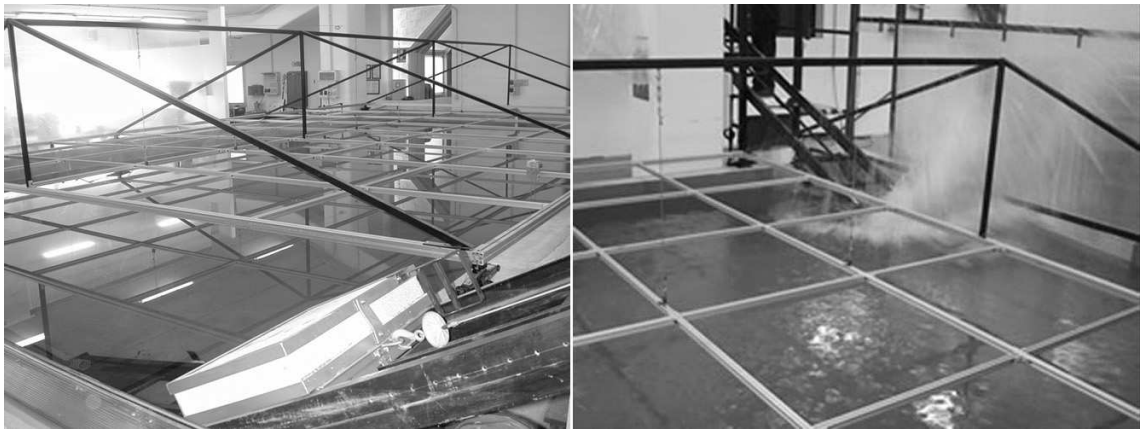

Figure 2.10: Pictures of the three dimensional model and wave tank, on the left, and impact of the trolley with water during one of the performed experiment, on the right.

$h\ [m]$	$w\ [m]$	$v\ [m/s)]$	$\alpha\ [^\circ]$	$d\ [m]$	$r\ [m]$	$\theta\ [^\circ]$
0.09	0.60	2.8	16	0.4	1.05	0.0
0.18	1.20	3.7	26	0.8	2.05	30.0
		4.4	36		3.05	60.0
					4.55	90.0
					6.05	

Table 2.3: Experimental program of the three dimensional model.

h/d	w/d	l/d	$v/\sqrt{gd}$	$cos(\alpha)$	$cos(\theta)$	r/d
0.1125	0.75	0.525	0.999	0.276	1.000	1.312
0.2250	1.50	1.050	1.320	0.438	0.866	2.562
0.4500	3.00		1.413	0.588	0.500	2.625
			1.570		0.000	3.812
			1.867			5.125
			2.221			5.687
						7.562
						7.625
						11.375
						15.125

Table 2.4: Values assumed by dimensionless parameters in the study performed on the three dimensional model.

Chapter 3

Analysis of experimental data

3.1 Introduction

Different methods of data analysis were numerically implemented and then employed in order to properly describe landslide generated waves features.
Firstly, the characterization of impulsive waves transient nature had been faced, considering the time series of water oscillations recorded during the performed experiments. Classical methods of signal analysis, such as the Fourier Transform (FT hereinafter) are not able to properly characterize time localized energy contributions. Hence, the recently introduced Wavelet Transform analysis (WT hereinafter) was considered to study transient events localized both in time and frequency. A WT numerical code was implemented on purpose using the Matlab computer language, by means of which the energy propagation of impulse waves was estimated in a surprisingly easy and meaningful way. The WT, introduced by Grossmann and Morlet (1984), provides the energy density distribution of a given signal over the time and frequency domains, overcoming the assumption of periodicity, being therefore applicable also to non-stationary time series. So far, WT has been applied to data analysis, data filtering, file compression, and analysis of images in the fields of Engineering, Physics and Economics. In ocean engineering, Massel (2001) gave an example of the application of WT to ocean surface wave records along with some meaningful examples describing the analysis of simple signal. Amongst past studies, it is worthwhile mentioning Liu (1999), who pointed out some interesting features on time-frequency energy distribution of sea waves, defining new dimensionless parameters describing wave groups. In the present work, the application of WT to wave records from the two-dimensional model is introduced. It is shown that the dispersive features of a transient wave can be easily characterized using the WT. Part of the obtained results of the application of WT to landslide generated waves time series were

published in the work of Panizzo et al. (2002).
Subsequently, on the basis of the three dimensional physical experiment, the definition of an engineering tool able to forecast landslide generated waves' principal parameters is faced. Physical variables able to describe the landslide and the wave features are accurately selected. In this issue the landslide is considered as the "wavemaker mechanism", and parameters able to define the energy transfer between the landslide and the water are taken into account. On the other hand, zero crossing parameters deduced from wave records is taken into account to describe the generated impulse wave field. In particular, the maximum wave height and the related wave period are considered. At a first step, the forecasting formulation is defined using the classic multiple regression approach from experimental data, and then using the Gauss-Newton non-linear optimization method, which has been developed on a Matlab platform on purpose. Subsequently, a Matlab numerical code modelling Artificial Neural Networks was implemented in order to improve the forecasting model accuracy in the correlation of experimental data. In the followings, it is shown that the forecasting formulations obtained using both the classic regression approach and the newer ANN approach fit very satisfactorily experimental data.

3.2 Experimental results from the two dimensional model

This section presents the characterization of the dispersive nature of landslide generated waves, which has been carried out using water level elevations from the two dimensional experiments performed in a 4.0 m long wave flume. The experimental layout has been introduced in the previous chapter. Here, the application of WT analysis is presented and discussed, while a brief description of the wavelet transform is reported in Appendix A. It is shown that the celerity of impulsively generated waves, the reflection by an overflow structure and seiching phenomena of the flume are successfully characterized.

3.2.1 Wavelet analysis of impact waves

Surface elevation and related wavelet spectra of some representative experiments are shown on Figure 3.1. The first two rows refer to an experiment with water depth of 0.06 m, the two middle rows to the case of water depth equal to 0.10 m and lower two rows to the case of water depth equal to 0.23 m. All these experiments were carried out with a vertical wall being the right boundary of the flume: in a following subsection experiments with an overflow structure will be illustrated. Making reference to wave gauge names, layout and notation introduced in the previous chapter, in experiments reported by Figure 3.1 the falling box mass was 2.0

kg, λ was 0.05 m and $\xi = 0.00$ m. Taking into account also Figure 2.1, on each couple of rows the water surface elevation recorded by gauges G1 (left panels), G2 (middle) and G4 (right) is presented on upper panels while the corresponding spectra are presented on lower panels. Wavelet spectra are plotted by means of contour lines of constant energy density. The meaning of these plots is easily understandable: they are similar to Fourier spectra but energy located at each frequency is spread in time. By adding energy at each frequency (i.e. adding the wavelet coefficients on horizontal sections) and dividing the results by an appropriate normalization coefficient, the Fourier component at that frequency is obtained.
Before using the WT to describe different types of impulsively waves observed during the experiments, it is useful to briefly focus on some interesting features of the waves under investigation. As previously discussed in Chapter 1, Prins (1958), Wiegel et al. (1970) and Noda (1970) performed several physical experiments and concluded that, depending on the landslide volume and the energy exchange between the landslide and the water, impact waves present different characteristics. Note that although Prins did not use a falling box to generate waves but imposed a local disturbance to the free surface, the results he obtained are still applicable to waves from these experiments. Basically four types of impact waves were observed by these authors: (1) leading wave with oscillatory wave characteristics, (2) leading wave with solitary wave characteristics, followed by a trough connecting it with the dispersive wave pattern, (3) leading wave being a single wave with solitary wave characteristics, separated by the dispersive wave pattern, (4) solitary wave with complex form (bore in the first stage). Referring to the reproduced Scott Russell wave generator, the generated waves type vary from (1) to (4) gradually as the ratios λ/d and h/d increase. It can be concluded that when the dimensions of the falling body are large in comparison to water depth, solitary waves are to be expected while a train of dispersive waves is likely to be generated in relatively deep water. The performed experiments seem to confirm this. It is easy to recognize that impact waves generated in the experiment with water depth equal to 0.06 m (first row of Figure 3.1) is a solitary wave with a tail. Its shape does not change significantly from gauge to gauge even if a decrease in height, probably due to non linear energy transfer while propagating, is observed. Even after being reflected several times at the left and right-end of the flume the shape of the solitary wave can be recognized in the plots. On the contrary, impact waves observed when water depth was equal to 0.23 m (fifth row) are quite different from a solitary wave and are more similar to a group of dispersive waves.
Impact waves can be also described by means of wavelet spectra. Wavelet spectra for water depth equal to 0.06 m (second row of Figure 3.1) and 0.23 m (sixth row) are significantly different. In the first experiment the shape of the spectra does not change from gauge to

gauge even if a general decrease in energy is appreciable. Note that by examining the wavelet spectra it can be confirmed the fact that the solitary wave can be viewed as the superposition of several components with different frequencies. Each component travels with a celerity which is independent from the frequency; it is equal to all other components celerity (i.e. it is bound to other components) and coincides with wave phase speed as the comparison with surface elevation plots suggests. On the contrary in the second and third experiment (water depth equal to 0.23 m) the spectra change from gauge to gauge: they tend to rotate clockwise. In other words for this case wave energy measured at subsequent gauges characterized by low frequency (1-2 Hz) is less shifted in time than high frequency (2-3 Hz) one. This is clearly due to different celerity of waves characterized by different frequencies. In section 3.2.1 it is demonstrated by means of WT that in the first case celerity at which energy propagates is similar to solitary wave celerity and that in the second case energy travels in reasonable agreement with linear wave theory group celerity.
Further interesting features of impact waves can be deduced by means of WT. As indicated in Figure 3.2, by drawing the contour lines corresponding to appropriate energy levels, the wavelet spectra results are made up of three components. The main component is related to the wave packet generated by the falling box propagating from left to right and is labelled as "Impact wave" on the figure. Energy related to waves reflected at the right-end of the wave flume is also visible on the spectra. This energy is shifted in time of an amount which is function of the distance between the gauge and the reflecting structure. In section 3.2.1 a method for dividing incident from reflecting wave energy is described and used to estimate the reflection coefficient of the overflow structure. Finally long period waves are evidenced by using WT. Energy characterized by very low frequency (0.1-0.5 Hz) is clearly visible on each wavelet spectra. This suggests that seiche waves affected the flume during the experiments. In section 3.2.1 WT is used to evaluate the period of the oscillating modes of the flume.

Impact waves celerity

In this section WT is applied to estimate the celerity at which the energy of the impact wave propagates. The proposed method is based on the idea that each coefficient of the wavelet spectra can be viewed as a wave train, localized in time, characterized by its own frequency and energy. By comparing wavelet spectra obtained at subsequent wave gauges (the distance between two generic gauges is indicated as Δx), the time Δt that this wave train takes to travel the distance Δx can be estimated. The ratio $\Delta x/\Delta t$ would finally provide an estimate of the wave energy celerity. This approach would work properly if no energy dissipation occurred during the propagation process. In that case it would be easy to follow

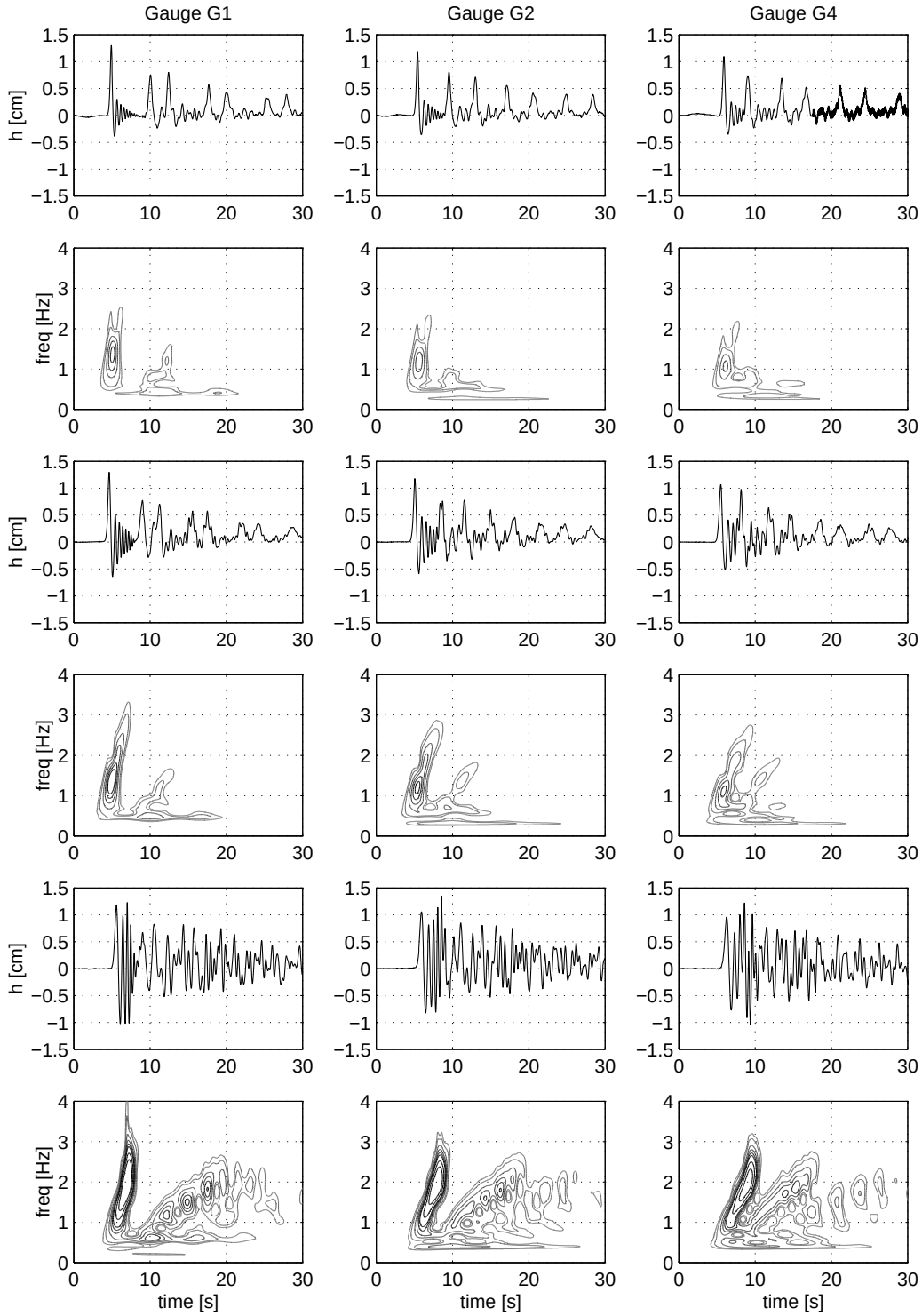

Figure 3.1: Surface elevation and wavelet spectra for three different water depth and vertical wall at the right-end of the flume. Wavelet spectra show equal energy density contour lines at 0.0006 0.001 0.002 0.003 0.004 0.005 0.008 0.012 m^2.

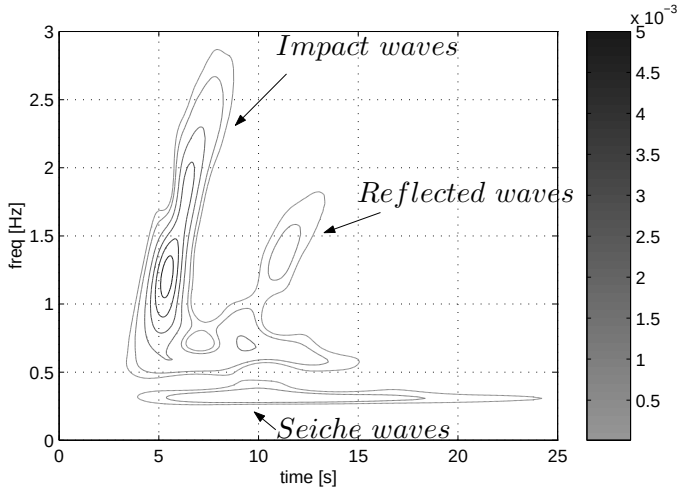

Figure 3.2: Typical wavelet spectra of impulsively generated waves.

from gauge to gauge wave trains of constant energy, i.e. constant values of spectra coefficients. Unfortunately wave energy of a specific wave train is not conserved due to energy losses and nonlinear energy transfer. A possible method to overcome this difficulty is to identify on each frequency the time at which spectra maximum occurs as detailed in the following. On upper panels of Figures 3.3 and 3.4 wavelet spectra obtained at gauges G1, G2 and G4 are shown ($\lambda = 0.10$ m, $\xi = 0$ m and box mass of 2.0 kg); on the same plots dots indicate the absolute maximum of energy on each frequency. A good estimate of celerity can therefore be obtained by evaluating the time that the maxima take to travel from gauge to gauge. Note that the method is unapplicable to very low (0-0.5 Hz) frequency components of the spectra; as demonstrated in section 3.2.1 these long period waves are flume seiches and therefore present standing waves characteristics.

It is useful to present the results of a slightly different approach to the problem. By taking as reference the wavelet spectra measured at gauge G1, each wave packet was propagated to the next gauges G2 and G4 by means of linear theory, i.e. each single coefficient of the spectra, corresponding to the energy of a wave packet, is transferred to the next gauge with a celerity corresponding to group celerity $c_g(f)$. Basically the following expression was applied to reconstruct the generic energy spectra E at gauge j

$$E_j(t, f) = E_{G1}\left(t - \frac{\Delta x_j}{c_g(f)}, f\right) \tag{3.1}$$

where t is time, f is frequency, Δx_j is the distance between gauge G1 and the generic gauge j. The comparison between measured and reconstructed spectra reveals that energy travels in reasonable agreement with linear theory waves.

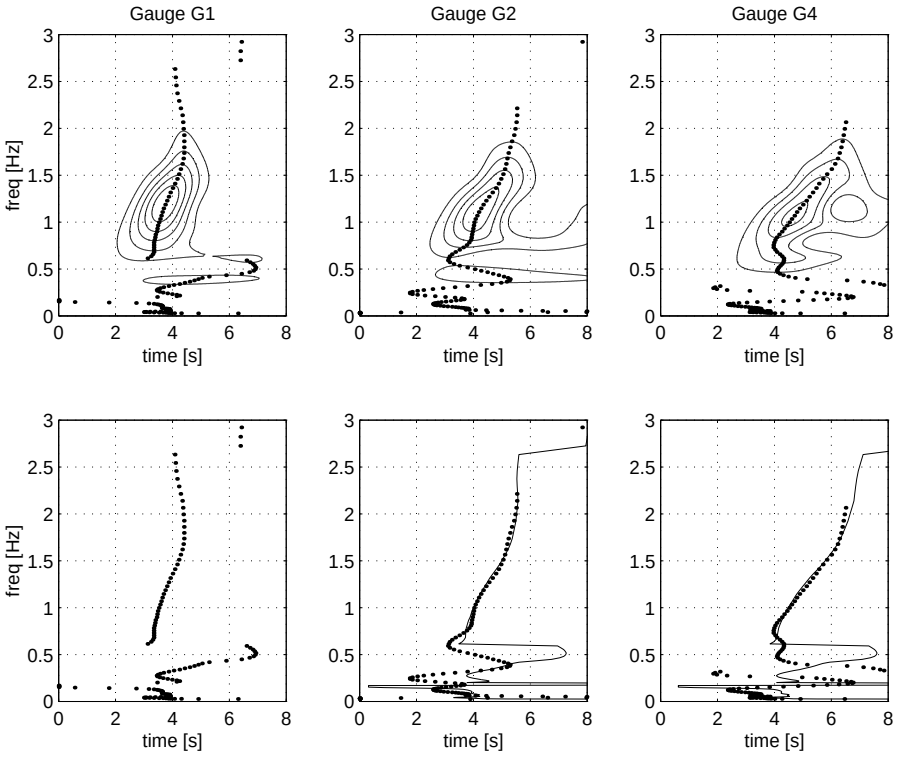

Figure 3.3: Measured and reconstructed wavelet spectra at three gauges for water depth equal to 0.23 m. On upper panels the measured spectra (solid contour lines) and absolute maximum energy densities (dots) for each frequency are shown. On lower panels measured maximum energy density (dots) and maximum of spectra reconstructed by applying Equation (3.1) (solid line) are plotted.

In order to help the reader estimate the difference between reconstructed and measured spectra in lower panels of Figure 3.3, the maximum of the measured (dots) and reconstructed (continuous lines) spectra are shown. Notice that since the wavelet spectrum related to gauge G1 was used as input on the left panels of the Figure only the measured maxima are shown. The wavelet spectrum on Figure 3.4 is typical of a solitary wave since its shape does not change significantly from gauge to gauge. The dashed line shows that Equation (3.1) does not apply. For this specific case the celerity c_s of the solitary wave was also used; the maxima of the spectra reconstructed by using c_s are indicated with a solid line. The celerity of the solitary wave was evaluated by means of the following expression

$$c_s = \sqrt{gd}\left(1 + \frac{a}{2d}\right) \tag{3.2}$$

where $g = 9.81$ m/s^2, d is the undisturbed water depth and a is solitary wave amplitude.
It can be concluded that depending on wave characteristics the celerity at which wave energy

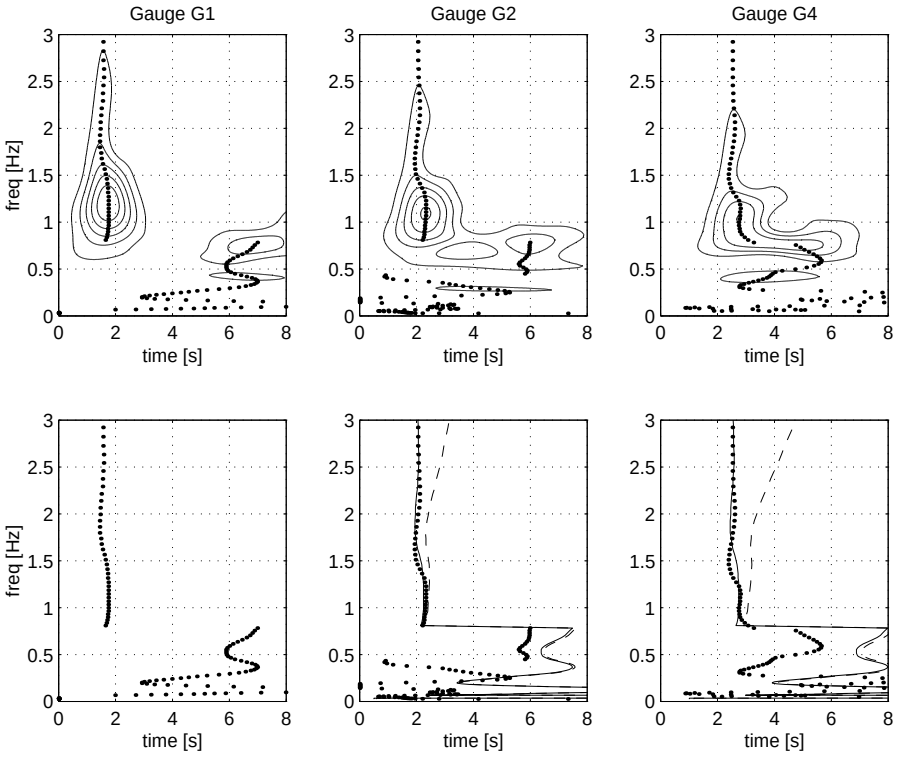

Figure 3.4: Refer to caption of Figure 3.3 for notation. For this specific case solid lines on lower panels represent maxima reconstructed by means of solitary wave celerity while dashed lines represent maxima reconstructed by means of Equation (3.1).

propagates may vary between the celerity of the solitary wave (relatively shallow water) and group celerity of linear theory (relatively deep water). It is to be stressed that a classical analysis based on Fourier Transform does not allow to study the celerity of propagation of the waves under investigation.

Estimate of the reflection coefficient of the overflow structure

When estimating the reflection coefficient of a structure the most natural approach is to split the wave field measured in front of it into an incident and a reflected one. Then, by comparing the two wave fields, the reflection coefficient K_r can be obtained. For example K_r can be defined as the ratio of the reflected waves height to that of the incident waves or, in the case of random waves, the ratio of the square root of energy of the reflected waves to that of the incident waves. One of the most widespread techniques used to estimate the reflection coefficient of a structure in presence of incident random waves is that one introduced by Goda and Suzuki (1976). Goda and Suzuki used the Fourier Transform to obtain the wave power

spectrum of the total wave field measured by two gauges and then introduced a method to individuate the spectra of incident and reflected waves. Total incident (E_i) and reflected (E_r) wave energies were then used to evaluate the total reflection coefficient, this being given by

$$K_r = \sqrt{\frac{E_r}{E_i}}. \tag{3.3}$$

This method is unapplicable to impact waves, cause it is based on the assumption that the wave field is stationary and periodic. Nevertheless it is still possible to use equation (3.3) if a suitable technique to separate incident from reflected waves is employed. In the following the application of WT to this scope is described. Note that WT has been previously used by Stamos and Hajj (2001) to calculate wave reflection and transmission over a submerged breakwater, but they used a particular technique valid for regular and stationary waves only. The technique here proposed is based on the assumption that the celerity at which impact wave energy propagates is known. As shown in the previous section, depending on waves characteristics this celerity varies between the group celerity c_g and the solitary wave celerity c_s. Furthermore it is here assumed that the portion of the incident and reflected wave spectra which overlaps in time is negligible if compared to the total spectra. The method will be described with reference to Figure 3.5 in which water surface levels recorded by gauges G1, G2 and G4 are shown on the upper panels. Middle and lower panels show the wavelet spectra by means of energy contour lines and time series of the wave energy obtained by cutting the two dimensional spectra with sections of given frequency (1.03 Hz). This test was carried out employing the overflow structure, $d = 0.23$, $\lambda = 0.05$ m, $\xi = 0.00$ m. Referring to the constant frequency section plots, it is clearly evident that the first energy maximum is moving forward in space i.e. from left to right in the wave flume. This energy is therefore related to incident waves which reach first wave gauge G1, then G2, and finally G4. On the contrary the second energy maximum is moving from right to left, as it firstly reaches the wave gauge G4, then G2 and finally G1. The second energy maximum is related to waves reflected by the structure under investigation. The method adopted for dividing incident from reflected energy assumes that relevant incident waves are measured when energy is greater than a threshold value, say five percent of the maximum energy measured on the frequency at hand. This instant is named t^i_{start}. Now it is possible to compute the time Δt that waves take for propagating to the right-end of the flume, being reflected and reaching the gauge again. As previously mentioned the celerity at which wave energy propagates is assumed to be known. For example, for the experiment at hand, the group celerity could be employed; if the distance between the wave gauge and the reflecting structure is Δx, the time Δt is given by:

$$\Delta t = \frac{2\Delta x}{c_g} \tag{3.4}$$

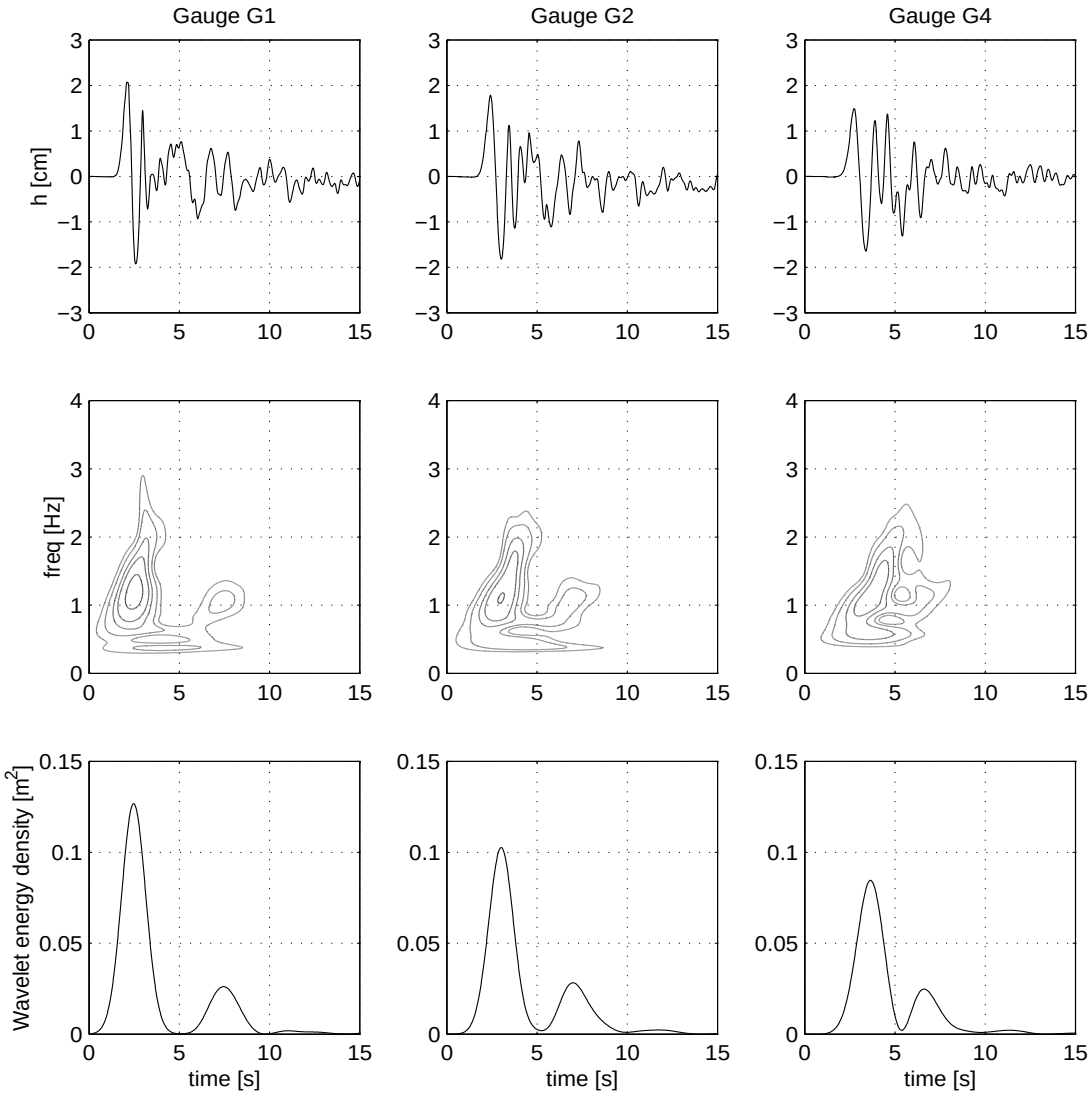

Figure 3.5: Experiment with vertical wall, water depth equal to 0.23 m and $\lambda = 0.10$ m, box mass 2 Kg and box immersion $\xi = 0.03$ m. From upper to lower panel: water surface elevation records, two dimensional wavelet spectra (energy contours at 0.01 0.02 0.04 0.06 0.1 m^2), constant frequency section (1.03 Hz) of spectra.

The time at which reflected waves start reaching the gauge is given by $t^r_{start} = t^i_{start} + \Delta t$. It is assumed that the wavelet energy for $t < t^r_{start}$ is related to incident waves and the wavelet energy for $t^r_{start} < t < t_{end}$ is related to reflected waves (t_{end} is a time chosen such that re-reflected waves by the left-end of the flume are not taken into account). This procedure can be carried out for each frequency of the wavelet spectrum separating the spectrum as desired. In Figure 3.6 an example of separation of incident and reflected wavelet spectra is shown. The left panel on this Figure shows the wavelet analysis of a test performed employing the

vertical wall with water depth equal to 0.23 m, $\lambda = 0.05$ m, mass 2 kg and $\xi = 0.0$ m. On the middle and right panels the incident and the reflected spectra obtained by applying the technique previously described are shown.

This methods is valid if incident and reflected wavelet spectra are distant in time. This can be achieved by using surface elevations recorded by gauges sufficiently distant from the structure under investigation. Nevertheless it is to be noted that by using wave gauges distant from the structure energy losses assume relevant importance. It is hard to decide what portion of energy was dissipated during the partial reflection process and what part was dissipated by bottom friction or other phenomena which could take place during wave propagation. However, comparisons between reflection coefficients obtained for the vertical wall and the overflow structure can be made. Surface elevations and wavelet spectra obtained using water depth of 0.23 m, box dimension λ equal to 0.05 m, box mass of 2 kg and box immersion ξ of 0.0 m are represented on Figure 3.7. Note that the mean water level increases due to the box volume in the experiment with the vertical wall, while decreases in the experiment with the overflow structure. The first part of both surface elevation records and spectra are very similar for the two experiments assuring that incident waves are reasonably similar. From a first analysis of wavelet spectra it can be deduced that wave reflection from the vertical wall is much larger than in the case of the overflow structure. Reflection coefficients obtained on the basis of surface level records at gauges G1, G2 and G4 are summarized in Table 3.1. As expected estimates of the reflection coefficients tend to decrease as the distance from the wall increases (from gauge G4 to G1), owing to distributed energy losses. So if on the one hand gauges distant from the wall are necessary in order to keep well distinct in time the incident from the reflected spectrum, on the other hand by doing so energy losses due to bottom friction have to be quantified, which is a somewhat difficult task. A pragmatic point of view is here adopted by taking as reference the reflection coefficients calculated at each gauge in the experiments with the vertical wall. By doing so a relative reflection coefficient is set, which states the difference between the overflow structure and the fully reflective wall. The relative reflection coefficient, calculated as the ratio between the reflection coefficient of overflow structure and the reflection coefficient of the vertical wall are reported in the fourth column of Table 3.1. It can be concluded that reflection is reduced of more than fifty percent by employing the proposed structure.

A more detailed analysis can be carried out by applying the technique described to each frequency. The reflection coefficient $K_r(f)$ was estimated at each frequency by means of:

$$K_r(f) = \sqrt{\frac{E_r(f)}{E_i(f)}}. \tag{3.5}$$

where $E_r(f)$ and $E_i(f)$ are respectively the total reflected and incident wavelet energy on the generic frequency f.

In Figure 3.8 the values of the reflection coefficient as a function of frequency for the three gauges G1, G2 and G4 are presented. As one could reasonably expect, low frequency components are reflected more than high frequency ones.

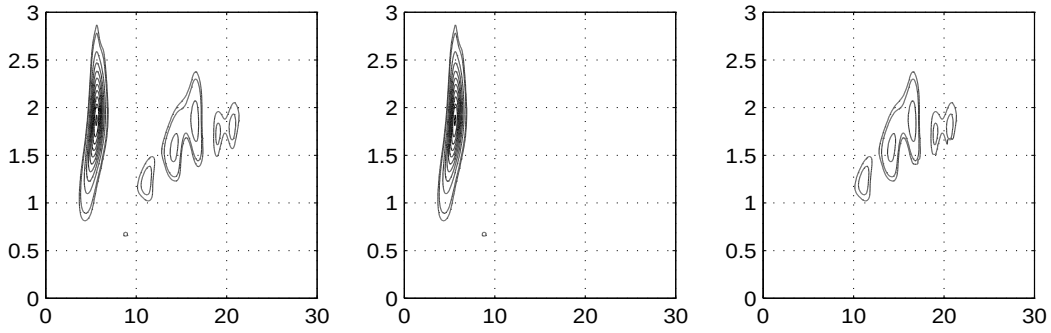

Figure 3.6: Example of separation of the two dimensional wavelet spectra into an incident and a reflected one.

Gauge	K_r (vertical wall)	K_r (overflow structure)	Relative K_r (overflow / vert. wall)
G1	0.58	0.26	0.45
G2	0.60	0.28	0.47
G4	0.63	0.31	0.49

Table 3.1: Values of the reflection coefficient K_r evaluated for the full reflecting vertical wall and the overflow structure.

Long period oscillations (seiche waves)

During the experiments it was noted that long period oscillations affected the wave flume when generating impact waves. These observations suggested that the box falling into water is able to excite the resonant modes of the flume. In this section WT is used to estimate the first oscillating periods of the wave flume; very good agreement is found with the periods obtained by using the shallow water wave theory.

When studying seiches an appropriate selection of wave gauges position is of the utmost importance. Since seiches are standing waves, if the measuring devices are placed at the nodes of the free surface oscillation, no surface elevation would be recorded. This is shown

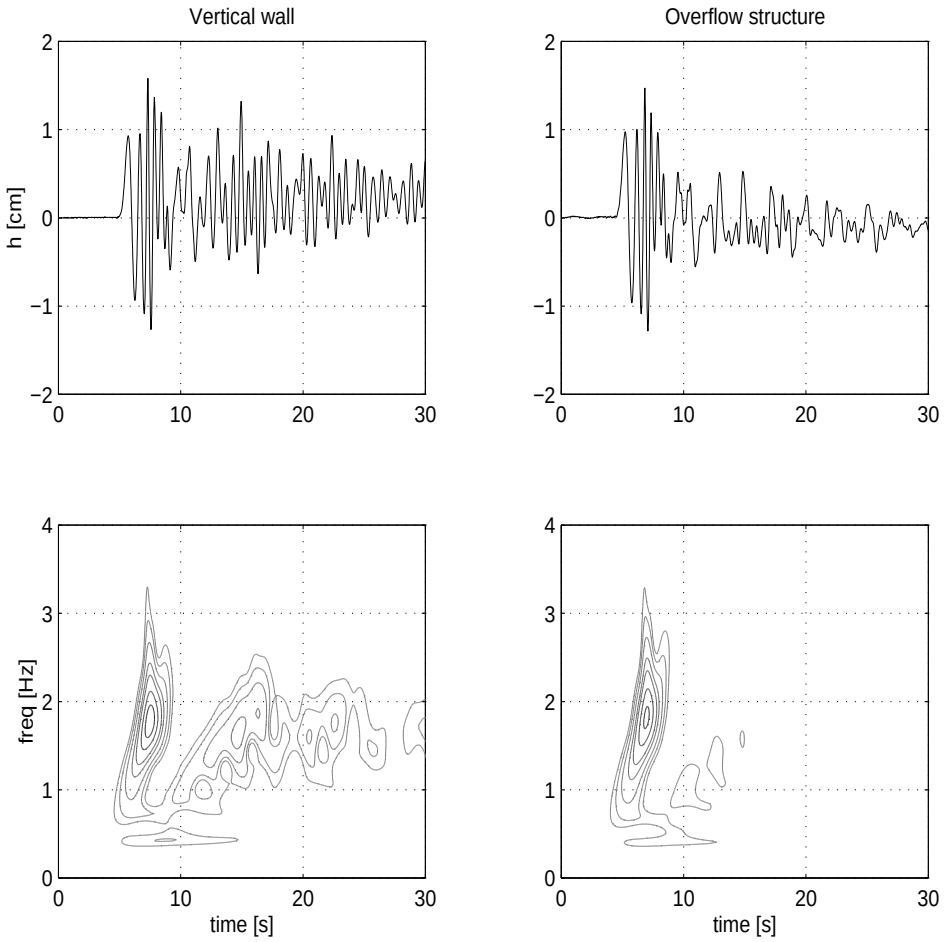

Figure 3.7: Experiment with vertical wall (left panels) and overflow structure (right panels). Surface elevations and wavelet spectra at gauge G2: contour lines indicate 0.005 0.01 0.02 0.04 0.06 0.1 m^2 energy density levels.

on Figure 3.9; for example gauge G3 does not record any surface elevation of the 1^{st} and 3^{rd} modes waves while should properly denote surface elevations related to the 2^{nd} and 4^{th} oscillating modes waves. The only gauge which is able to reveal all seiche waves is gauge G6, which is very close to the right-end of the wave flume. For these reasons it is useful to present wavelet spectra of surface elevations measured at gauges G3, G5 and G6. The results are shown on Figures 3.10 and 3.11 (water depth is respectively equal to 0.18 m and 0.23 m). On upper panels of each Figure the wavelet spectra related to gauges G3 (left panel), G5 (middle) and G6 (right) are shown. Contour lines represent equal energy density while horizontal, dashed lines represent the oscillating periods of the first four modes estimated by means of the following expression:

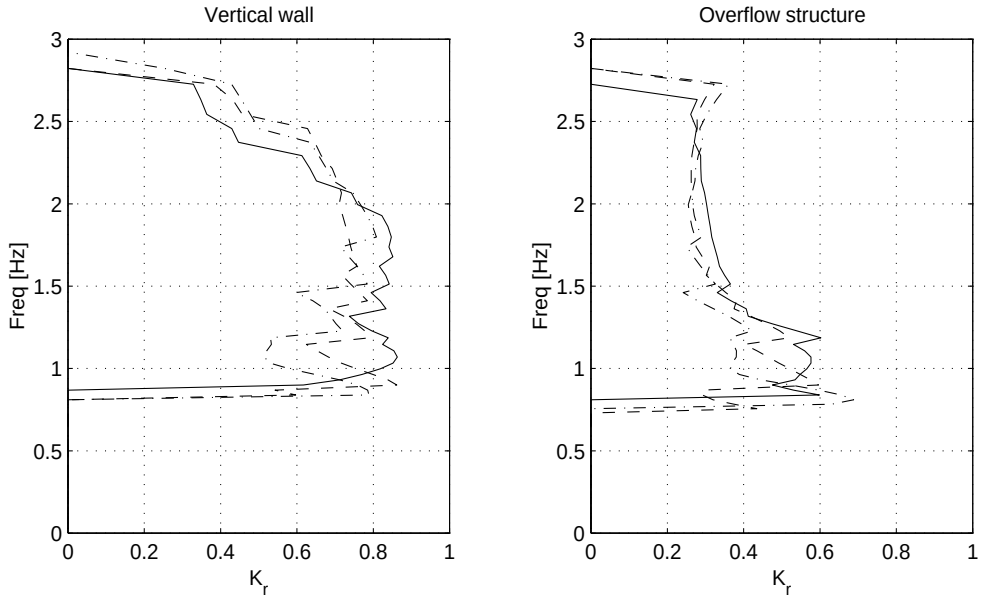

Figure 3.8: Reflection coefficient for each frequency. Solid, dashed and dashdotted lines refer to gauges G4, G2 and G1 respectively.

$$T_n = \frac{2l_0}{n\sqrt{gd}} \tag{3.6}$$

where $n = 1, 2, 3, 4$ indicates the resonant mode and $l_0 = 3.40$ m is the length of the wave flume. The well known equation (3.6) is based on the assumption that wave celerity c is given by the classical shallow water formula:

$$c = \sqrt{gd}. \tag{3.7}$$

The frequencies of the first four oscillating modes obtained by (3.6) for the two experiments at hand are summarized in Table 3.2. On the lower panels of each Figure three sections of the wavelet spectra at constant time are plotted against frequency. Sections for time equal to 8, 10 and 12 seconds are respectively plotted using solid, dashdotted and dashed lines (vertical lines with the same patterns on upper panels indicate where the section of the two dimensional wavelet spectra were made). On the same plots vertical dashed lines represent again the first four theoretical oscillating modes. Both the contour lines and constant time sections representations of the wavelet spectra for the two experiments reveal the presence of low frequency waves well localized around the resonant modes of the flume. It is interesting to note that, for the reasons discussed above, plots related to G3 indicate that no energy is located around the first resonant mode while denote a relatively large amount of energy on

the second resonant mode. Wavelet spectrum related to surface elevation measured at gauge G6 suggests that energy is present on each resonant period of the wave flume.
A quantitative estimate of the resonant periods of the wave flume was obtained by individuating the relative maxima of each constant time section. In Figure 3.12 the position of the wavelet spectrum relative maxima obtained on the basis of gauge G6 records are plotted in the time-frequency domain using dots. The upper panels refer to the experiment with water depth of 0.18 m while lower panel to 0.23 m. Similarly to Figures 3.10 and 3.11 horizontal dashed lines represent resonant frequencies estimated by using (3.6). These plots are very similar to those used for studying wave celerity (Figures 3.3 and 3.4) when absolute maxima position of constant frequency section of the spectra were plotted. It is interesting to note that horizontal rows of dots are located on the resonant periods of the flume. By taking the average of the frequency of relative maxima located around resonant modes the resonant frequencies are obtained: they were found to be equal to the theoretical ones up to the second decimal figure. Oblique series of dots represent the energy of waves reflecting at the right-end of the flume. The slope of these dots series decreases as the experiment proceeds, due to the dispersive properties of waves generated in relatively deep water.

Water depth (m)	1^{st} mode	2^{nd} mode	3^{rd} mode	4^{th} mode
0.23	0.22	0.44	0.66	0.88
0.18	0.19	0.39	0.58	0.78

Table 3.2: Frequency (in Hz) of the theoretical oscillating modes of the wave flume for each water depth used in the experiments.

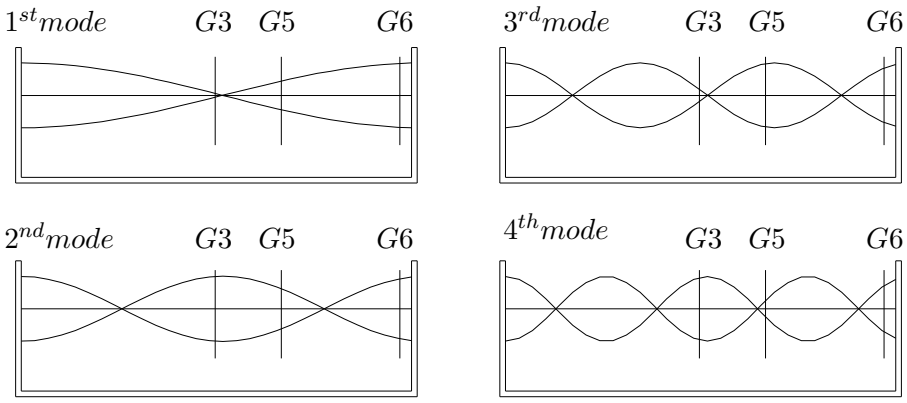

Figure 3.9: Oscillating modes of the wave flume and gauges position

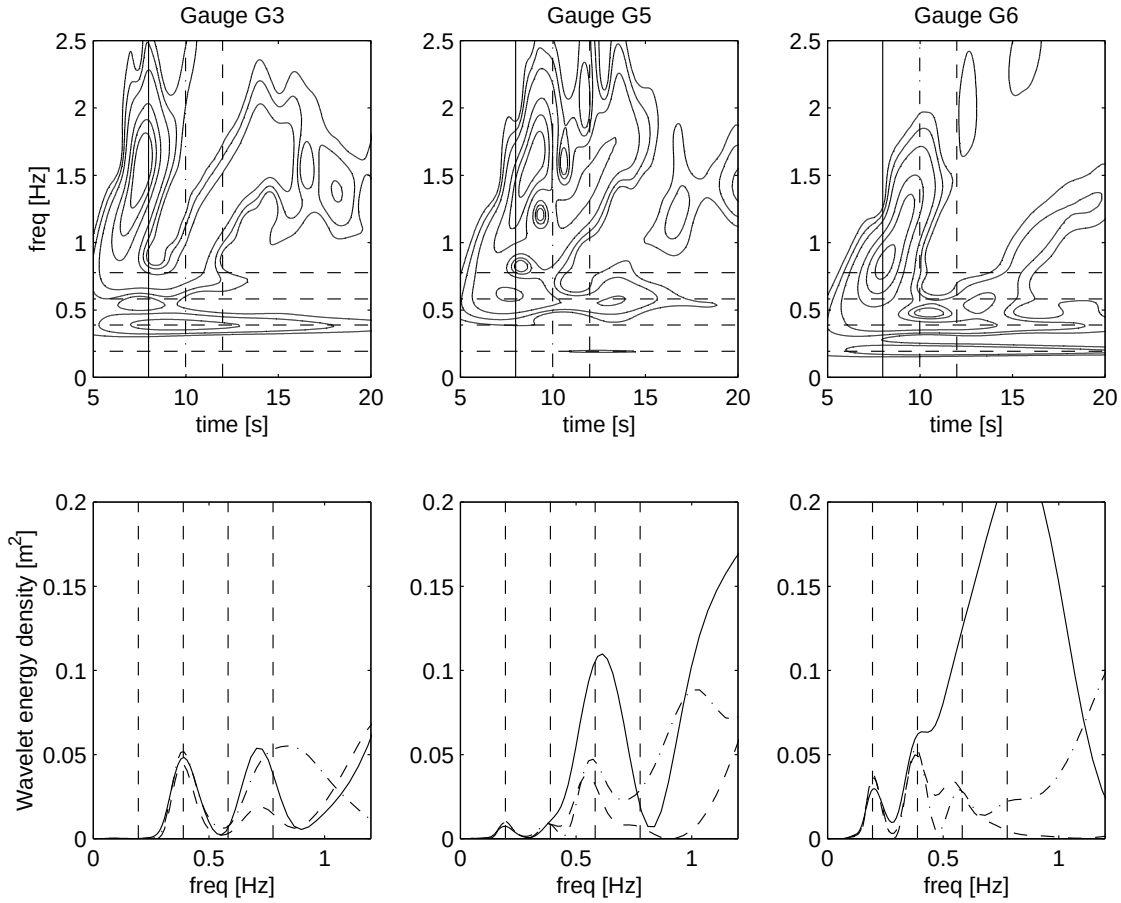

Figure 3.10: Experiment for seiche waves analysis with water depth of 0.18 m. Two dimensional wavelet spectra (upper panels) and constant time sections of the spectra (lower panels). Horizontal dashed lines in upper panels and vertical dashed lines in lower panels indicate oscillating frequencies of the flume. Vertical lines in upper panels indicate where the constant time sections were made. Constant time plots for time equal to 8, 10 and 12 seconds are plotted on the left, the middle and the right panel respectively.

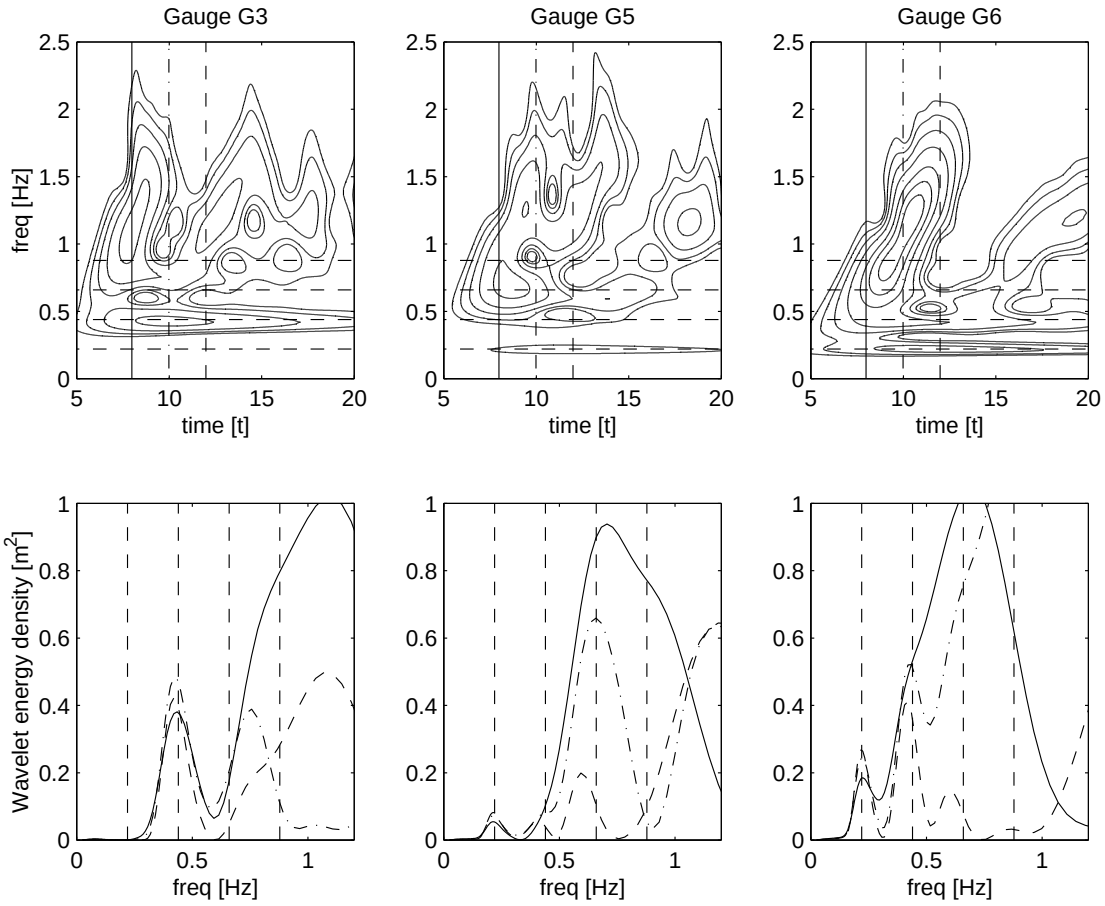

Figure 3.11: Refer to the caption of Figure 3.10 for notation. Water depth of 0.23 m.

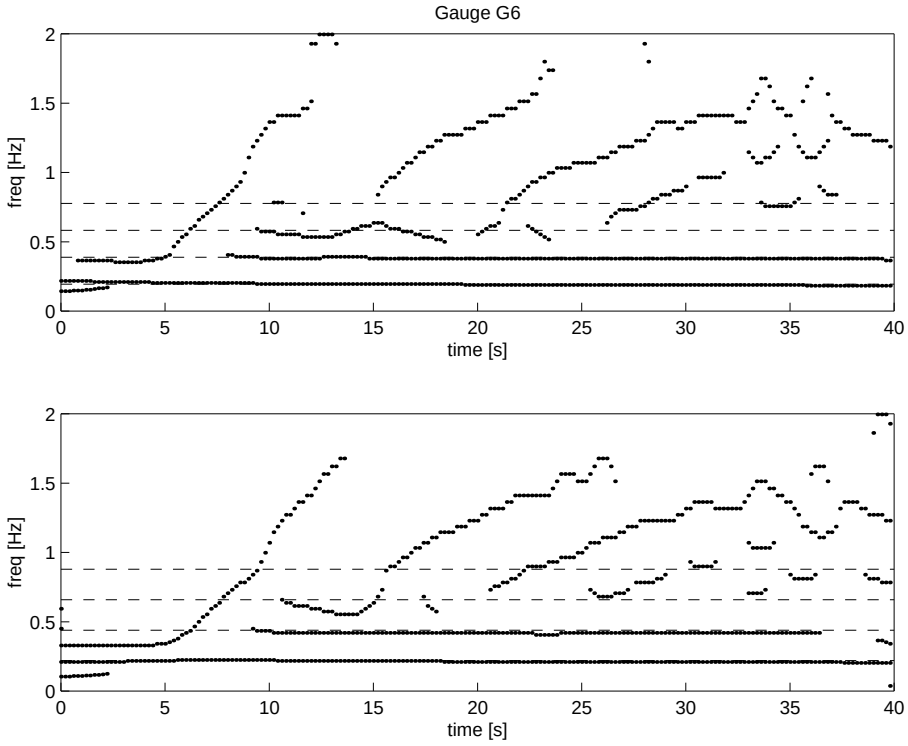

Figure 3.12: Relative maxima of wavelet spectra. Upper panel refer to water depth equal to 0.18 m and lower panel to 0.23 m.

3.3 Experimental results from the three dimensional model

While the previous section dealt with the characterization of landslide generated waves dispersive features, this section presents the analysis of data from the three dimensional experiment carried out in the wave tank. In particular, the experimental study on the three dimensional model is here used to define formulations forecasting the main parameters of impulsively generated waves as a function of landslide parameters. Standard regression approaches, involving also the Gauss-Newton optimization method, along with advanced regression approaches, such as the Artificial Neural Network model, are applied and demonstrate a very satisfactorily capability in experimental data fitting. Some mathematical details about the Gauss-Newton method are provided in Appendix B. The ANN model mathematics and architecture are briefly described in the followings.

3.3.1 Test results

Figure 3.13 reports one of the wave records from the experiments carried out to study landslide generated waves propagating in a three dimensional water body. As the study was conceived to gain empirical formulations, parameters able to to synthesize the generated wave field and the waves generating mechanism (i.e. the falling landslide) were taken into account. As far as the generated wave field is concerned, a standard zero crossing analysis of wave records was carried out, thus obtaining the maximum wave height H_{max} and the related wave period T_{max}. Moreover, the characterization of the first wave of the generated transient train was faced, defining, by means of the zero crossing analysis the value of the first wave crest (η_{1+}), trough (η_{1-}), height ($H_1 = \eta_{1+} - \eta_{1-}$) and period ($T_1$). As each test was repeated twice, only one value of the above considered six parameters was taken by averaging. The computation of the zero crossing analysis of the wave records was performed with the help of Wavelet Analysis. In particular, on the basis of results presented in the previous section, WT analysis was used to individuate waves reflected from the solid walls of the wave tank, thus taking into account only the part of the wave motion propagating away from the impact point.

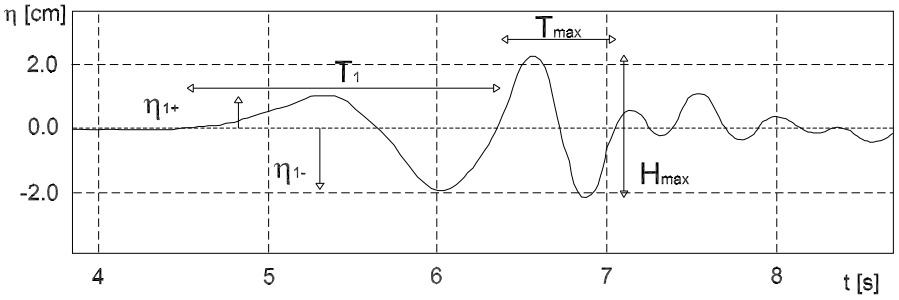

Figure 3.13: Sketch of an impulse wave along with main wave parameters.

The complete sets of *input* ($h/d; w/d; l/d; v/\sqrt{gd}; \alpha; \theta$) and *output* ($H_{max}/d$; $T_{max}\sqrt{g/L}$; η_{1+}/d; η_{1-}/d; H_1/d; $T_1\sqrt{g/L}$) dimensionless parameters, had been firstly correlated by means of a standard regression approach. In this process, parameters were considered one by one, and regressing formulations were estimated starting from a potential *main* parameter, which was expected to be r/d, followed by w/d, h/d, $v/\sqrt{gd}$, α and θ, in the sequence. Concerning α

and θ, their sinusoidal functions had been introduced, and so they were considered as $sin(\alpha)$ and $cos(\theta)$. In a second step, the obtained regression formulas were optimized using the Gauss-Newton method, which tries to minimize the mean squared errors between forecasted and experimental values by varying the coefficients in the formulations. A brief description of the Gauss Newton method, which was implemented using the Matlab computer language, is given in the Appendix B.

As far as the modelling of the maximum generated wave height is concerned, its forecasting formula was defined as:

$$\left(\frac{H_{\max}}{d}\right)^{*} = 0.12 \cdot \left(\frac{r}{d}\right)^{-0.4} \cdot \left(\frac{w}{d}\right)^{0.79} \cdot \left(\frac{h}{d}\right)^{0.5} \cdot \left(v\Big/\sqrt{gd}\right)^{0.17} \cdot e^{0.6\cdot\cos\theta - 0.8\cdot\sin\alpha} \tag{3.8}$$

Equation 3.8 presents a mean error $\bar{\varepsilon}$ equal to 0.011 from experimental data, and a correlation parameter $R^2 = 0.86$.

Figure 3.14 shows the influence of each one of the dimensionless input parameter over H_{max}/d. In particular, the dimensionless maximum wave height is presented as a function of each one of the input parameters, along with the 95% confidence intervals. It could be seen that the slide volume (parameters w/d and h/d) and the distance from impact point (r/d) have the greatest influence on the variability of H_{max}/d. As one would expect, H_{max}/d increases with the landslide volume and the landslide impact velocity, while decreases when r/d increases. The directional distribution presents a maximum at $\theta = 0.0$, as expected. The introduction of the parameter l/d didn't improve the correlation with the experimental data.

The same analysis was carried out to establish a formula forecasting the dimensionless wave period $T_{max}\sqrt{g/d}$ related the maximum wave height, which is defined as:

$$T_{\max}\sqrt{g/d} = 2.5 \left(\frac{h}{d}\right)^{0.1} \left(\frac{v}{\sqrt{gd}}\right)^{0.29} \left(\frac{r}{d}\right)^{0.18} e^{0.22\sin(\alpha)} \tag{3.9}$$

Equation 3.9 presents a mean error $\bar{\varepsilon}$ equal to 0.349 and a correlation parameter $R^2 = 0.65$. The introduction of more input parameters, in this case w/d, l/d, $cos\theta$ didn't improve considerably the accuracy of the forecasting formulation. It is to be noted that the wave period of the maximum wave height increases when increasing the distance from the impact point, the landslide front area, its impact velocity with water and the inclination angle of the slope.

In the followings, correlation formulas obtained for the principal parameters of the first wave in the generated transient train are reported, which are the crest (η_{1+}), trough (η_{1-}), height (H_1) and period (T_1).

$$\left(\frac{H_1}{d}\right)^* = 0.2\left(\frac{r}{d}\right)^{-0.8}\left(\frac{w}{d}\right)^{1.17}\left(\frac{h}{d}\right)^{0.88}\left(\frac{v}{\sqrt{gd}}\right)^{0.22} e^{1.32\cos\theta - 1.12\sin\alpha} \tag{3.10}$$

which presents $\bar{\varepsilon} = 0.0044$ and $R^2 = 0.937$.

$$T_1\sqrt{g/d} = 6.9\left(\frac{r}{d}\right)^{0.16}\left(\frac{w}{d}\right)^{0.16}\left(\frac{h}{d}\right)^{0.16} e^{0.23\cos\theta} \tag{3.11}$$

which presents $\bar{\varepsilon} = 0.4274$ and $R^2 = 0.912$.

$$\left(\frac{\eta_{1+}}{d}\right)^* = 0.069\left(\frac{r}{d}\right)^{-0.82}\left(\frac{w}{d}\right)^{1.28}\left(\frac{h}{d}\right)^{0.97}\left(\frac{v}{\sqrt{gd}}\right)^{0.2} e^{1.55\cos\theta - 1.4\sin\alpha} \tag{3.12}$$

which presents $\bar{\varepsilon} = 0.0019$ and $R^2 = 0.918$.

$$\left(\frac{\eta_{1-}}{d}\right)^* = -0.12\left(\frac{r}{d}\right)^{-0.82}\left(\frac{w}{d}\right)^{1.11}\left(\frac{h}{d}\right)^{0.84}\left(\frac{v}{\sqrt{gd}}\right)^{0.24} e^{1.21\cos\theta - \sin\alpha} \tag{3.13}$$

which presents $\bar{\varepsilon} = 0.0029$ and $R^2 = 0.935$

Figures 3.15, 3.16 and 3.17 present the application of the above defined forecasting formulations to experimental data, using two different types of graphs. The first one (always on the left) is a scatter plot reporting data forecasted using the defined formulations, on the abscissa, while the observed data are reported on the ordinate. The second graph (always on the right) is a frequency distribution histogram of the classes of errors between observed and predicted parameters values. As the error is defined as forecasted values minus observed values, positive and negative values of the error stand for overestimated and underestimated forecasts respectively.

3.3.2 Comparison of results with past studies

As introduced before, tests carried out on a three dimensional physical model were used to define formulations able to relate the principal parameters of a subaerial landslide generation mechanism with the main features of the generated wave field.

Among experimental works carried out in the past, it is interesting the comparison with results obtained by Kamphuis and Bowering (1972) and Huber and Hager (1997), due to the experimental nature of the carried out studies.

The experimental model of Kamphuis and Bowering (1972) was intended to characterize impulse waves generated by the the impact of a rigid body with water, by employing a 45 m long wave flume. The landslide was modelled using a tray without porosity, rolling down a

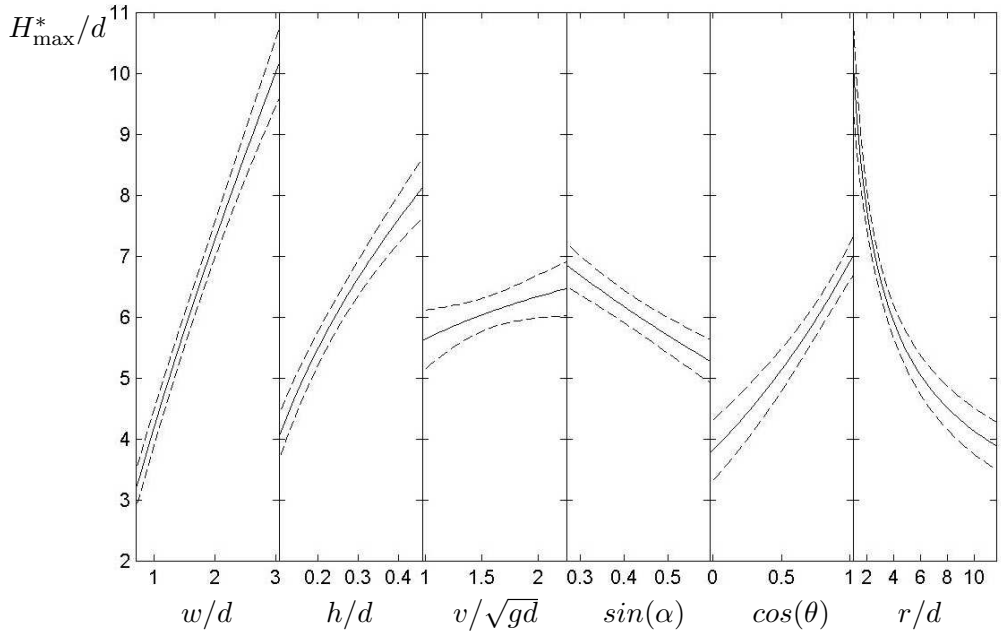

Figure 3.14: Parameters functions in the forecasting formula of H_{max}/d and their 95% confidence intervals.

ramp. Both the angle of the landslide front with the ramp and the angle of the ramp with the horizontal were considered as experimental variables. Wave oscillations were recorded by three wave gauges, set at different distances from the impact point. A formulation of the dimensionless "maximum stable wave height" H_c/d, defined as the wave height which not decrease significantly while propagating, taken in the far field along the channels, was defined as the following:

$$\frac{H_c}{d} = \left(v/\sqrt{gd}\right)^{0.7} \cdot \left(0.31 + 0.2\log\left(\frac{l}{d}\cdot\frac{h}{d}\right)\right) \tag{3.14}$$

where v is the slide impact velocity, d is the local water depth, l and h are the slide length and height respectively. Eq. 3.14 gives reliable estimates of H_c/d when the inclination angle of ramp is equal or greater than 30°, when the landslide front inclination is equal or greater than 90°, and when the dimensionless volume $q = lh/d^2$ is in the range $[0.05; 1.0]$. So, even if a complete set of experimental variables were considered in the study of Kamphuis and Bowering, the maximum wave height was influenced mainly by the slide impact velocity and by the slide volume. The far field wave attenuation was defined by the equation:

$$\frac{H}{d} = \frac{H_c}{d} + C_3 \cdot e^{-C_4 x/d} \tag{3.15}$$

where x is the travel distance, and C_3 and C_4 are expressed as a function of the other

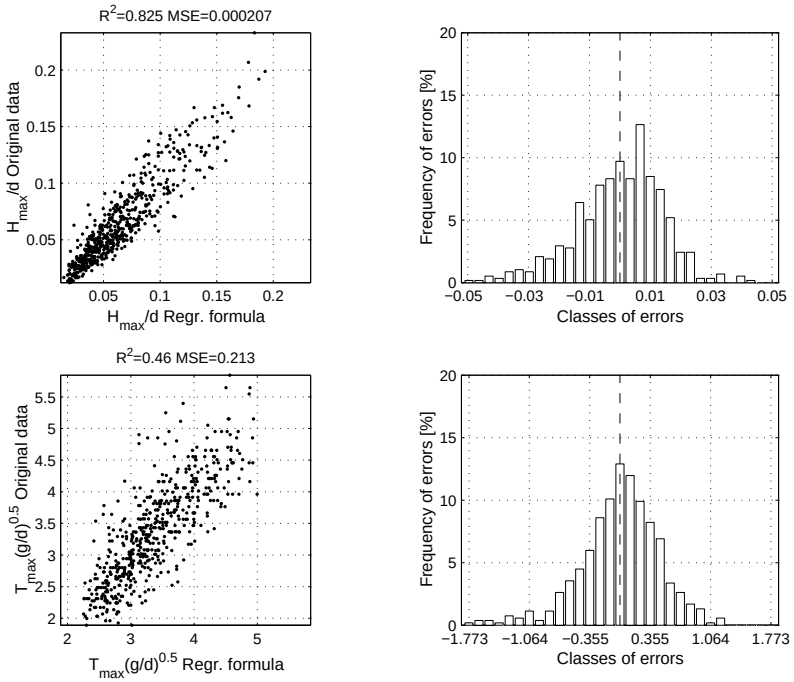

Figure 3.15: Dimensionless parameters H_{max}/d (first row) and $T_{max}(g/d)^{0.5}$ (second row). Left panels show the scatter plots of the forecasted values, on the abscissa, over measured values, on the ordinate. Right panels show the frequency distribution histogram of the classes of errors between observed and predicted parameters values.

parameters. As far as the dimensionless wave period is concerned, its correlation formula was:

$$T_1\sqrt{\frac{g}{d}} = 11.0 + 0.225\left(\frac{x}{d}\right) \tag{3.16}$$

Results presented in the present work seem to extend those obtained by Kamphuis and Bowering in a three dimensional wave field, as the considered parameters H_{max}/d and $T_{max}\sqrt{g/d}$ present analogous correlation with the experimental input variables. H_{max}/d is defined as a function of the landslide impact velocity and the landslide volume in both formulations, and this correspond to say that the energy of the impulse generated waves is mainly influenced by the energy exchange between the landslide and the water. Moreover, in both the Kamphuis and Bowering two dimensional experiment and the three dimensional experiment carried out in the present work, greater wave heights are expected at smaller slope inclination angles. About the wave period, Kamphuis and Bowering defined it as a function of the travel distance, while results from the three dimensional model here presented

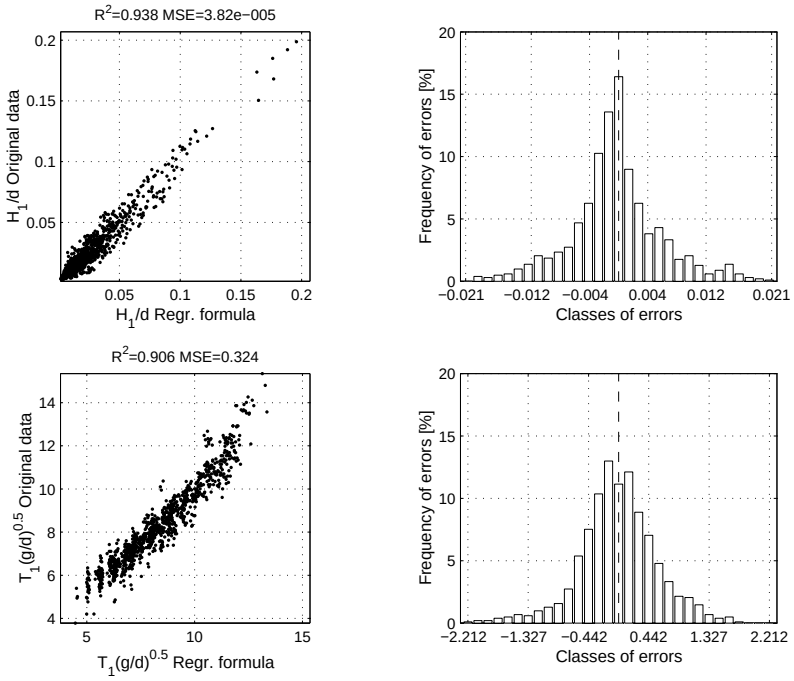

Figure 3.16: Dimensionless parameters H_1/d (first row) and $T_1(g/d)^{0.5}$ (second row). Refer to the caption of Figure 3.15 for notation.

showed that it is strongly related also to a significant landslide length and to the landslide impact velocity. Finally, while Kamphuis and Bowering correlations concerned impulse waves propagating in the *far field*, the formulation defined in the present work considered distances ranging from the near field to the far field.

Differently, the experimental work of Huber and Hager (1997) was carried out in a three dimensional wave tank. The landslides were modelled using dense debris flows, sliding down on slopes in the range $[28°; 60°]$. Few experimental details are given about this study. The impact landslide velocity was not introduced as an experimental parameter, but landslides were thrown into water at high impact velocities, which were not declared in Huber and Hager (1997) work. Their forecasting formula of the dimensionless maximum wave height H_{max}/d was the following:

$$\frac{H_{max}}{d} = 2 \cdot 0.88 \cdot sin\alpha \cdot \cos^2\left(\frac{2\theta}{3}\right)\left(\frac{\rho_s}{\rho_w}\right)^{0.25} M^{0.5}\left(\frac{r}{d}\right)^{-2/3} \tag{3.17}$$

where α is the slope angle with the horizontal, θ is the angle taken from the landslide impact velocity vector, ρ_s and ρ_w are the landslide and the water densities respectively, the parameters M is defined as $M = \frac{m}{b_s d^2 \rho_s} = \frac{V_s}{b_s d^2}$, V_s is the slide volume, b_s is the width of the

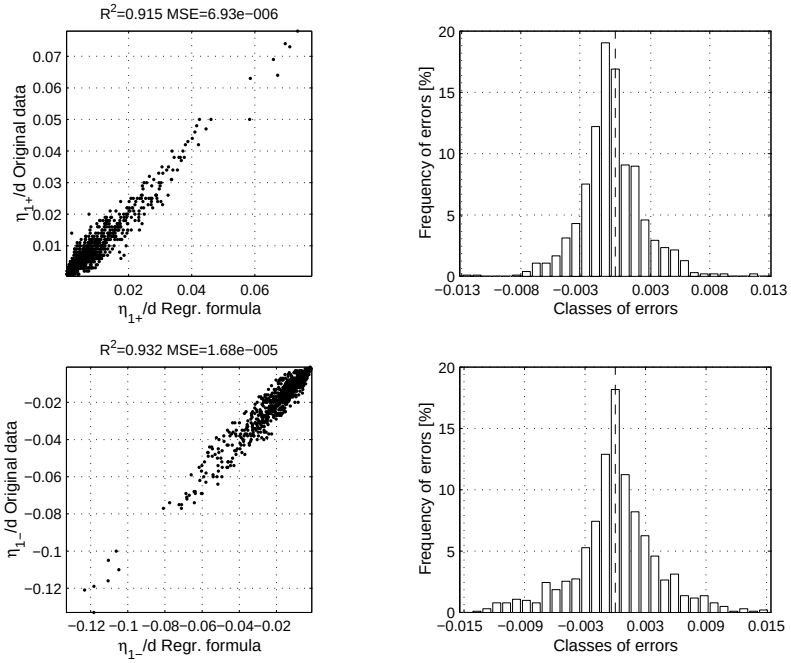

Figure 3.17: Dimensionless parameters η_{1+}/d (first row) and η_{1-}/d (second row). Refer to the caption of Figure 3.15 for notation.

slide front, r is the distance from the impact point, and finally d is the local water depth, considered as the length scaling parameter. No formulations of the wave period of the maximum wave height was defined by Huber and Hager.

Comparisons between our results and those presented by Huber and Hager (1997) are straightforward if a distribution of H_{max} in a three dimensional water body is considered. Figure 3.18 presents the application of both Huber and Hager formula (Eq. 3.17) and the formula introduced in the present study (Eq. 3.8) for the forecasting of the maximum wave height. Parameters values are: $d = 0.4$ m (local water depth); $\rho_s = 2200$ Kg/m^3 (landslide density); $w = 1.2$ m (landslide front width); $h = 0.18$ m (landslide front height); $l = 0.42$ m (landslide length); $\alpha = 26.0°$ (slope inclination angle); $v = 4.4$ m/s (impact velocity). Both formulations are calculated using values of r/d ranging in $[0.0; 15.0]$ and θ ranging in $[-90.0°; 90.0°]$. Plots in Figure 3.18 show the H_{max}/d distribution over r/d and θ domains. It is evident that Huber and Hager formula furnishes higher estimates of H_{max}/d. This is demonstrated also by the scatter plot reported in Figure 3.19, which shows the application of Huber and Hager formula to data taken from the experiments on the three dimensional model of the present work.

So that, it has been demonstrated that the formula set up by Huber and Hager gives higher

estimates of H_{max}/d, if compared to the herein presented experimental study. The correlation functions between the maximum wave height and the generation mechanism parameters are very similar in both the considered studies, except for the role of the slope inclination angle α. While the present study, according to results of Kamphuis and Bowering (1972), shows higher waves at smaller α, Huber and Hager formula gives a H_{max}/d value which is proportional to $sin(\alpha)$. The shape of the directional energy distribution (directional wave front of the maximum wave height) and the function of the wave height attenuation with r/d present a substantial agreement between the considered formulations.

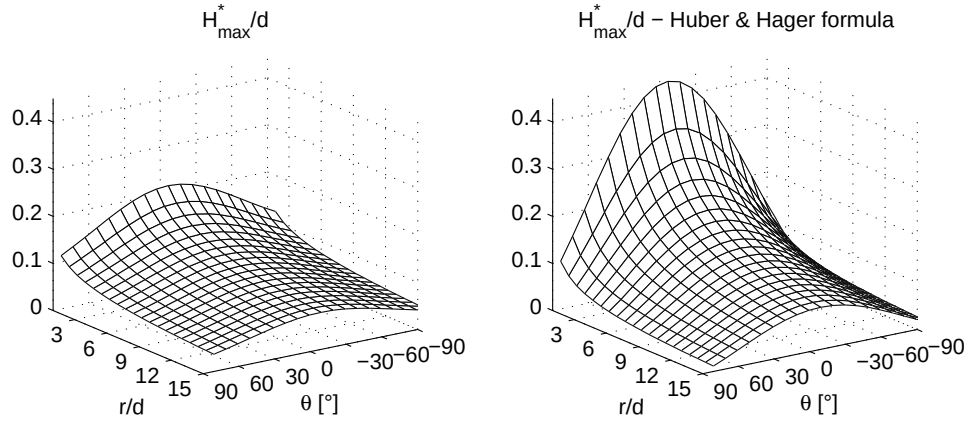

Figure 3.18: Comparison between the forecasting formulation of H_{max}/d defined in the present study (left panel), and Huber and Hager formula (right panel). Landslide parameters are: d=0.4 m; ρ_s=2200 Kg/m^3; w=1.2 m; h=0.18 m; l=0.42 m; α=26.0°; v=4.4 m/s.

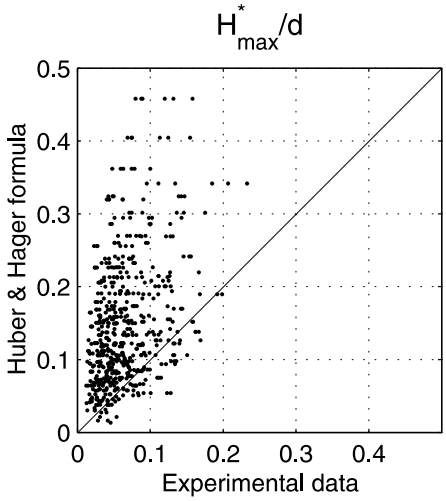

Figure 3.19: Application of Huber and Hager formula (1997) to experimental data from the present study.

3.4 Non-linear regression based on Artificial Neural Networks

3.4.1 Fundamentals of Artificial Neural Networks

Artificial Neural Networks (ANN) have been introduced as complex mathematical models able to reproduce the mechanism of thinking of the human mind. The basic idea is to spit the available information over a complex and multiple connected network. So far, they have been successfully applied in engineering, physics, economics and informatics. They are made up of simple elements working in parallel (neurons), linked by non linear transfer functions (synapses), which may be activated by the network adjustable parameters, which are the *ANN weights*. While information is stored in the neuron units, the synapses are used to connect neurons from different layers, thus propagating the input values to the output values, layer by layer. Synapses can be modelled in terms of a function containing a number of adjustable parameters, whose values are determined with the help of the available data set. Usually, ANN parameters are adjusted in order to minimize the errors between ANN outputs and observed outputs. Generally, an ANN model can be approximated by the following function, as:

$$y = y\left(\mathbf{x};\mathbf{w}\right) \tag{3.18}$$

where $\mathbf{x}=(x_1,..,x_N)^T$ represents the input data and $\mathbf{w}$ denotes the vector of ANN adjustable parameters. A neural network model can be regarded simply as a particular choice for the approximation function y. Figure 3.20 shows the ANN model used in the present work, which

is a fully-connected, feed-forwarded, multi-layer network (multi-layer perceptron), presenting N=6 input (i=1,...,N), M=6 hidden (j=1,...,M) and P=1 output units (k=1,...,P).

The output of the jth hidden units is obtained by first forming a weighted linear combination of the N input values, and adding a bias, such as:

$$a_j = \sum_{i=1}^{N} w_{ji}^{(1)} x_i + w_{j0}^{(1)} \tag{3.19}$$

Here $w_{ji}^{(1)}$ denotes a weight in the first layer, connecting the input i to hidden unit j, while $w_{j0}^{(1)}$ denotes the bias of the hidden unit j. The activation of hidden unit j is then obtained by inserting the linear sum a_j of equation 3.19 into an activation function $g(a_j)$, to give:

$$z_j = g(a_j) \tag{3.20}$$

The outputs of the network are obtained by transforming the activations of the hidden units using a second layer of weights processing elements. Thus, for each output unit k it is possible to construct a linear combination of the outputs of the hidden units of the form:

$$a_k = \sum_{j=1}^{M} w_{kj}^{(2)} z_j + w_{k0}^{(2)} \tag{3.21}$$

The activation of the k output unit is then obtained by transforming this linear combination using an activation function to give

$$y_k = \tilde{g}(a_k) \tag{3.22}$$

Here it has been used the notation $\tilde{g}(\cdot)$ for the activation function of the output units to emphasize that this need not be the same function as used for the hidden units. Combining equations 3.19 and 3.21 makes it possible to express the approximated function represented by the network as

$$y_k = \tilde{g}\left[\sum_{j=1}^{M} w_{kj}^{(2)} g\left(\sum_{i=1}^{N} w_{ji}^{(1)} x_i + w_{j0}^{(1)}\right) + w_{k0}^{(2)}\right] \tag{3.23}$$

In the present work, the ANN architecture is defined by the abbreviation $\mathrm{I}_i\mathrm{H}_j\mathrm{O}_k$, where the input (I), hidden (H) and output (O) layers contain a number of i, j and k neurons respectively. The ANN architecture used to model landslide generated waves data is of the form $\mathrm{I}_6\mathrm{H}_6\mathrm{O}_1$, as reproduced in Figure 3.20.

The model is trained to predict the values of output neurons as a function of the values of input neurons. In particular, it is adjusted making comparison between evaluated and target outputs (*supervised* training), while the error of the ANN is minimized adjusting the weights using an appropriate learning algorithm. So, an ANN model is characterized by its structure

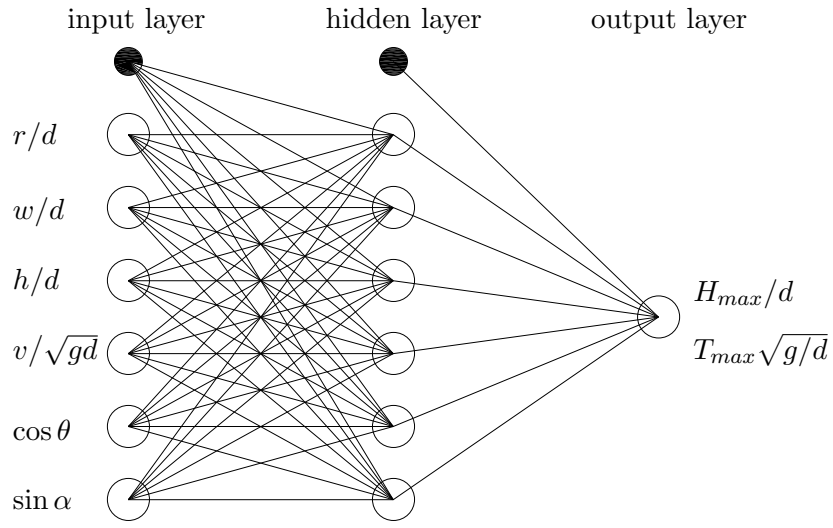

Figure 3.20: The ANN model used in the characterization of landslide generated waves.

as well as by the adopted transfer function and learning rule (i.e. optimization algorithm). In the present study a sigmoid function of the type $g(a_j) = 1/(1 + e^{-a_j})$ has been used to calculate neurons of the hidden layer, while a linear transfer function $g(a_j) = a_j$ has been used to calculate neurons of the output layer.

During the learning phase, by comparing all the predicted values $y_k(W)$ with the corresponding observed values ov, the weight matrices W of the interconnections are iteratively adjusted using the specific optimization algorithm adopted to minimize the network output error E, which is expressed as

$$E = \frac{1}{2} \sum_{p=1}^{P} \|y_k(W) - ov\|^2 \tag{3.24}$$

Each step of the iterative minimization process is called a *Learning Epoch*.

The learning rule adopted in the present study is the Levenberg-Marquardt algorithm (Levenberg, 1944; Marquardt, 1963) which seeks to minimize the error function while tries to keep small the step size between the old (W_{old}) and new value (W_{new}) of the weight matrices, which are updated at each Learning Epoch. The iteratively optimization process stops when a given tolerance between two subsequent estimates of the error function is reached. The Levenberg-Marquardt optimization algorithm can be expressed by the following equation:

$$W_{new} = W_{old} - \left[J^T J + \gamma I\right]^{-1} J^T E(W_{old}) \tag{3.25}$$

where J is the Jacobian matrix of the error, I is the unit matrix, and γ is a parameter that governs the step size.

3.4.2 Numerical details and applications

ANN mathematical theories introduced in the previous section had been implemented using the numerical Matlab computer language. The implemented numerical code was then applied to study subaerial landslide generated waves data, which were collected during the experimental tests carried out on the three dimensional model. The aim of the proposed ANN application was to gain a correlation rate higher than that one obtained using the standard regression approach previously introduced. ANN models were built considering the architecture $I_6H_6O_1$ sketched in Figure 3.20. It is to be stressed that a simple model architecture, with a reduced number of hidden layers (only one in the application at hand) containing few hidden neurons, reduces the problem of data overfitting. When a complicated ANN architecture is employed to gain high correlation rates, the side effect of the model application is the inaccuracy usually presented outside the experimental ranges. In that case, the data overfitting problem can be avoided adding selected or synthetically generated experimental data, thus to obtain a uniform dataset of values spread over the desired ranges.
In this work, six different ANN models $I_6H_6O_1$ were calibrated for each one of the dimensionless maximum wave height H_{max}/d, the related dimensionless wave period $T_{max}(g/d)^{0.5}$, the dimensionless crest (η_{1+}/d), trough (η_{1-}/d), height (H_1/d) and period ($T_1(g/d)^{0.5}$) of the first wave of the impulse generated group.

The first step was the testing of the ANN model capability in the interpretation of the physical problem under consideration. For this purpose, the models were firstly calculated using a certain percentage (say 80%) of available experimental data (learning data), and they were subsequently applied considering the 100% of data (testing data). As estimators of the correlation between observed and predicted parameters, the correlation parameter R^2 and the Mean Squared Error (MSE) were considered. The testing phase demonstrated that the same correlation rates are shown by ANN models considering both learning and testing data. Subsequently, the proposed ANN models were calculated using the 100% of available data. Figures 3.21, 3.22 and 3.23 present results of the modelling of each one of the considered parameters, using two different types of graphs. The first one (always on the left) is a scatter plot reporting forecasted ANN data, on the abscissa, while the observed data are reported on the ordinate. The second graph (always on the right) is a frequency distribution histogram of the classes of errors between observed and predicted parameters values.

The values of R^2 and MSE are reported on the top of each couple of plots. It is to be noted that results show a slight increased accuracy in correlating experimental input and output variables if compared to model accuracy shown by standard regression formulations. Further considerations can be made comparing ANN results to those obtained using the standard regression approach optimized using the Gauss-Newton method. Due to the fact that the same experimental data were considered in both the standard and the ANN approaches, it is possible to use ANN results as a test of goodness of the previously defined forecasting formulations. As introduced before, the complexity of the ANN model makes it particularly capable finding the best possible correlation using the available dataset, without any assumption on the physics of the considered phenomenon and on the role of each one of the input parameters on the output values. At this regard, it is clear that the ANN model would get higher improvements in the correlation rate of a parameter with a poor, or badly defined forecasting formula from the standard regression approach. It is to be stressed that ANN results present just slight improvements of the correlation rates if compared to those of the forecasting formulations defined in the previous section, demonstrating the high correlation rates and accuracy of the previously introduced forecasting formulations.

3.5 Discussion of obtained results

In a first step, the characterization of subaerial landslide generated waves from carried out experiments was successfully obtained applying the Wavelet Transform (WT) analysis. A WT analysis numerical code was implemented on purpose for this application. For the first time in literature, WT was used to define impulse waves dispersive features while propagating in a two dimensional wave flume, recognizing different types of generated impulse waves. Moreover, the reflection coefficient from an overflow structure and seiche waves of the flume were studied. Some of results were published in the paper “Application of wavelet transform analysis to landslide generated waves”, Panizzo et al. (2002).

Experimental results from the three dimensional model were analyzed in order to gain forecasting formulations, following two different approaches. The former, which is the classic regression approach, was used to define forecasting formulations relating the principal features of impulse waves with the experimental parameters of the landslide model kinematic and geometry, and the water basin. The latter, which is a Neural Network approach, was used to test the potentiality of correlation between the considered experimental parameters. Forecasting formulations defined with the classic regression approach showed very satisfactorily correlations R^2 between observed and forecasted parameters. As far as the maximum

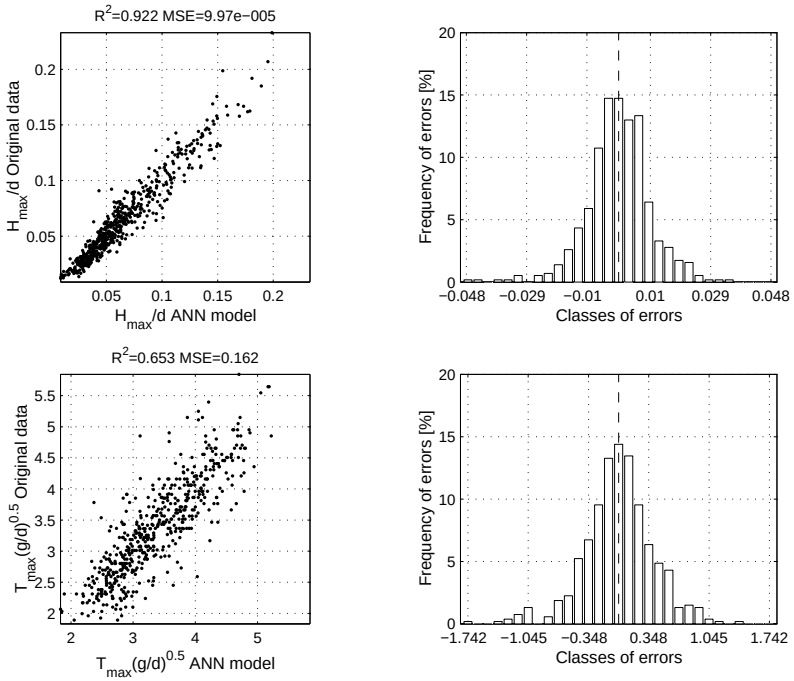

Figure 3.21: Dimensionless parameters H_{max}/d (first row) and $T_{max}(g/d)^{0.5}$ (second row). Left panels show the scatter plots of the forecasted values, on the abscissa, over measured values, on the ordinate. Right panels show the frequency distribution histogram of the classes of errors between observed and predicted parameters values.

generated wave height is concerned, which is considered the most important feature of impulse generated waves, Figure 3.14 reported the influence of any given input parameter. Analyzing the input parameters functions reported in Figure 3.14, and taking into account the experimental ranges, it can be noticed that the dimensions of the landslide front (parameters w and h) play a predominant role, while impulse waves height considerably vary over directions θ and distances r from the impact point. Highest waves are expected with increasing the impact velocity v and decreasing the angle α of the sliding slope with the horizontal, but, if compared to other parameters, v and α show a minor influence on the maximum generated wave height.

As far as the ANN approach is concerned, Figure 3.24 reports a comparison of the correlation parameter R^2 between formulations defined with the classic regression approach (white bars) and results obtained using the ANN approach (black bars). While ANN models present always highest accuracy, it is to be stressed that no information about the physics of the phenomenon can be provided by the ANN approach.

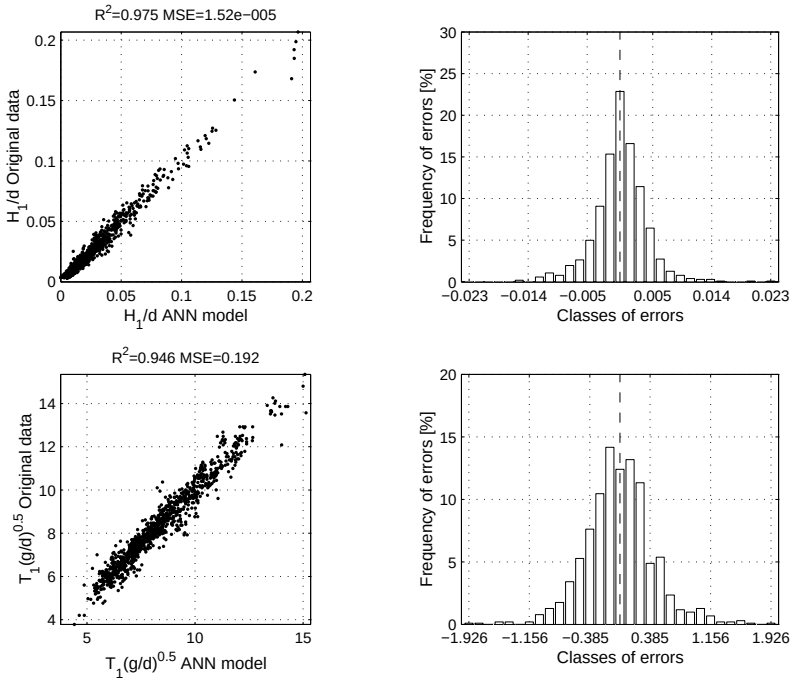

Figure 3.22: Dimensionless parameters H_1/d (first row) and $T_1(g/d)^{0.5}$ (second row). Refer to the caption of Figure 3.21 for notation.

The comparison of obtained results with those presented by past studies showed a substantial agreement with the work of Kamphuis and Bowering (1972), while some discrepancies exist with the work of Huber and Hager (1997). It is to be noticed that Huber and Hager (1997) generated impulse waves in a three dimensional water body considering granular landslides. In the present work, with the aim of obtaining the highest possible effects, solid landslides with zero porosity were considered. However, contrarily to what expected, the application of Huber and Hager (1997) formulation to experimental data carried out in the present work showed a substantial overestimation of forecasted values. In particular, Figure 3.18 reports the comparison between the forecasting formulation defined in the present study and that one defined by Huber and Hager. In this case, the latter presents forecasted values which are more than twice those forecasted by the former. Moreover, Figure 3.19 shows results of the application of Huber and Hager (1997) formulation to all experimental data obtained in the present study: the scatter plot confirms the tendency in overestimating the forecasts, some of them five times greater than real values.

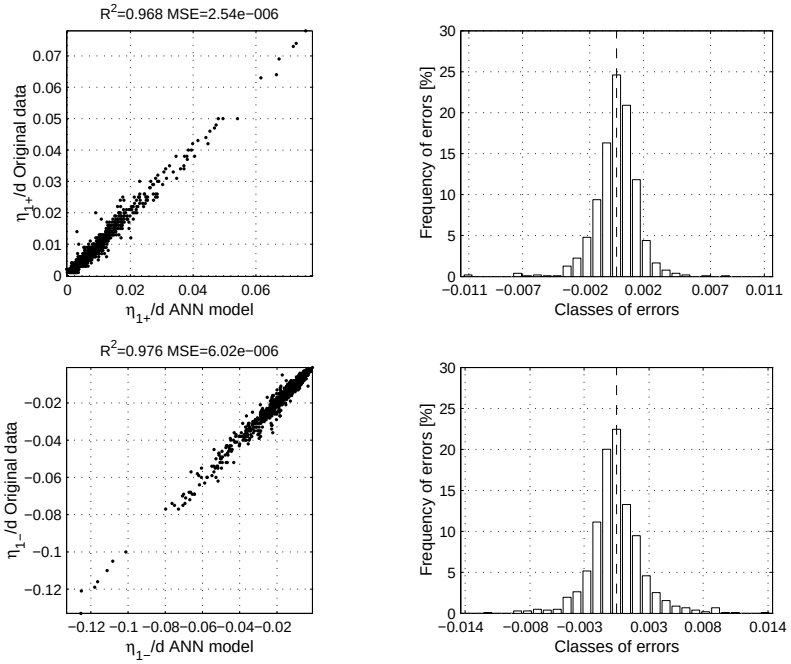

Figure 3.23: Dimensionless parameters η_{1+}/d (first row) and η_{1-}/d (second row). Refer to the caption of Figure 3.21 for notation.

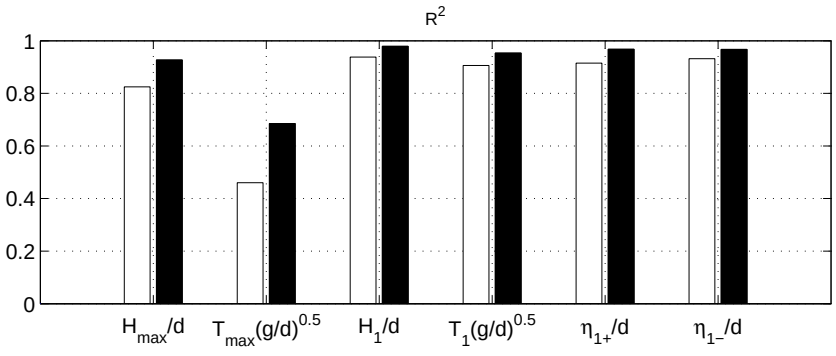

Figure 3.24: Comparison of the correlation parameters R^2 between formulations from classic regression (white bars) and ANN models (black bars).

Chapter 4

Numerical modelling of landslide generated waves

4.1 Introduction

Computational Hydraulics is a field presenting ever more challenging problems. The great development of computer technology of the last two decades allowed the facing of hydraulics two and three dimensional phenomena which before were studied by means of physical model experiments. For instance, the field of ocean wave numerical modelling recently presented successful studies on breaking waves, wave and structures interaction, breakwater wave overtopping. Also the well known water entry problem (involving the subaerial landslide generated wave problem) has been recently faced by many researchers. Amongst the others, three numerical models were spreadly implemented and applied in the scientific community. They are the Boundary Element method (BEM), the Volumes of Fluids (VOF) method, and the Smoothed Particle Hydrodynamics (SPH).

The BEM method is a numerical solutions of Fully Nonlinear Potential Flow equations, simulating the water motion by means of panels opportunely set along the boundaries of the computational domain. The basic hypothesis of the method is the compactness of the considered water field, i.e. the line of panels can assume any type of deformations, without intersections, and without presenting separation of the water body in multiple sub-domains. A detailed description of the BEM method, along with applications in ocean wave modelling, can be found in the works of Grilli et al. (1994), Grilli and Horrillo (1997), Watts et al. (2001).

VOF, introduced by Hirt and Nichols (1981), is a method to track the free-surface in Reynolds Averaged Navier Stokes (RANS) numerical models. Recently, RANS codes have been successfully applied in the study of the wave-breaking process and wave and structure

interactions. Usually, the k–ε technique is employed as turbulence closure model. A complete description of the VOF method can be found in the works of Hirt and Nichols (1981) and Liu and Lin (1997).

The SPH model was originally introduced by Lucy (1977) and Gingold and Monaghan (1977) in astrophysics. Since then it has been applied in many other areas, such as impact penetration into solids (Johnson and Beissel, 1996), fluid dynamics, including viscous flows Takeda et al. (1994), free surface flows (Monaghan, 1994; Dalrymple et al., 2001), multiphase flows (Colagrossi and Landrini, 2003), and impact generated waves (Monaghan and Kos, 2000).

The reason why to apply a particle method instead of a finite difference, a finite element or a finite volume scheme is the fact that SPH is well suited to simulate free surface flows and fluid structures interaction with rapid changes of the flow field, and sudden formation of bores and splashes, such as in the water entry problem. Moreover, the computational water domain is allowed to present separations into subdomains, as in the case of drops and splashes. So, in the present research program, the above mentioned reasons justify the choice of SPH as the proper numerical method to model subaerial landslide generated waves. In hydraulics applications, the main advantage of the SPH model is the great capability to deal with free surface flows (Monaghan, 1994) without the assumption of a hydrostatic pressure. Unfortunately, SPH codes presents the disadvantage of the great computational times: at this regard, some parallel versions of the original SPH formulation have been proposed (Morris et al., 1999).

In the present work the SPH numerical model has been chosen to simulate subaerial landslide generated waves. In particular, a parallel version of the original SPH algorithm was implemented on purpose using the FORTRAN computer language. An original technique for the problem of reducing the computational time by optimizing the search of interacting particles is here proposed. The implemented SPH model is firstly tested using physical model experiments found in the literature, and then it is applied to simulate two dimensional physical model experiments on subaerial landslide generated waves performed within the present work.

4.2 Smoothed Particle Hydrodinamics

4.2.1 Fundamentals

The two basic ideas of SPH to solve the evolution equations are that every flow characteristic is smoothed over the spatial domain by using an appropriate kernel function W, and that the smoothed flow is approximated by particles, which time evolution is governed by a Lagrangian

scheme. There are no constraints imposed either to the geometry of the system or in how far it may evolve from the initial conditions. The equations of fluid dynamics are transformed into integral equations through the use of W, which presents a finite interaction radius equal to $2h$. The kernel is indeed a weighting function that smooths out field contributions defining the value of a physical variable, say A, at a certain point $\mathbf{r}$. In this optic, the kernel estimate of A is defined as:

$$A(\mathbf{r}) = \int_{space} A(\mathbf{r}')W(\mathbf{r}-\mathbf{r}', h)\, d\mathbf{r}' \tag{4.1}$$

The Kernel function W has to satisfy the following two constraints:

$$\int_{space} W(\mathbf{r}-\mathbf{r}', h)\, d\mathbf{r}' = 1 \tag{4.2}$$

$$\lim_{h\to 0} W(\mathbf{r}-\mathbf{r}', h)\, d\mathbf{r}' = \delta(\mathbf{r}-\mathbf{r}') \tag{4.3}$$

In other words, W is a smoothing function with a compact support, approximating a delta-function.

In SPH numerical implementation, the water domain is represented by a certain finite number of particles, carrying the physical variable at the points occupied by their volumes. So, eq. 4.1 is approximated by a summation interpolant:

$$A(\mathbf{r}) = \sum_b m_b \frac{A_b}{\rho_b} W(\mathbf{r}-\mathbf{r}_b, h) \tag{4.4}$$

where the index b is referred to any field particle, with mass m_b, density ρ_b, position $\mathbf{r}_b$, and velocity $\mathbf{v}_b$. The error arising between the discrete and the continuous version of the basic SPH equation (eq. 4.4 and eq. 4.1) is related on how disordered the particles are.
Making reference to the kernel function W, and to the above introduced equations, it is possible to write the smoothed gradient of the generic field variable A, which is:

$$\nabla_{\mathbf{r}} A(\mathbf{r}) = \int \nabla_{\mathbf{r}'} A(\mathbf{r}')W(\mathbf{r}-\mathbf{r}', h)\, d\mathbf{r}' \tag{4.5}$$

Assuming that:

$$u = W(\mathbf{r}-\mathbf{r}', h) \Rightarrow du = \nabla_{\mathbf{r}'} W(\mathbf{r}-\mathbf{r}', h)\, d\mathbf{r}' \tag{4.6}$$

$$dv = \nabla_{\mathbf{r}'} A(\mathbf{r}')\, d\mathbf{r}' \Rightarrow v = A(\mathbf{r}') \tag{4.7}$$

and integrating by parts, eq. 4.5 is rewritten as:

$$\nabla_{\mathbf{r}} A(\mathbf{r}) = A(\mathbf{r}') W(\mathbf{r}-\mathbf{r}', h)\,|_{Surface} - \int A(\mathbf{r}')\,\nabla_{\mathbf{r}'} W(\mathbf{r}-\mathbf{r}', h)\, d\mathbf{r}' \tag{4.8}$$

The surface integral in eq. 4.8 is usually neglected in SPH numerical implementations, as demonstrated by Schlatter (1999), if boundaries are made up of smoothed particles interacting with normal fluid particles. The minus sign in 4.8 can be replaced by a plus sign if the gradient is referred to the particle at the point $\mathbf{r}$.

$$\nabla_{\mathbf{r}} A(\mathbf{r}) = \int A(\mathbf{r}')\nabla_{\mathbf{r}} W(\mathbf{r}-\mathbf{r}', h)\, d\mathbf{r} \tag{4.9}$$

In SPH numerical implementations, the gradient approximation is written as a finite summation over all particles:

$$\nabla_{\mathbf{r}} A(\mathbf{r}) = \sum_{b=1}^{N} V_b A_b \nabla_{\mathbf{r}} W(\mathbf{r}-\mathbf{r}_b, h) \tag{4.10}$$

Hereinafter notation will be simplyfied referring to generic particles a and b, being a the reference particle, and b one of the other particles in the fluid domain. The rewritten version of SPH equations are:

$$A_a = \sum_{b=1}^{N} V_b A_b W_{ab} \tag{4.11}$$

$$\nabla_a A_a = \sum_{b=1}^{N} V_b A_b \nabla_a W_{ab} \tag{4.12}$$

where $W_{ab} = W(\mathbf{r}_a - \mathbf{r}_b, h)$, $V_i = m_i/\rho_i$ and ∇_i implies spatial derivative with respect to coordinates of the generic particle i. Although eq. 4.10 gives a correct estimate of the gradient of A, in numerical simulations it is preferable to use the following:

$$\nabla_{\mathbf{r}} A = \frac{1}{\rho}\left[\nabla_{\mathbf{r}}(\rho A) - A\nabla_{\mathbf{r}}\rho\right] \tag{4.13}$$

Making reference to the above introduced equations and notation, it is possible to write eq. 4.13 in the summation form:

$$\nabla_a A = \frac{1}{\rho_a}\left[\sum_{b=1}^{N} m_b A_b \nabla_a W_{ab} - A_a \sum_{b=1}^{N} m_b \nabla_a W_{ab}\right] = \frac{1}{\rho_a}\sum_{b=1}^{N} m_b (A_b - A_a)\,\nabla_a W_{ab} \tag{4.14}$$

Kernels

The principal features required to the kernel function are to be differentiable almost once and to approximate a Dirac delta function. In addition, the kernel must have continuous second derivative so as to keep the integral slowly varying. One of the standard kernel is the cubic spline kernel, also called the Beta-spline kernel (Monaghan and Lattanzio, 1985), and it is given by:

$$W(\mathbf{r},h)=\frac{\sigma}{h^{\nu}}\begin{cases}\left(4-6s^2+3s^3\right), & \text{if } 0\leq s\leq 1\\ \left(2-s\right)^3, \text{if } 1\leq s\leq 2\\ 0, \text{otherwise}\end{cases} \tag{4.15}$$

where $s=r/h$, ν is the number of dimensions and σ is the normalization factor with values $\frac{5}{14\pi}$, and $\frac{1}{4\pi}$ in two and three dimensions, respectively. One of the advantages of using eq. 4.15 instead of a Gaussian is that it has a compact support (i.e. it is equal to zero for $s>2$) and numerical computations are reduced.
A higher order polynomial kernel is the quintic spline kernel, introduced by Morris et al. (1997):

$$W(\mathbf{r},h)=\frac{\sigma}{h^{\nu}}\begin{cases}\left(3-s\right)^5-6\left(2-s\right)^5+15\left(1-s\right)^5, & \text{if } 0\leq s\leq 1\\ \left(3-s\right)^5-6\left(2-s\right)^5, \text{if } 1\leq s\leq 2\\ \left(3-s\right)^5, \text{if } 2\leq s\leq 3\\ 0, \text{otherwise}\end{cases} \tag{4.16}$$

and the normalization factor assumes values equal to $\frac{7}{478\pi}$, and $\frac{3}{359\pi}$ in two and three dimensions, respectively.

Another kernel function was proposed by Johnson et al. (1996), and presents a function that prevents particle clustering in compression problems:

$$W(\mathbf{r},h)=\frac{1}{\pi h^2}\left[\frac{3}{8}s^2-\frac{3}{2}s+\frac{3}{2}\right], \text{if} 0\leq s\leq 2 \tag{4.17}$$

and it is written for 2-D simulations. The derivative of the kernel function is:

$$W'(\mathbf{r},h)=\frac{1}{\pi h^3}\left[\frac{3}{4}s-\frac{3}{2}\right], \text{if} 0\leq s\leq 2 \tag{4.18}$$

Figure 4.1 presents a comparison between the cubic spline kernel and the Quadratic smoothing function introduced by Johnson. As far as the kernel is conceived to solve the particle clustering problem, it presents a discontinuous second derivative and it makes the

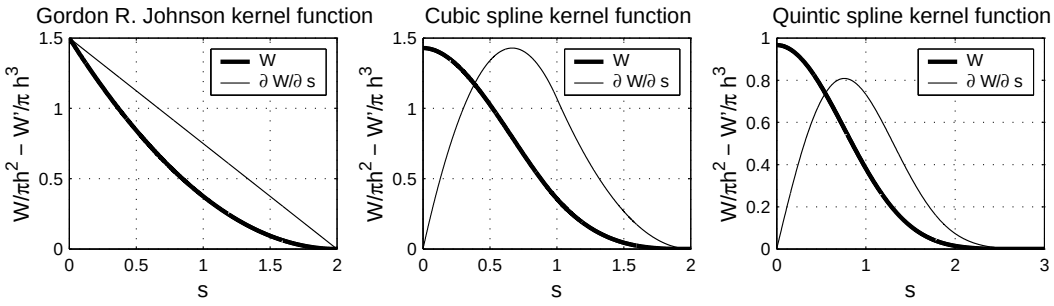

Figure 4.1: Some of the most widespread kernel functions in SPH models: Gordon R. Johnson function, on the left; cubic spline function, on the middle; quintic spline kernel function, on the rigth.

kernel more dispersive than the cubic spline and more sensitive to particle disorder (Monaghan, 2000).

In the present work, the previously introduced kernel functions were all implemented and tested. A couple of good reasons led to employ the kernel function proposed by Johnson et al. (1996). Firstly, the cubic spline and the quintic spline kernel functions have to be corrected (see section *Kernelcorrection*) to handle impacts and high values of velocity in the flow field without presenting the problem of particle clustering. Moreover, using the spline kernels increases the computational time, due to the multiple check used to define which part of the spline function it is to be considered.

Equation of state

Fluids simulated by using the SPH are compressible, as a stiff equation of state is used. This is to avoid solving the Poisson equation for incompressible fluids at each time step. The equation of state used in the present work is taken from Batchelor (1999), and is:

$$p = B\left[\left(\frac{\rho}{\rho_o}\right)^{\gamma} - 1\right] \tag{4.19}$$

with $\gamma = 7$, $\rho_o = 1000.0 Kg/m^3$ is the initial density of the fluid, B is a constant chosen to make sure the Mach number $M = \frac{u}{c}$ is small enough to avoid fast sound waves which would require small Δt. B is defined considering that the Mach number has to be $M < 0.2$. In simulations that will be presented in the present work, the Mach number was set $M = 0.1$, and so:

$$M^2 = \frac{u^2}{c^2} = 0.01 \tag{4.20}$$

According to the definition of sound speed under constant entropy:

$$c^2 = \frac{\partial p}{\partial \rho} \tag{4.21}$$

which results in:

$$c^2 = \frac{\partial p}{\partial \rho} = \frac{\gamma B}{\rho_o}\left(\frac{\rho}{\rho_o}\right)^{\gamma-1} \tag{4.22}$$

the constant B is defined assuming a value of the velocity u which should be characteristic of the problem at hand. In free surface studies, u is taken equal to $\sqrt{2gH}$, being H a representative depth (Monaghan, 1994). In this approach the sound speed c is much slower than the actual speed of sound in the water.

Continuity equation

Making reference to eq. 4.11, the density of the generic particle a can be calculated using the following equation:

$$\rho_a = \sum_{b=1}^{N} m_b W_{ab} \tag{4.23}$$

however, this equation requires an extra loop over all particles before it can be used in the calculations. A better numerical equation can be formulated using the SPH version of the continuity equation:

$$\frac{d\rho}{dt} = -\rho \nabla \cdot \mathbf{v} \tag{4.24}$$

It is possible to calculate the right hand side of eq. 4.24 in either a straightforward fashion, to get:

$$-\rho \nabla \cdot \mathbf{v} = \sum_{b=1}^{N} \frac{m_b}{\rho_b} \mathbf{v}_b \cdot \nabla_a W_{ab} \tag{4.25}$$

As introduced with eq. 4.13, it is preferable to use the following expression to evaluate the gradient of a given function:

$$\nabla \cdot \mathbf{v} = \frac{\nabla \cdot (\rho \mathbf{v}) - \mathbf{v} \cdot \nabla \rho}{\rho} \tag{4.26}$$

which yields a more accurate numerical result (Schlatter, 1999). So, the continuity equation becomes:

$$\begin{aligned} \frac{d\rho_a}{dt} &= \sum_{b=1}^{N} m_b (\mathbf{v}_a - \mathbf{v}_b) \nabla_a W_{ab} \\ &= \sum_{b=1}^{N} m_b \mathbf{v}_{ab} \nabla_a W_{ab} \end{aligned} \tag{4.27}$$

where $\mathbf{v}_{ab} \equiv \mathbf{v}_a - \mathbf{v}_b$.

Momentum equation

The momentum conservation equation for a non-viscous fluid in the absence of gravity is given by Euler's equation:

$$\frac{d\mathbf{v}}{dt} = -\frac{1}{\rho}\nabla P \tag{4.28}$$

By using the above introduced equations and notation, it is possible to write the Euler's equation in the SPH formalism. Moreover, rewriting the pressure gradient as explained before, eq. 4.28 turns into:

$$\frac{\nabla P}{\rho} = \nabla\left(\frac{P}{\rho}\right) + \frac{P}{\rho^2}\nabla\rho \tag{4.29}$$

Considering the SPH discrete version of eq. 4.29, the first term can be written as:

$$\begin{aligned}\nabla_a\left(\frac{P_a}{\rho_a}\right) &= \sum_{b=1}^{N} \frac{m_b}{\rho_b}\frac{P_b}{\rho_b}\nabla_a W_{ab} \\ &= \sum_{b=1}^{N} m_b \frac{P_b}{\rho_b^2}\nabla_a W_{ab}\end{aligned} \tag{4.30}$$

while the second term can be written as:

$$\begin{aligned}\nabla_a\rho_a &= \sum_{b=1}^{N} \frac{m_b}{\rho_b}\rho_b\nabla_a W_{ab} \\ &= \sum_{b=1}^{N} m_b\nabla_a W_{ab}\end{aligned} \tag{4.31}$$

Combining terms yields:

$$\begin{aligned}\frac{\nabla_a P}{\rho_a} &= \sum_{b=1}^{N} m_b\frac{P_b}{\rho_b^2}\nabla_a W_{ab} + \frac{P_a}{\rho_a^2}\sum_b m_b\nabla_a W_{ab} \\ &= \sum_{b=1}^{N} m_b\left(\frac{P_b}{\rho_b^2} + \frac{P_a}{\rho_a^2}\right)\nabla_a W_{ab}\end{aligned} \tag{4.32}$$

Thus, according to SPH formalism and equations, the Euler's equation is rewritten as:

$$\frac{d\mathbf{v}_a}{dt} = -\sum_{b=1}^{N} m_b\left(\frac{P_b}{\rho_b^2} + \frac{P_a}{\rho_a^2}\right)\nabla_a W_{ab} \tag{4.33}$$

Artificial viscosity

So far, SPH equations have been derived for non-viscous fluids. The introduction of a viscous term in the SPH momentum equation is not only necessary if a viscid fluid or a no-slip boundary condition have to be considered, but also to prevent inter-particle penetration and

to improve the code numerical stability. There are many forms of artificial viscosity that have been proposed for the SPH method (Lucy, 1977; Gingold and Monaghan, 1983) but the most common is to add the following viscous pressure term into the momentum equation:

$$\frac{d\mathbf{v}_a}{dt} = -\sum_{b=1}^{N} m_b \left(\frac{P_a}{\rho_a^2} + \frac{P_b}{\rho_b^2} + \prod_{ab} \right) \nabla_a W_{ab} \tag{4.34}$$

where $\prod_{ab}$ is the artificial viscous pressure and is defined as:

$$\prod_{ab} = \begin{cases} \frac{-\alpha c_{ab} \mu_{ab} + \beta \mu_{ab}^2}{\rho_{ab}}, & \text{if } \mathbf{v}_{ab} \cdot \mathbf{r}_{ab} < 0, \\ 0, & \text{otherwise} \end{cases} \tag{4.35}$$

with:

$$\mu_{ab} = \frac{h \mathbf{v}_{ab} \cdot \mathbf{r}_{ab}}{\mathbf{r}_{ab}^2 + \eta^2}$$

and $\rho_{ab} = \frac{1}{2}(\rho_a + \rho_b)$, $c_{ab} = \frac{1}{2}(c_a + c_b)$, c_a and c_b are the sound speed at particles a and b respectively, h is the smoothing length, $\eta^2 = 0.01h^2$, and α and β are constants dependent on the particular type of simulation being run. Common values for α and β in astrophysical simulations are 1.0 and 2.0, respectively. In general hydraulic problems α assumes values in the range $[0.01 - 0.1]$, while β is usually set equal to zero (Monaghan, 1994). In this optic, the artificial viscosity is introduced in the SPH model as an artificial pressure between particles. Moreover, it is to be noted that the linear term in eq. 4.35 produces a shear and bulk viscosity (Monaghan, 1985) while the quadratic term handles high Mach number shocks by increasing the artificial pressure proportionally to ρv^2 .
Other versions of viscosity equations for SPH codes have been proposed, aiming at numerically reproducing the Navier-Stokes equation: details can be found in the works of Morris (1996), and Takeda et al. (1994).

XSPH variant

For free surface problems, a numerical filter was proposed by Monaghan (1994). The correction modifies the update of the particles motion by correcting the velocity according to the following expression:

$$\frac{dv_a}{dt} = v_a + \varepsilon \Delta v_a \tag{4.36}$$

where

$$\Delta v_a = \sum_{b=1}^{N} \frac{m_b (v_b - v_a)}{\bar{\rho}_{ab}} W_{ab} \tag{4.37}$$

Indeed, the XSPH correction represents a smoothing of the velocity field considering the neighboring particles velocities. It is particularly efficient when fast flow fields or impacts are considered. The coefficient ε has to be chosen in the range [0; 1].

4.2.2 Numerical recipes

Although the SPH method has been completely described in the previous section, several numerical techniques are currently used in order to improve the numerical accuracy and to reduce the computational time. In this section the most used and recent numerical techniques presented in SPH numerical codes are introduced and compared.

Time stepping and particle motion

The time stepping defines the time integration used to update particle positions. The most common time stepping schemes used in SPH literature are the *leap-frog* explicit scheme, and the *predictor-corrector* scheme which conserve linear and angular momentum exactly (Monaghan, 1994; Dalrymple et al., 2001). According to the *leap frog* scheme, the velocity at point a are at first found as:

$$\mathbf{v}_a^{n+(1/2)} = \mathbf{v}_a^{n-(1/2)} + \overline{\Delta t}\mathbf{a}_a^n \tag{4.38}$$

Then the particle position are updated as

$$\mathbf{x}_a^{n+1} = \mathbf{x}_a^n + \Delta t^{n+1}\mathbf{v}_a^{n+(1/2)} \tag{4.39}$$

where $\overline{\Delta t} = \frac{1}{2}\left(\Delta t^n + \Delta t^{n+1}\right)$ and $\mathbf{a}_a^n$ is the acceleration vector at point a using the equilibrium equation.

The *predictor corrector* scheme is applied to a differential equation of the form:

$$\frac{d\mathbf{v}}{dt} = -\Gamma\mathbf{v} + F \tag{4.40}$$

the predictor step predicts to the midpoint, so that, with a time step equal to Δt, the associated $\mathbf{v}$ is:

$$\mathbf{v}^{n+1/2} = \frac{\mathbf{v}^n + 0.5\Delta t \cdot F^n}{1 + 0.5\Gamma\Delta t} \tag{4.41}$$

while the corrector step is:

$$\mathbf{v}^{n+1/2} = \frac{\mathbf{v}^n + 0.5\Delta t \cdot F^{n+1/2}}{1 + 0.5\Gamma\Delta t} \tag{4.42}$$

the value of $\mathbf{v}$ at the end of the step is then:

$$\mathbf{v}^{n+1} = 2\mathbf{v}^{n+1/2} - \mathbf{v}^{n} \tag{4.43}$$

In order to satisfy the Courant-Friedrichs-Levy (CFL) stability the following expression was used to determine Δt:

$$\Delta t = C_{FL} \frac{h_{\min}}{\max_a(c_a + \|\mathbf{v}_a\|)} \tag{4.44}$$

where $0 < C_{FL} \leq 1$ is the Courant number and $c = \sqrt{\gamma k/\rho}$ is the speed of sound. Unfortunately, the use of the real bulk modulus of water in the equation of state would result in extremely small timesteps and therefore lenghty computations. In order to prevent this, an artificial smaller bulk modulus is typically used. This is determined by choosing a small ratio between the maximum speed of the fluid and the speed of the sound and then evaluating k as $k = c_{\max}^2 \rho/\gamma$, where $c_{\max} = m \|\mathbf{v}\|_{\max}$. Usually m is taken between 10 and 1000.

Corrected SPH

A periodic correction of the kernel function W is necessary in SPH hydraulics computations, where a finite domain and a free surface are often part of the computational domain. Particles near boundaries or the free surface have a kernel smoothing function truncated due to the absence of neighboring particles. The condition of consistency of W (eq. 4.2) fails. However it is still possible to handle these situation by opportunely correcting the kernel function W itself or its gradient. In the followings the most used techniques to avoid errors from a corrupted interpolating function will be introduced in details, making reference to the works of Randles and Libersky (1996), Bonet and Lok (1999) and Bonet and Kulasegaram (2002).

Kernel correction

The simplest possible correction involves the kernel function. A kernel correction technique was proposed by Li and Liu (1996) and Liu et al. (1997) with the aim to correctly interpolate polynomial functions. For instance, taking in consideration the kernel approximation of an arbitrary function $f(\mathbf{r})$, defined as:

$$f(\mathbf{r}) = \int_{space} f(\mathbf{r}') W(\mathbf{r} - \mathbf{r}', h)\, d\mathbf{r}' \tag{4.45}$$

by a proper selection of the kernel function, it is possible to ensure that polynomials up to a given degree k are correctly reproduced by eq. 4.45. To demonstrate this, it is sufficient

considering a Taylor series expansion about x of the given function, such as:

$$f\left(\mathbf{r}'\right) = f\left(\mathbf{r}\right) + f'\left(\mathbf{r}\right)\left(\mathbf{r}' - \mathbf{r}\right) + \frac{1}{2}f''\left(\mathbf{r}\right)\left(\mathbf{r}' - \mathbf{r}\right)^2 + ... \tag{4.46}$$

Substituting into eq. 4.45, it results:

$$\langle f\left(\mathbf{r}\right)\rangle = f\left(\mathbf{r}\right)\int\limits_{space} W\left(\mathbf{r}' - \mathbf{r}\right)d\mathbf{r}' - f'\left(\mathbf{r}\right)\int\limits_{space}\left(\mathbf{r}' - \mathbf{r}\right)W\left(\mathbf{r}' - \mathbf{r}\right)d\mathbf{r}' + ... \tag{4.47}$$

If the following conditions are satisfied,

$$\int\limits_{space} W\left(\mathbf{r}' - \mathbf{r}\right)d\mathbf{r}' = 1$$

$$\int\limits_{space}\left(\mathbf{r}' - \mathbf{r}\right)W\left(\mathbf{r}' - \mathbf{r}\right)d\mathbf{r}' = 0 \tag{4.48}$$

the given function $f(\mathbf{r})$ has an approximation which is said to be of the second order. Considering a velocity field function, defined as:

$$\mathbf{v}\left(\mathbf{r}\right) = \sum_{b=1}^{N} V_b \mathbf{v}_b \tilde{W}_b\left(\mathbf{r}\right) \tag{4.49}$$

with $V_b = m_b/\rho_b$, it is possible to employ a corrected kernel function $\tilde{W}$ to gain the above defined accuracy. The correction at a first order is defined as:

$$\tilde{W}_b\left(\mathbf{r}\right) = W_b\left(\mathbf{r}\right)\alpha\left(\mathbf{r}\right)\left[1 + \beta\left(\mathbf{r}\right)\cdot\left(\mathbf{r} - \mathbf{r}_b\right)\right] \tag{4.50}$$

Where parameters $\alpha\left(\mathbf{r}\right)$ and $\beta\left(\mathbf{r}\right)$ are evaluated with the constraint that a given velocity field is correctly interpolated by the SPH model, as:

$$\mathbf{v}_0 + \mathbf{v}_1\cdot\mathbf{x} = \sum_{b=1}^{N} V_b\left(\mathbf{v}_0 + \mathbf{v}_1\cdot\mathbf{r}\right)\tilde{W}_b\left(\mathbf{r}\right) \tag{4.51}$$

Since both $\mathbf{v}_0$ and $\mathbf{v}_1$ are arbitrary vectors, the following consistency conditions are to be satisfied:

$$\sum_{b=1}^{N} V_b \tilde{W}_b\left(\mathbf{r}\right) = 1 \tag{4.52}$$

$$\sum_{b=1}^{N} V_b\left(\mathbf{r} - \mathbf{r}_b\right)\tilde{W}_b\left(\mathbf{r}\right) = 0 \tag{4.53}$$

These equations, derived from 4.48, enable to find the corrected values of $\alpha(\mathbf{r})$ and $\beta(\mathbf{r})$. Substituting eq. 4.50 into eq. 4.53 gives, after some algebra:

$$\beta(\mathbf{r}) = \left[\sum_{b=1}^{N} V_b(\mathbf{r}-\mathbf{r}_b) \otimes (\mathbf{r}-\mathbf{r}_b) W_b(\mathbf{r})\right]^{-1} \sum_{b=1}^{N} V_b(\mathbf{r}_b-\mathbf{r}) W_b(\mathbf{r}) \tag{4.54}$$

Once $\beta(\mathbf{r})$ is estimated, $\alpha(\mathbf{r})$ is obtained by substitution of eq. 4.50 into eq. 4.52:

$$\alpha(\mathbf{r}) = \left[\sum_{b=1}^{N} V_b[1+\beta(\mathbf{r})(\mathbf{r}-\mathbf{r}_b)] W_b(\mathbf{r})\right]^{-1} \tag{4.55}$$

The kernel correction proposed above ensures that linear velocity field are exactly interpolated: however it is cumbersome in the SPH loop. A simpler way to correct the kernel function is obtained considering constant, rather than linear, correction: this is equivalent to taking $\beta(\mathbf{r}) = 0$. So, eqs. 4.55 and 4.50 lead to:

$$\mathbf{v}(\mathbf{r}) = \frac{\sum_{b=1}^{N} V_b \mathbf{v}_b W_b(\mathbf{r})}{\sum_{b=1}^{N} V_b W_b(\mathbf{r})} \tag{4.56}$$

The denominator of eq. 4.56 is the parameter $\alpha(\mathbf{r})$. This correction of the kernel function W can be expressed by the following equation:

$$\tilde{W}_b(\mathbf{r}) = \frac{W_b(\mathbf{r})}{\sum_{b=1}^{N} V_b W_b(\mathbf{r})} \tag{4.57}$$

and coincides with the interpolation technique proposed by Shepard (1968). Even if simple and easy to implement, it ensures great improvements in SPH simulations.

It is worthwhile mentioning another kernel correction technique, introduced by Bonet and Lok (1999), which involves the modification of the kernel gradient by a correction matrix. In all SPH simulations presented in the following sections the Shepard kernel correction, expressed by eq. 4.57, has been used.

Correction of tensile instability

In order to prevent particles clustering, Monaghan (2000) proposed a modification of the cubic spline based kernel, by introducing a suitable function which increases as the separation between particles decreases:

$$f_{ab} = \frac{W(r_{ab})}{W(\Delta p)} \tag{4.58}$$

where Δp is the initial particle spacing. The correction of "tensile instability" is introduced by replacing:

$$\frac{P_a}{\rho_a^2} + \frac{P_b}{\rho_b^2} + \Pi_{ab} \tag{4.59}$$

with

$$\frac{P_a}{\rho_a^2} + \frac{P_b}{\rho_b^2} + \Pi_{ab} + R f_{ab}^n \tag{4.60}$$

Monaghan (2000) suggests to assume the following values for the variables: $n = 4$, $h = 1.3\Delta p$, while the factor R could be determined as a function of the pressure. So that:

$$R = R_a + R_b \tag{4.61}$$

and factor R_a is determined by the rule (if $P_a < 0.0$)

$$R_a = \frac{\varepsilon \left| P_a \right|}{\rho_a^2} \tag{4.62}$$

while a typical value of ε is 0.2. Moreover, Monaghan suggests to employ the correction also for positive values of the field pressure, due to the formation of local linear structures in case of liquids simulations. So, if $P_a > 0.0$ and $P_b > 0.0$,

$$R = 0.01 \left(\frac{P_a}{\rho_a^2} + \frac{P_b}{\rho_b^2} \right) \tag{4.63}$$

As stated before, the cubic spline kernel function with the above introduced kernel correction was employed in the SPH numerical code realized in the present work. It is to be noticed that the problem of particle clustering can be also avoided employing the kernel function proposed by Gordon R. Johnson, in an easier and straightforward way.

Density re-initialization

As it has been introduced, in the SPH model each particle has a constant mass, while density is updated by using eq. 4.27. However this evolution equation for density, doesn't ensure the consistency between mass, density and occupied area. This problem can be prevented by a periodic re-initialization of the density field, for instance smoothing out density contributions from neighbor particles, using equation 4.23. It is clear that, if the particle at hand is close to a boundary layer or to the water surface, the kernel function W suffers the lack of particles, and a corrected kernel function $\tilde{W}$ has to be considered. So, the particles' density can be re-initialized, say every ν time steps, by using the following equation:

$$\bar{\rho}_a = \sum_b m_b \tilde{W}_{ab} \tag{4.64}$$

The above introduced equation, which is very simple to implement, is usually called the 'Shepard' method (Shepard, 1968).

A different technique, which presents a first order approximation based on a Moving Least Squares (MLS) approach, was introduced by Belytschko et al. (1998) and recently applied also by Colagrossi and Landrini (2003). The periodic density correction is gained using the following expression:

$$\bar{\rho}_a = \sum_b \rho_b W_{ab}^{MLS}(\mathbf{x}_a) dV_b = \sum_b m_b W_{ab}^{MLS}(\mathbf{x}_a) \tag{4.65}$$

where the kernel function W_{ab}^{MLS} is computed by means of the following equations:

$$W_{ab}^{MLS}(\mathbf{x}_a) = \left[\beta_0(\mathbf{x}_a) + \beta_1(\mathbf{x}_a)(x_a - x_b) + \beta_2(\mathbf{x}_a)(y_a - y_b)\right] W_{ab}(\mathbf{x}_a) \tag{4.66}$$

$$\beta(\mathbf{x}_a) = \begin{pmatrix} \beta_0 \\ \beta_1 \\ \beta_2 \end{pmatrix} = \mathbf{A}^{-1}(\mathbf{x}_a) \begin{bmatrix} 1 \\ 0 \\ 0 \end{bmatrix} \tag{4.67}$$

$$\mathbf{A}(\mathbf{x}_a) = \sum_b W_b(\mathbf{x}_a) \tilde{\mathbf{A}}_{ab} \tag{4.68}$$

$$\tilde{\mathbf{A}}_{ab} = \begin{bmatrix} 1 & (x_a - x_b) & (y_a - y_b) \\ (x_a - x_b) & (x_a - x_b)^2 & (y_a - y_b)(x_a - x_b) \\ (y_a - y_b) & (y_a - y_b)(x_a - x_b) & (y_a - y_b)^2 \end{bmatrix} \tag{4.69}$$

Even if both the above introduced density correction methods slightly increase the computational time, results show a smoother density (and so, pressure) distribution. The periodic re-initialization is computed every ν time steps, without any rule suggesting a value for ν. In one of the following section details are given about the assumed value for ν.

In order to compare the above introduced density re-initialization methods a very simple test has been performed. Making reference to Figure 4.2, a given density distribution over a squared xz field was considered (top left panel), assuming ρ_0=const.=1000.0 Kgm^{-3}. Then, the considered density field was artificially disturbed by adding a small amount of density at each grid point. The disturbance was uniformly distributed in $[-0.5; +0.5]$, and the resulted density field is plotted in the top right panel of Figure 4.2. The left and the right bottom panel of Figure 4.2 show results obtained using the method A (eq. 4.64) and the method B

(eq. 4.65) respectively. It is to be noted that both methods improve the density field smoothness, reducing the disturbances around the average given value of $\rho_0 = 1000.0 Kgm^{-3}$. In order to better understand test results, the frequency distribution of the errors ε, defined as $\varepsilon = \rho(x,z) - \rho_0$, have been considered. Figure 4.3 shows the frequency of errors ε, distributed over 21 classes in the interval $[-0.5; +0.5]$. The errors distribution of the artificially disturbed density field, the re-initialization method A, and the re-initialization method B are plotted on the left, the middle and the right panel respectively. It is to be noted the narrower errors histogram of the method A, which has been preferred for density re-initialization in the SPH simulations which will be shown in the following sections. Moreover, spurious density peaks are evident along boundaries of the re-initialized density field given by method B (see Figure 4.2).

4.2.3 Computational strategies

As it is well known, SPH models suffer the great computational time employed for the neighbors particles searching. In fact, at every time step, a first *do loop* cycle is employed to consider each one of the N particles in the simulation, while a second *do loop* cycle, which works inside the former, is employed to evaluate neighbors particles contributions to the particle at hand. In order to reduce the great amount of computational time, several numerical techniques have been proposed to optimize the definition of the interacting neighbors of each particle of the fluid domain: Figure 4.4 shows the neighbors (black particles) of the particle at hand. In the followings two of the most successful SPH optimizing techniques will be introduced.

Linked list

The principal idea of linked list, or Verlet list, methods is to reduce the neighbor search algorithm by setting the particles in an ordered grid, characterized by a grid cell size equal to $2h$, as sketched in Figure 4.4. In this way, it is clear that each particle interacts at least with particles of the same grid cell, and at most with particles placed in the eight adjacent grid cells, as it is shown in the left panel of Figure 4.5. So that, a linked list algorithm consists of searching neighbors particles looking at the eight grid cells around the cell at hand: the right panel of Figure 4.5 shows one of the possible way to look at the neighbors cells. An optimization of this method is obtained by employing the action-reaction principle, according to which each interaction value A between a couple of particles i and j could be defined as $A_{ij} = -A_{ji}$, as the value of the kernel W is a function only of the distance between particles. So, the basic idea is to compute only once W_{ij} between two particles. This can be attained

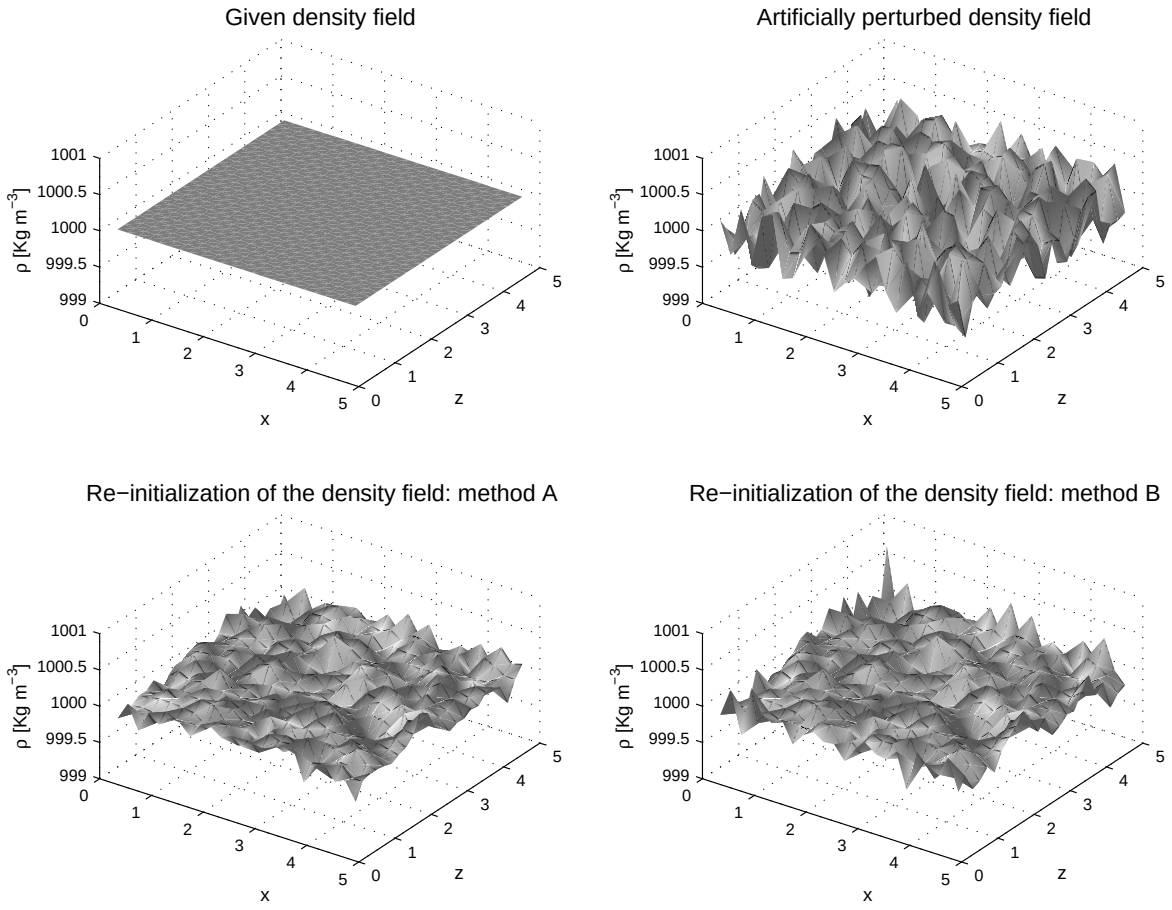

Figure 4.2: Results from the test on methods A and B for density re-initialization. Top left panel: given density field. Top right panel: artificially disturbed density field. Bottom left panel: reconstructed density field using density re-initialization method A. Bottom right panel: reconstructed density field using density re-initialization method B.

taking into account grid cells by a main direction over the grid. In this optic it is sufficient to look only at five of the grid cells of the previously defined linked list, as it is shown in Figure 4.6, while all interaction values have to be stored in dedicated vectors, with a small wasting of memory. In this example, the five neighbors cells are placed around the right upper corner of the cell at hand, so the main direction according to which grid cells have to be considered starts from the left bottom corner of the computational domain, going to the right upper corner.

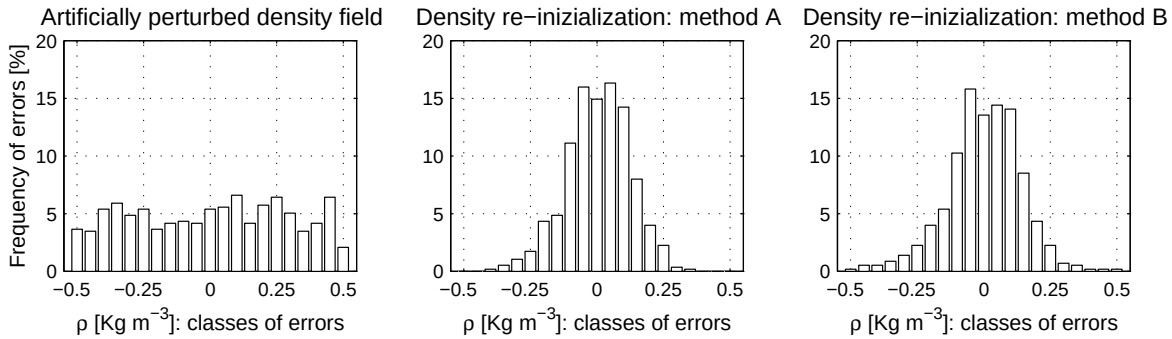

Figure 4.3: Frequency distribution of density errors ε. Left panel: histogram of errors from the artificially disturbed density field. Middle panel: histogram of errors from the reconstructed density field (method A). Middle panel: histogram of errors from the reconstructed density field (method B).

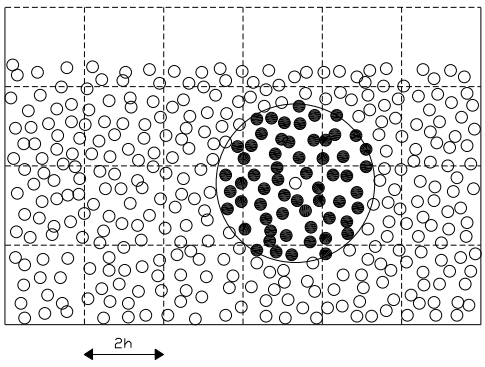

Figure 4.4: Particle interaction in the SPH model: neighbors particles of a given particle.

Oversized neighbors list

The main idea of this technique, which is introduced here for the first time, is to reduce the number of time the neighbors particles list is computed, keeping the same particle list for a certain number of time steps. The method is introduced making reference to Figure 4.7, which shows the circle (r= $2h$) of neighbors particles (blacks) of the particle at hand. By considering an oversized radius $r = 2h + \delta$ in the formation of the particle neighbors list, some non interacting particles are taken into account (grey particles). Even if unnecessary particles are considered in the list, it is possible to keep the same list for lots of numerical

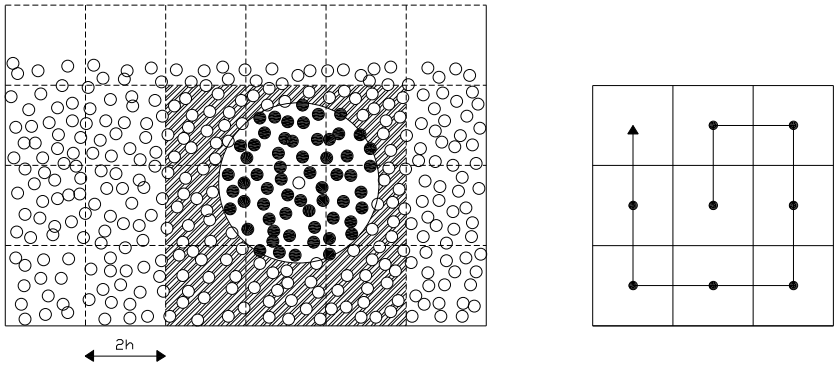

Figure 4.5: Particle grid cells in the fluid domain (on the left) and linked list through neighbors grid cells (on the right).

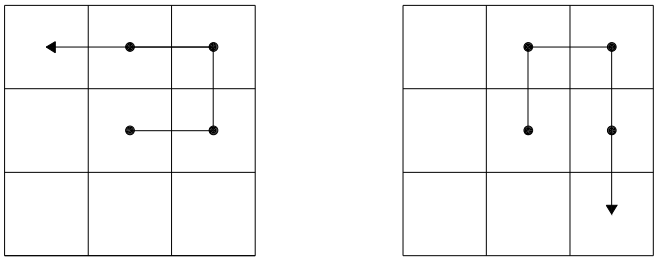

Figure 4.6: Reduced linked list algorithm over five grid cells.

time steps of the model. Considering at each time step (t_i) the maximum particle velocity ($v_i^{\max}$) in the flow field, the maximum particle movement is computed as ($ds_i^{\max} = v_i^{\max} \cdot dt$). The neighbors list is computed every time the summation of ds_i over successive time steps reaches the value of δ, that's to say:

$$ds = \sum_{i=1}^{N_{NL}} ds_i^{\max} = \sum_{i=1}^{N_{NL}} v_i^{\max} \cdot dt_i \geq \delta \tag{4.70}$$

being N_{NL} the number of time steps necessary before the neighbors list updating. Making reference to Figure 4.7, it is clear that smaller values of δ result in smaller number of the useless particles interactions enclosed in the neighbors list, but the list is frequently updated (left plot). On the contrary, greater values of δ result in greater number of useless particles enclosed in the neighbors list, but the list is infrequently updated (left plot).

In the present work, both the linked list (Verlet list) and the oversized neighbors list

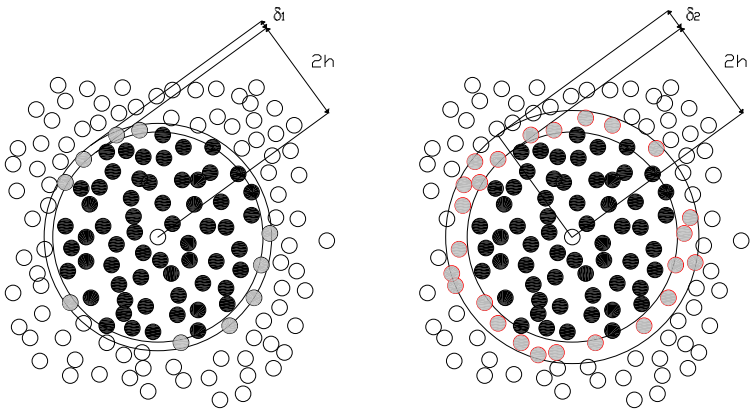

Figure 4.7: Oversized neighbors lists.

methods have been implemented and tested. The best performances have been obtained using the oversized neighbors list, which is computed every n time steps using the linked list algorithm, being n a parameter calculated as a function of the velocity of the flow field, with typical values in the range [10; 200]. It is to be stressed that, considering both the proposed method, if n=1 the optimization is reduced to the linked list method. The parameter δ was considered in the range [0.001; 0.1]: the best value to adopt is a function of the problem at hand.

Moreover, a parallel version of the original SPH algorithm has been implemented using the OpenMP parallel libraries. In particular, using both the linked list and the oversized neighbors list computational strategies made it possible to employ a technique which assigns, at any time step, the computation of variables of any given particle to the first available CPU. This can be obtained assigning a parallel do loop cycle when updating the properties of particles in the fluid domain. In particular, with this technique, the work of each CPU is equally balanced with that of other CPUs, and the parallel architecture results well optimized. The reduction of computational time using an IBM parallel machine with 8 CUPs resulted to be less than 40% the time required by a simple sequential computation.

4.2.4 Boundary Conditions

In SPH numerical codes, boundary conditions are set by external forces or pressure given by the so called boundary particles. In the SPH literature there are several numerical techniques used for the calculation of boundary particles.

Monaghan's boundary conditions

One of the most employed method to set boundary conditions in hydrodynamic simulations was introduced by Monaghan (1994). The method was conceived as an inter-molecular repulsive force. Considering a boundary and a fluid particle at the given distance r, the "Lennard Jones" force between them is defined as:

$$f(r) = D\left(\left(\frac{r_o}{r}\right)^{p_1} - \left(\frac{r_o}{r}\right)^{p_2}\right)\frac{\mathbf{r}}{r^2} \tag{4.71}$$

The considered force $f(r)$ is set to zero for $r > r_o$, and so is purely repulsive. In the same paper, Monaghan (1994) suggest to use the values $p_1 = 12$ and $p_2 = 6$ for the constants in 4.71. Moreover, while r_o is the scaling initial particle distance in the repulsive force, D is a coefficient to be set for each different problem.
In a more recent paper, Monaghan faced the problem of the irregular force distribution over a smooth plane given by the repulsive force expressed by 4.71. The new form of the repulsive force is defined as (Monaghan and Kos, 1999):

$$f(\Delta t, \Delta n) = \mathbf{n} \cdot R(\Delta n) \cdot P(\Delta t) \tag{4.72}$$

where f is the force per unit mass on a fluid particle, and it is evaluated considering two different contributions. Considering the left sketch in Figure 4.8, the former is defined as a function of the normal distance Δn of the fluid particle from the boundary at hand; the latter is defined as a function of the distance Δt between the fluid and the boundary particles, taken along the tangent. $R(\Delta n)$ is defined as:

$$R(\Delta n) = \begin{cases} A\frac{1}{\sqrt{q}}(1-q) & \Delta n < inh \\ 0 & \Delta n \geq inh \end{cases} \tag{4.73}$$

where $q = \frac{\Delta n}{inh}$, $A = \frac{1}{h}\left(0.01c_s^2 + \beta c_s \mathbf{v}_{ij} \cdot \mathbf{n}_i\right)$. On the other hand, $P(\Delta t)$ is a function set to balance the repulsive contributions from neighbor boundary particles, in order to ensure that the repulsive force presents a constant value at each point of the boundary line. The role of the P function is explained by the right sketch of Figure 4.8, and it is defined as:

$$P(\Delta t) = \begin{cases} \frac{1}{2}\left[1 + \cos\left(\frac{\pi \Delta t}{inh}\right)\right] & \Delta t < inh \\ 0 & \Delta t \geq inh \end{cases} \tag{4.74}$$

This kind of boundary conditions are easy to implement, fast in the SPH computational time, and allow to model arbitrary shaped boundaries. However, due to the constant value of the repulsive force along a boundary line, particles in proximity of a boundary are induced

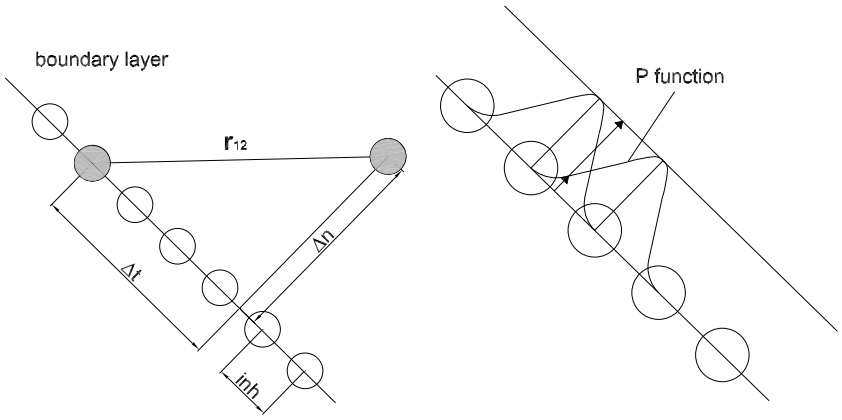

Figure 4.8: Monaghan's boundary conditions. On the left, distances between a fluid particle and a boundary particle (grey particles). On the right, repulsive contributions of two boundary particles.

to arrange along a layer parallel to the boundary at hand. Even if this side effect is unpretty to look, it doesn't introduce errors in simulations.

Dalrymple's boundary conditions

A different way to model boundaries was introduced by Dalrymple et al. (2001). The basic idea is to employ boundary particles having the same properties of the fluid particles, such as density, pressure and velocity, while maintaining a fixed boundary position. According to this method, a boundary reacts to an approaching particle by increasing the boundary particles pressure. Usually, a double layer of particles is preferred in order to ensure a smoother distribution of repulsive points along the boundary.
The main disadvantages of this boundary modelling method is the increased computational time, if it is compared to Monaghan's boundary conditions, due to the calculation of the boundary particles physical variables, and the difficulty to handle with impacts and shocks.

Ghost particles

Boundary conditions defined using ghost particles reproduce part of the computational fluid domain, which is close to the boundary at hand, symmetrically in a thin layer with dimensions of the order $O(h)$, as sketched in Figure 4.9. Ghost particles present density, pressure and velocity deduced from the fluid particles. The mirroring rules are the followings:

$$\begin{aligned} \mathbf{r}_{iG} &= 2\mathbf{r}_b - \mathbf{r}_i \\ u_{niG} &= 2u_b - u_{ni} \\ u_{tiG} &= u_{ti} \\ p_{iG} &= p_i \end{aligned} \tag{4.75}$$

where the subscript i is referred to a generic fluid particle, G is referred to the corresponding ghost particle, n and t are the normal and the tangential velocity components to the boundary, which is placed at the position $\mathbf{r}_b$. Figure 4.9 presents a simple reference sketch with a boundary wall parallel to the y axis. For arbitrary shaped boundaries, the particles mirroring has to be performed considering local normal and tangent, making particular attention to particles mass balance between outside and inside the computational domain.
As discussed in Colagrossi and Landrini (2003), equations 4.75 allow to model free slip boundary conditions. Moreover, despite the greater computational time, ghost particles allow to have a smoother particles behavior in the proximity of the modelled boundary.
Other types of ghost particles boundary condition were introduced by Takeda et al. (1994) and Morris et al. (1999).

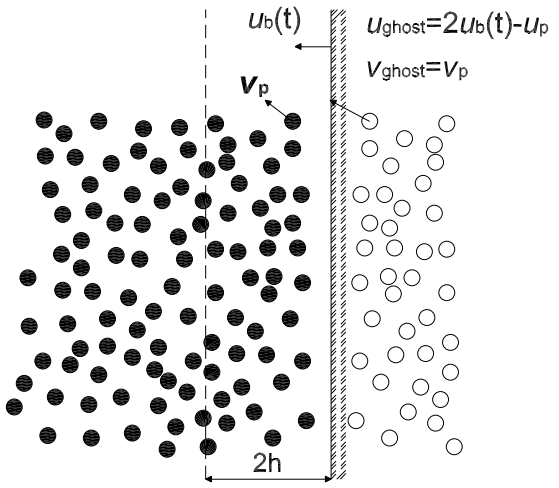

Figure 4.9: Solid boundaries with free slip conditions obtained by using ghost particles.

In the present work, all the proposed methods to model boundaries have been implemented and tested. It is to be noticed that, when considering solid-liquid interactions, such as impacts of solid bodies with the water considered in this study, the modelling of boundaries is a very delicate task. Due to the high pressures involved in this kind of problems, Dalrymple's boundary conditions sometimes fail reacting particles from solid walls. On the

other hand, as introduced before, the modelling of boundaries using ghost particles presents the side effect of a greater computational time. So, due to the possibility to model arbitrary shaped boundaries in a straightforward way, due to the reduced computational time, and above all due to the possibility to successfully deal with impacts between solid bodies and the water, in the present work the repulsive Monaghan's boundary conditions have been adopted.

4.2.5 Model tests

A series of tests have been performed in order to assess and verify the implemented SPH model. Comparisons with other SPH models found in the literature are introduced and discussed in the present section, with the aim of individuating possible source of inaccuracy or weak aspects of the numerical model, along with correctly reproduced test conditions.
Subsequently, the implemented numerical model is applied to physical experiment reproducing landslide generated waves in a two dimensional water body.

Dam break test proposed by Martin and Moyce (1952)

One of the most common test used to validate free surface numerical codes is the dam break problem. Making reference to top left panel of Figure 4.10, a column of water is initially at rest, sustained by rigid walls. The dam break flow field is triggered by removing the right wall which sustain the water column. In the physical experiment presented by Martin and Moyce (1952), the water column is two units high and one unit wide. Here, a comparison with the experimental results obtained by Martin and Moyce (1952) is carried out. Physical parameters are made dimensionless by referring to the column width a as length scaling parameter. So, the dimensionless time is $t^* = t\sqrt{g/a}$, being $g = 9.81$ the gravitation acceleration. The computational domain is $4a$ long and $3a$ high. The water flow takes place on a dry bed with free slip conditions. Left panels of Figure 4.10 show experimental test results at the dimensionless times $t^* = [0.023; 0.900; 1.847; 2.678; 3.487]$.
Right panels of Figure 4.10 show results from the SPH numerical simulation of the proposed dam break test, at the same values of the dimensionless time. The numerical test has been performed using 7200 particles, and assuming a=6.0 m, a particle size equal to $0.0167a$ (0.1 m), a $XSPH$ smoothing parameter $\varepsilon_{XSPH} = 0.05$, and a viscosity parameter $\alpha = 0.1$.
Results show a very good agreement between the SPH simulation and the experiment performed by Martin and Moyce (1952). In particular, it is evident the SPH capability in correctly reproducing the shape of the free surface, while the simulated flow field is perfectly synchronized with the experimental frames. This aspect is also appreciable by considering

Figure 4.11, which presents the toe positions time movements, calculated by the SPH model (continuous line) and taken from Martin and Moyce (1952) experimental results (black dots).

Free surface test proposed by Gallati and Braschi (2000)

In his work Gallati and Braschi (2000) presented a physical experiment of a dam break generated flow field, which, after accelerating on a dry bed, hits against a fixed obstacle. The top left picture of Figure 4.12 shows the initial stage of the experiment performed by Gallati. In the same work a comparison with the SPH model is presented, demonstrating a very satisfactorily model capability in reproducing the complexity of the proposed case study. The free surface modelling and the characterization of the impact between water and structure are very difficult tasks in the considered physical experiment. In the present work, the experiment performed by Gallati has been taken as a reference test to validate the implemented SPH numerical code.

The performed experiment can be easily described referring to pictures in the left column of Figures 4.12 and 4.13, which shows subsequent frames taken from the performed experiment (pictures taken by Gallati and Braschi, 2000). A dam break water flow field is generated removing the wall sustaining a water column, which initially is 0.225 m wide and 0.1 m high. A fixed obstacle, 0.06 m wide and 0.03 m high, is set at a distance of 0.395 m from the left wall of the computational domain. After being released to move, the the toe of the dam break accelerates and eventually hits the rigid squared obstacle, thus producing a violent impact. Part of the water is reflected back, and part of the water overtops the obstacle forming a jet. Then, the water eventually hits the right wall of the computational box domain, and a roller takes place.

Figures 4.12 and 4.13 present the comparison between frames taken from the experiment performed by Gallati and Braschi (2000), on the left column, and the SPH simulation performed in the present work, on the right column, at the same values of time, equal to [0.13; 0.21; 0.31; 0.52; 0.73; 0.86] s. The SPH simulation was performed using 5600 fluid particles and 882 fixed boundary particles, with a particles diameter equal to 0.002 m. It was also assumed a viscosity coefficient $\alpha = 0.05$, the smoothing $XSPH$ coefficient $\varepsilon_{XSPH} = 0.1$, and $B = 10000\rho/\gamma$.

Results show a very surprisingly agreement between physical experiment and SPH numerical simulations. Jetties and splashes are fully characterized, and also the mean flow is correctly represented. Figure 4.14 presents a detail of the water impact against the obstacle along with the vector velocity field, both simulated using the SPH numerical code, at the time t=0.21 s, t=0.31 s, t=0.52 s.

4.2.6 Model applications

Scott Russell wave generator: release from below the water level

After the testing of the implemented SPH numerical code, numerical simulations reproducing the two dimensional physical experiment presented in this work were carried out. The first case taken into consideration was the "Scott Russell wave generator" with a box released from below the water level. The considered physical test was performed assuming a water depth d=0.10 m, a box width λ=0.10 m, a release height $\xi = d_1 - d$=-0.03 m.
Figure 4.15 shows the comparison between the physical experiment (left column) and the performed SPH numerical simulation (right column). Couples of frames on the horizontal are taken at the same time. The SPH simulation was carried out using 3880 fluid particles, 320 boundary particles, 58 box particles, with a particle size equal to 0.005 m (particle diameter). The falling box was modelled as a rigid body, which movements are calculated considering the vertical balance of gravity and water pressure forces. Water pressure exerted on the bottom of the box was calculated considering the fluid particles pressures, by using the SPH summation. Pictures reported in Figure 4.15 show a part, 0.4 m on the x axes and 0.3 m on the y axes, of the used computational domain, which was equal to 1.0 m on the x axes, and 0.3 m on y axes. SPH model parameters assumed values $\alpha = 0.05$, $\varepsilon_{XSPH} = 0.1$, $B = 5000\rho/\gamma$.
The agreement between the numerical model and the physical test is very satisfactorily. In particular, the numerical model performs very good the box movements with time, demonstrating a correct water pressure which dynamically adjusts the of vertical forces on the box.

Scott Russell wave generator: release from above the water level, case 1

The second considered application case was the "Scott Russell wave generator" with a box released from above the water level, assuming a water depth d=0.10 m, a box width λ=0.10 m, a release height $\xi = d_1 - d$=+0.03 m.
The Figure 4.16 presents the comparison between the physical experiment (left column) and the performed SPH numerical simulation (right column), at the same instant of time. The SPH simulation was carried out using 20000 fluid particles, 802 boundary particles, 148 box particles. The falling box was modelled as a rigid body, which movement is given by the vertical balance of gravity and water pressure forces. Water pressure exerted on the bottom

of the box was calculated over the fluid particles pressures, by using the SPH summation interpolation. Pictures reported in Figure 4.15 show a part, which is 0.36 m on the x axes and 0.3 m on the y axes, of the used computational domain, which was equal to 0.8 m on the x axes, and 0.3 m on y axes. In this simulation the kernel proposed by Johnson et al. (1996) was employed. SPH particles had a diameter equal to 0.002 m, and the same value was assumed for the initial particle spacing. Other model parameters assumed values $\alpha = 0.07$, $\varepsilon_{XSPH} = 0.1$, $B = 2500\rho/\gamma$. Boundaries were modelled employing Monaghan's repulsive boundary conditions, which consist of fixed particles repulsing fluid particle by means of forces defined in equations 4.72, 4.73 and 4.74. Another coefficient, equal to 0.01, multiplied the repulsive force in order to smooth the boundaries repulsive contributions.
Surface water level calculated by the SPH numerical model show a satisfactorily agreement with the performed physical test. The maximum height of the produced splash is well modelled by SPH, such as the box movements with time, demonstrating a correct water pressure which dynamically adjusts the balance of vertical forces on the box. As the box starts entering the water, an air cavity is formed between the box vertical wall and the water, which, being impulsively pushed in motion, forms a sharp cavity surface. The SPH model seems to correctly reproduce the water behavior in the initial stage of the impulse wave generation, presenting a shape of the cavity which is satisfactorily the same as that one of the performed physical experiment. It is to be noted that, for practical reasons, thin separations were kept between the box walls and the wave flume walls, which were of the order of 1/10 of a millimeter on each one of the three box walls. This could be the reason why the SPH simulation presents a water cavity slightly larger than the physical model does. Figure 4.17 reports a detail of the water surface and the vector velocity field, both simulated using the SPH numerical code, at the time t=0.12 s and t=0.20 s.

Scott Russell wave generator: release from above the water level, case 2

A test to that one proposed in the previous section is here presented, considering a water depth d=0.18 m. The box of the "Scott Russell wave generator" is released from above the water surface, considering $\xi = d_1 - d$=+0.03 m.
Figures 4.18 and 4.19 present obtained results, showing the comparison between the physical experiment (left column) and the performed SPH numerical simulation (right column), at the same instant of time. The SPH simulation was carried out using 27000 fluid particles, 702 boundary particles, 148 particles modelling the falling box. As in the previously presented simulation, the falling box was modelled as a rigid body, which movement is given by the vertical balance of gravity and water pressure forces. Water pressure exerted on the bottom

of the box was calculated over the fluid particles pressures, by using the SPH summation interpolation. Pictures reported in Figures 4.18 and 4.19 show a part, which is 0.4 m on the x axes and 0.3 m on the y axes, of the used computational domain, which was equal to 0.6 m on the x axes, and 0.3 m on y axes. The same SPH model parameters employed in the last presented simulation were considered (Johnson et al. (1996) kernel function, particles diameter equal to 0.002 m, $\alpha = 0.07$, $\varepsilon_{XSPH} = 0.1$, $B = 2500\rho/\gamma$, Monaghan's repulsive boundary conditions).

Also this application demonstrates that surface water level calculated by the SPH numerical model shows a satisfactorily agreement with the performed physical test.

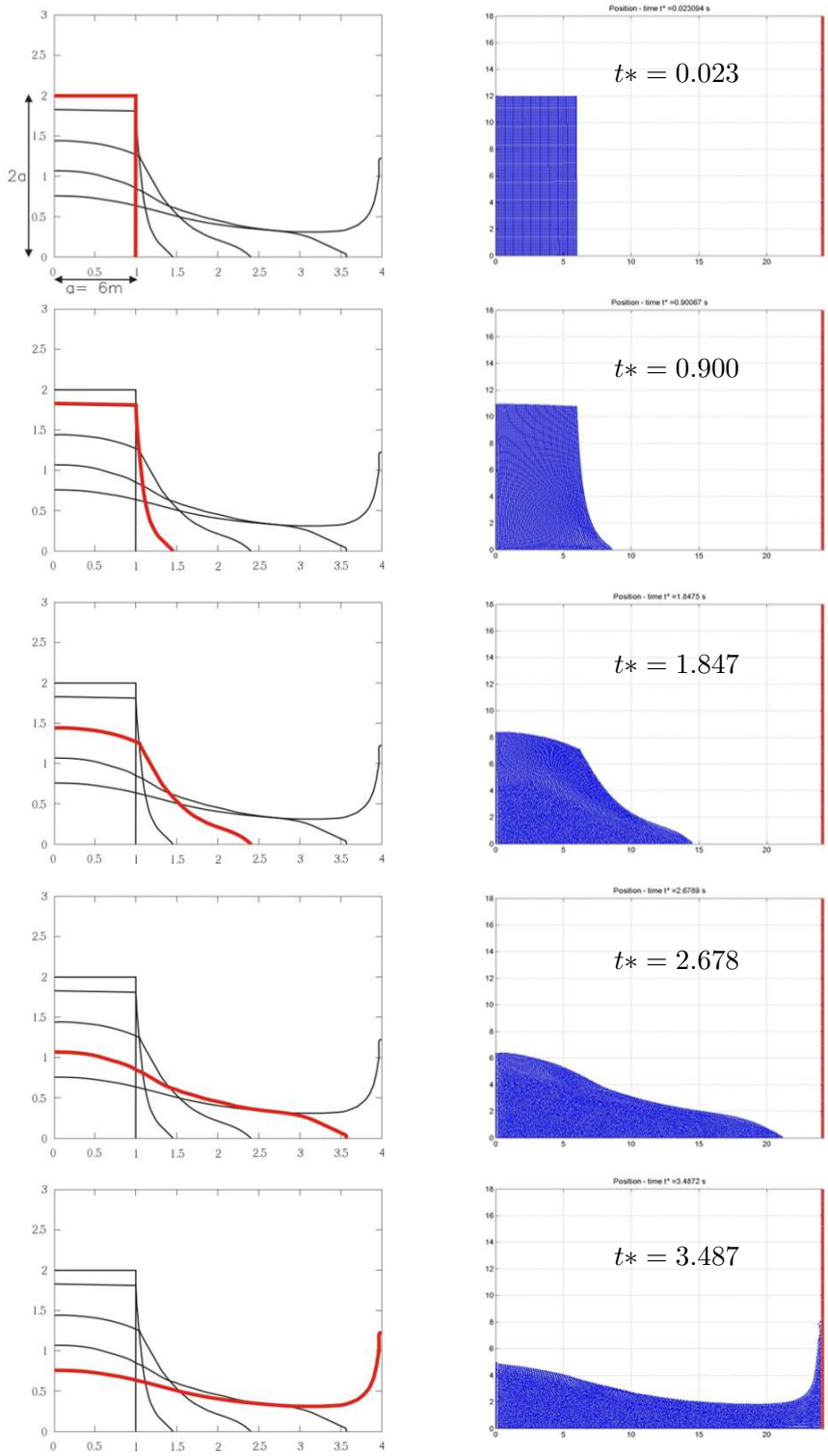

Figure 4.10: Frames of the comparison between physical model test (on the left) and SPH simulation (on the rigth) of the dam break test proposed by Martin and Moyce (1952).

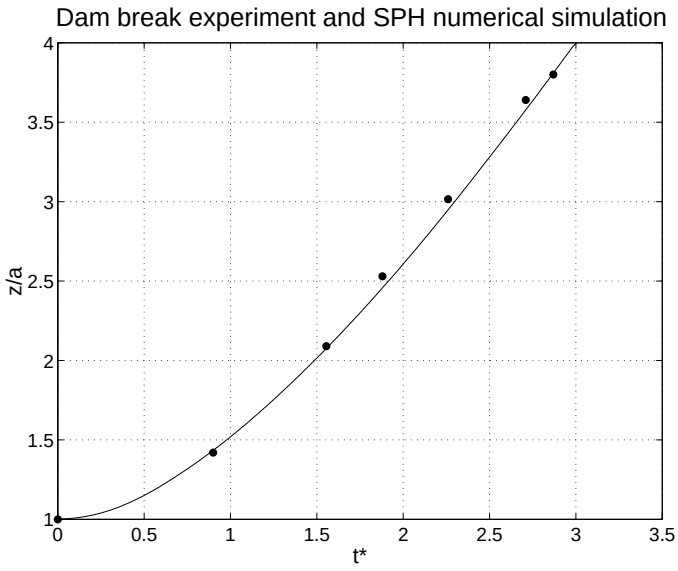

Figure 4.11: Dam break toe time movements. Comparison between calculated (continuous line), and experimental (black dots) toe position of the dam break problem proposed by Martin and Moyce (1952).

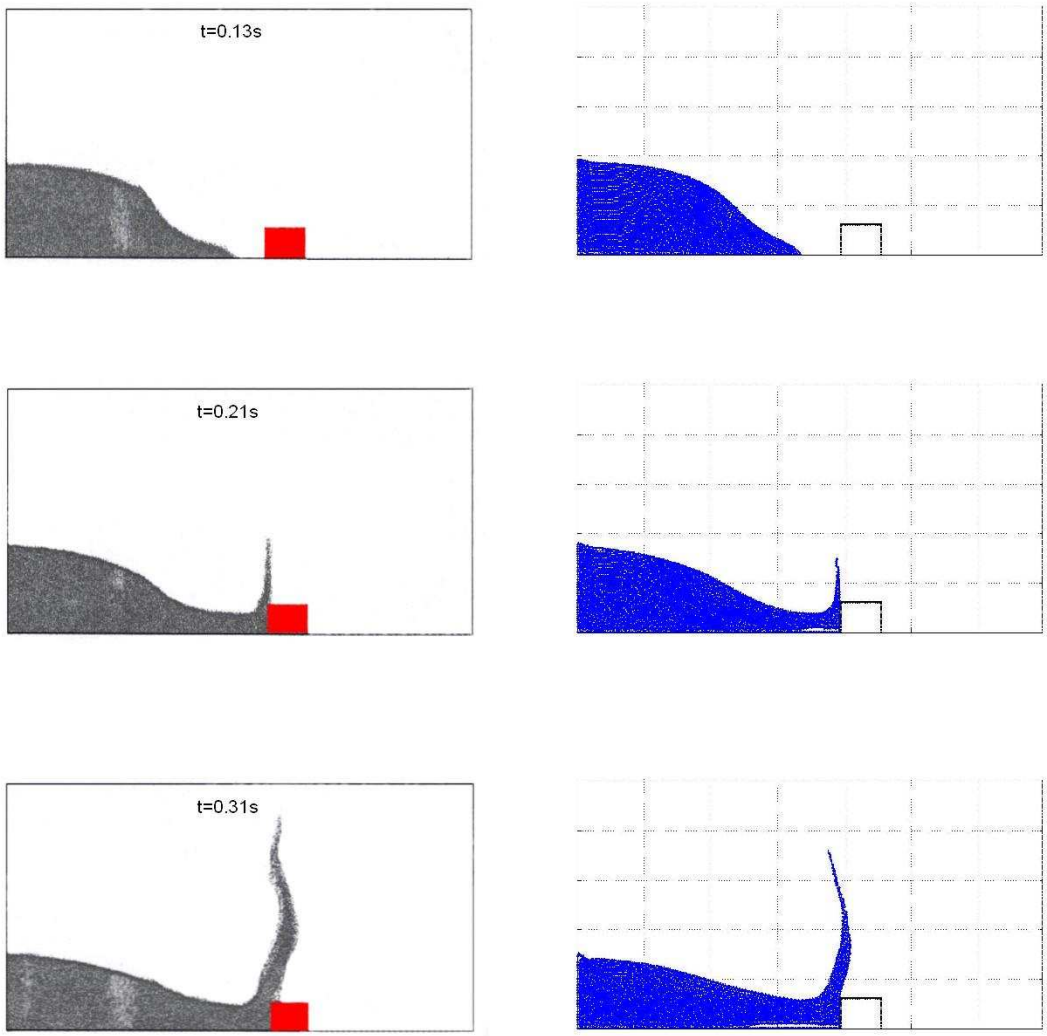

Figure 4.12: Free surface test proposed by Gallati and Braschi (2000). Comparison between physical experiment (left column) and SPH numerical simulation (right column). First row, t=0.13 s; second row, t=0.21 s; third row, t=0.31 s.

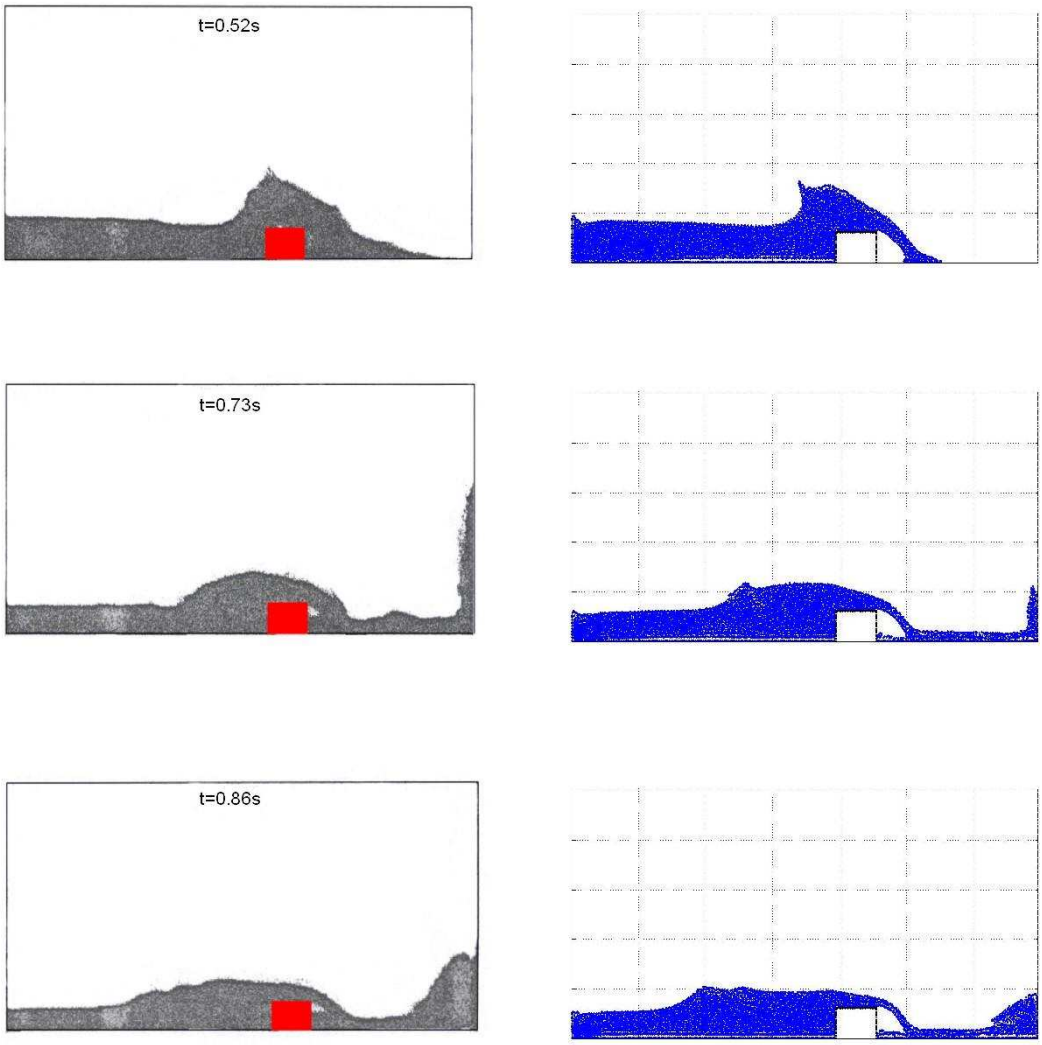

Figure 4.13: Free surface test proposed by Gallati and Braschi (2000). Comparison between physical experiment (left column) and SPH numerical simulation (right column). First row, t=0.62 s; second row, t=0.73 s; third row, t=0.86 s.

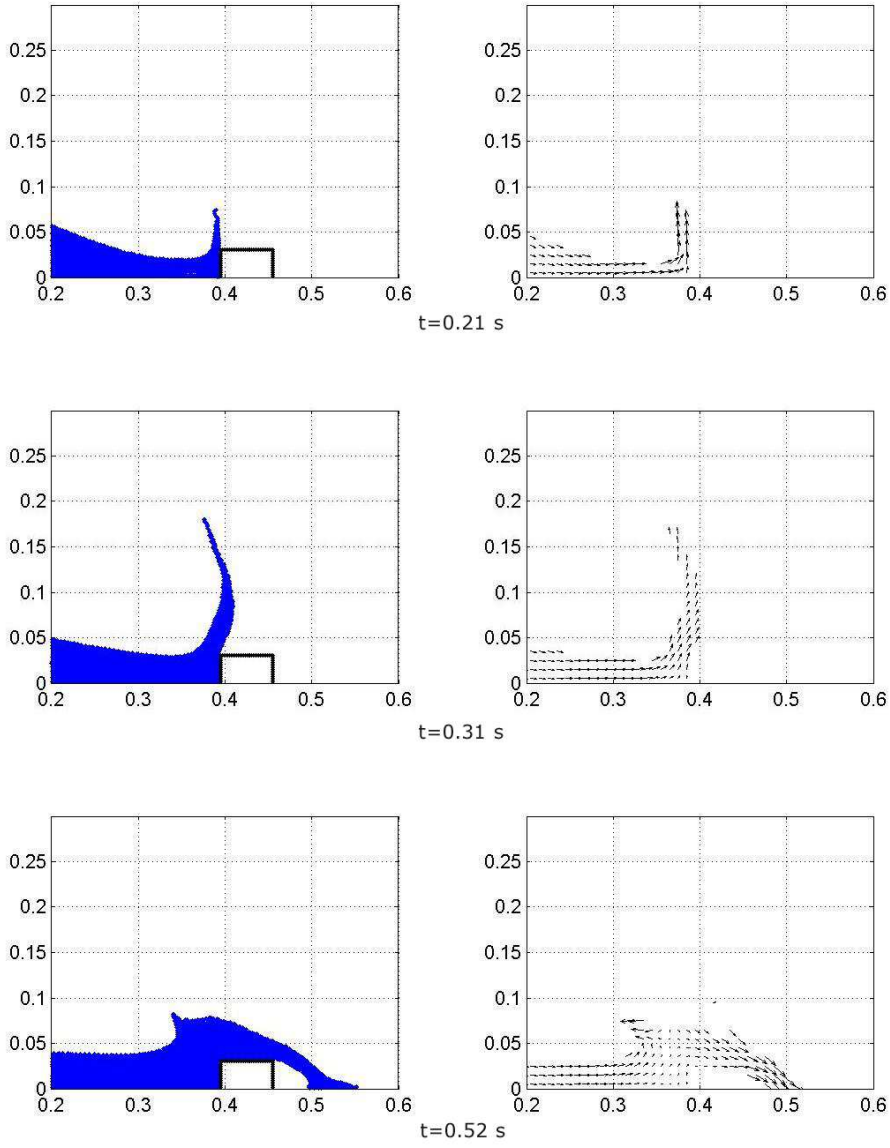

Figure 4.14: Free surface test proposed by Gallati and Braschi (2000). Details of the calculated free surface flow field (left column) and vector velocity field (right column) at three different time (0.21 s; 0.31 s; 0.52 s).

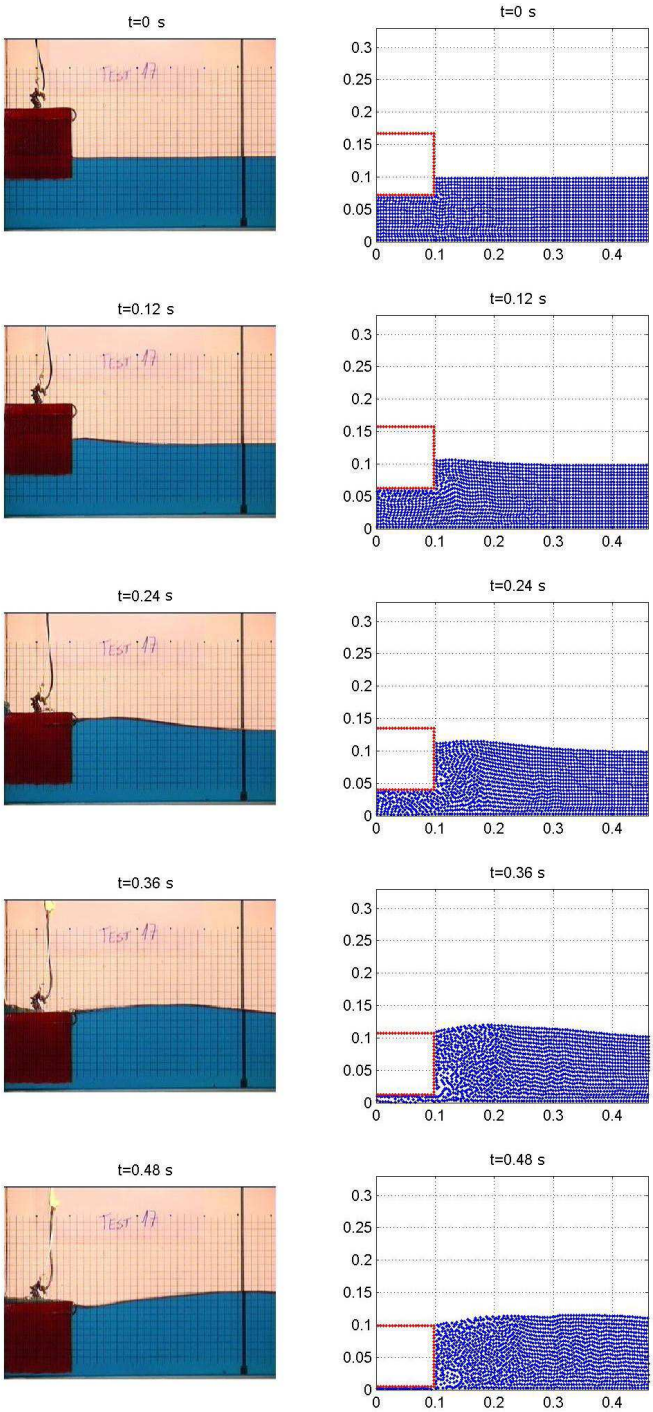

Figure 4.15: Comparison between experimental frames and SPH simulation of the "Scott Russell" wave generator. The test was performed considering d=0.10 m, λ=0.10 m, $\xi = d_1 - d$=-0.03 m.

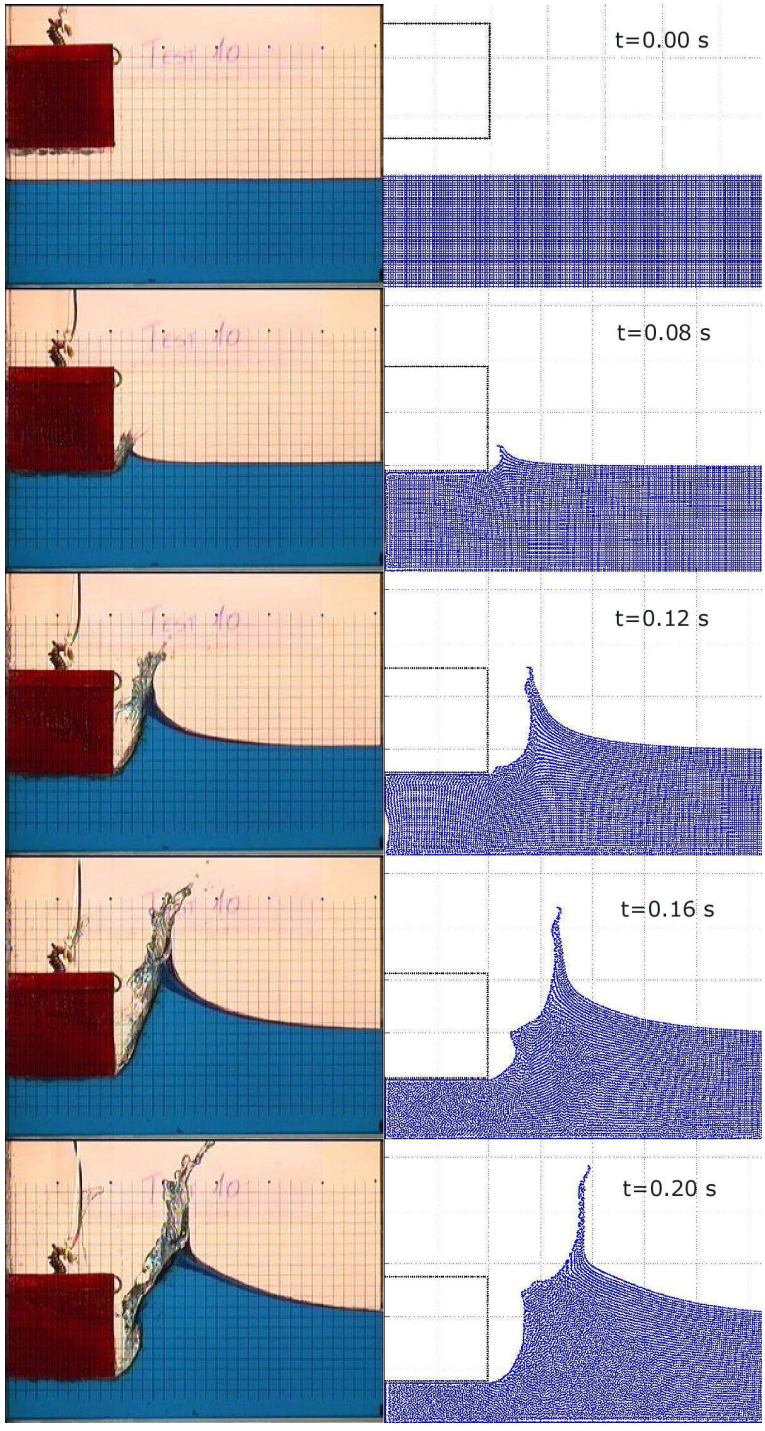

Figure 4.16: Comparison between experimental frames and SPH simulation of the "Scott Russell" wave generator. The time is expressed in seconds.

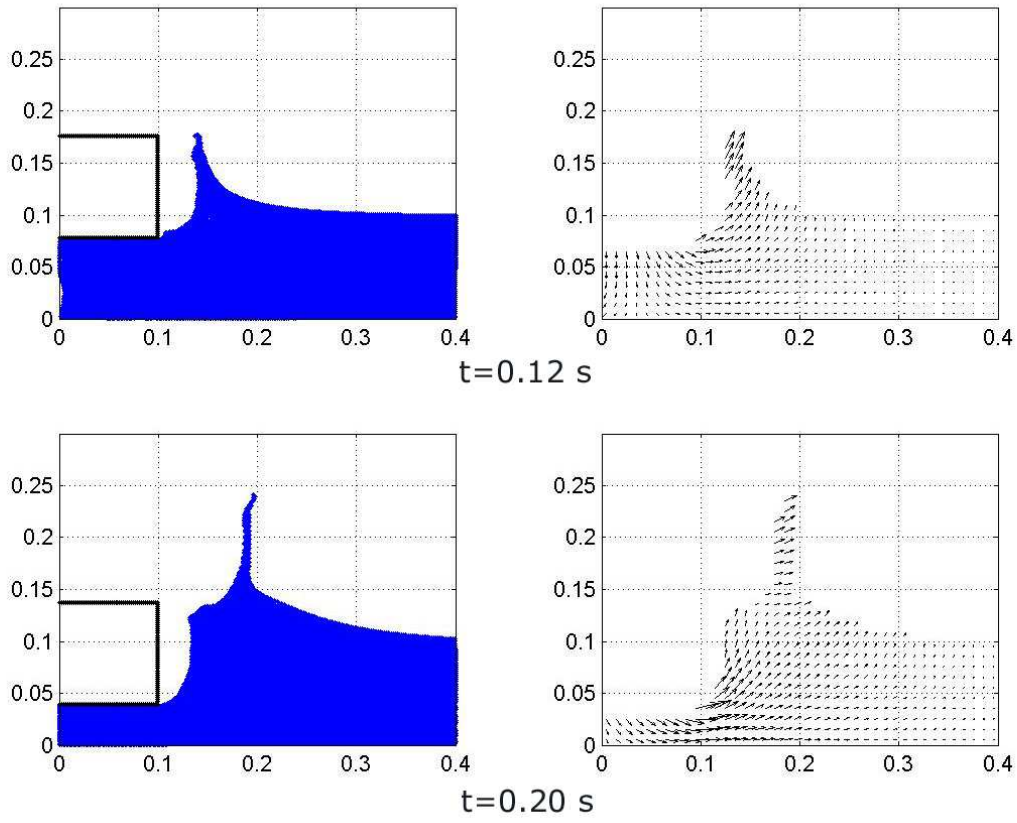

Figure 4.17: SPH simulation of the "Scott Russell" wave generator, release from above the water surface. Details of the water surface and the vector velocity field, taken at t=0.12 s and t=0.20 s.

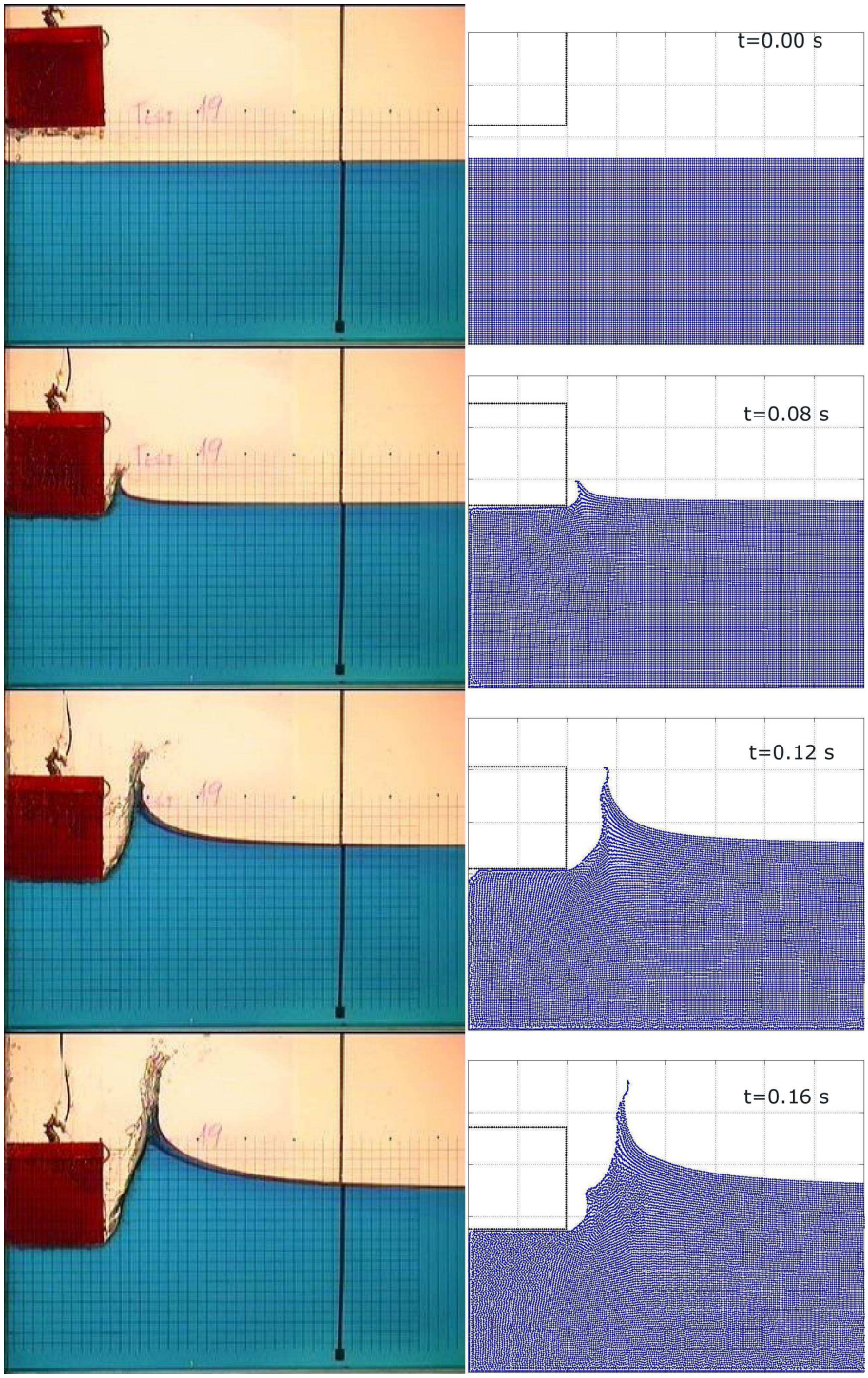

Figure 4.18: Comparison between experimental frames and SPH simulation of the "Scott Russell" wave generator. Release from above the water surface.

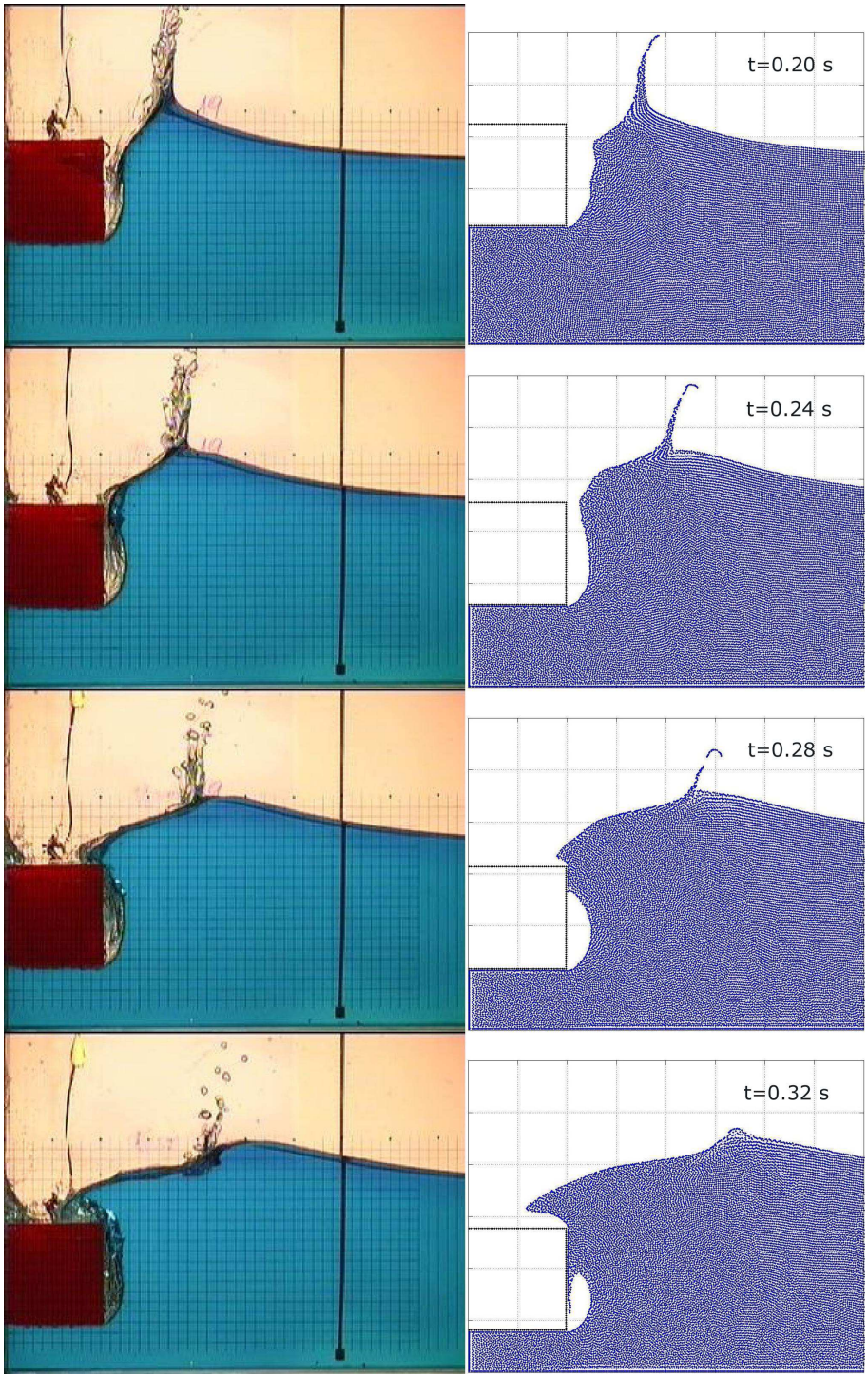

Figure 4.19: Comparison between experimental frames and SPH simulation of the "Scott Russell" wave generator. Release from above the water surface.

Chapter 5

Case studies

5.1 Introduction

This section presents some very famous past events with the aim both to shed light to some different aspects of the considered phenomenon and to characterize the principal features of the generated water wave field using the previously introduced experimental formulations. In particular, subaerial landslide generated waves events occurred in Italy around the 1960 are considered, including the well known and tragic event occurred at the Vajont valley on October the 9^{th} 1963, where the generated impulse wave caused 2000 deaths.

5.2 1959 event at Pontesei, Italy

On March the 22^{nd} 1959, at the Pontesei artificial basin, an impulse wave was generated by the falling of a 5 million m^3 landslide into the water. A man, who was walking along the street on the opposite side of the basin, was killed by the runup of the generated impulse wave. The event is described in the work of Semenza (2002). Figure 5.1 sketches the dam location, while Figure 5.2 shows a picture of the dam and the artificial reservoir as it appears today.

The 1959 event didn't cause damages to the dam, but reduced the basin capacity of about the 50%. The dam is 93 m high, the basin capacity was equal to $9.09 * 10^6$ m^3 before the 1959 landslide, while now it is equal to $5.8 * 10^6$ m^3. On March the 22^{nd} 1959 the basin contained about 6.10 million m^3 of water. As sketched in Figure 5.3, the landslide was made up mainly of limestone and dolomite. Considering the descriptions in the works of Semenza

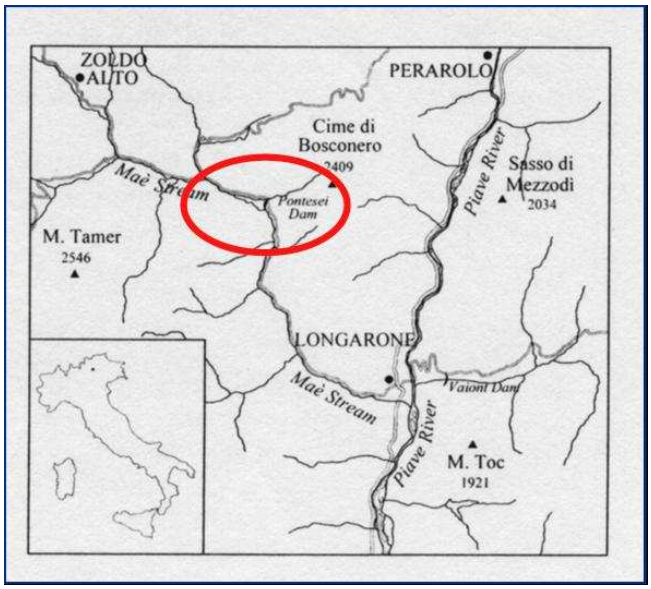

Figure 5.1: Map of the Pontesei dam location in Italy (Caratto et al., 2002).

Figure 5.2: Picture of the Pontesei dam and artificial reservoir as it appears today. The 1959 landslide is clearly visible on the right-hand side of the lake.

(2002) and Caratto et al. (2002), it is possible to make reasonable assumptions about the values of principal parameters involved in the phenomenon. The slope inclination angle of the landslide, as it can be estimated analyzing Figure 5.3, was considered to be variable in

the range [5; 10] °. As sketched in Figure 10, page 37, of the work of Semenza (2002) (see Figure 5.4), the landslide front width w was equal to 400 m, while the landslide front height, considering Figure 5.3, was equal to 50 m. About this parameter, the landslide sliding bed was defined by means of soil drillings carried out by ENEL (the national society for electricity supply in Italy) in 1969, as reported by Milli (1975). The impact velocity can be calculated considering that the landslide felt down into water in about 2-3 minutes, covering a distance equal to 120 m: so that the impact velocity v is taken in the range [0.7; 1.0] m/s (the movement can be classified as very rapid according to Cruden and Varnes, 1996). As the water level, at the moment the landslide felt down into the water, was equal to 787 m above the m.s.l., while the bottom of the reservoir was at 740 m above the m.s.l., the value of the water depth d can be assumed equal to 47 m. The application of the formulation forecasting the maximum wave height is here applied considering θ=0.0 °, as it is known for sure that the generated impulse wave reached the street which was on the opposite side of the basin (see Figure 5.4). The distance from the impact point is taken equal to 190.0 m.
As far as the maximum wave height is concerned, the work of Semenza (2002) reports a value of about 20.0 m on the opposite side of the basin, without considering wave runup.
Considering the values of the principal physical parameters involved in the phenomenon, Figure 5.5 shows results obtained applying the forecasting formulation defined in Chapter 3. Results are plotted considering a given uncertainty on the landslide impact velocity, assumed to vary in the range [0.7; 1.0] m/s, and the slope inclination angle, variable in the range [5; 10] °. It can be noticed that the maximum generated wave height varies the range [16.0 m; 18.0 m], which is in perfect agreement with the value reported in the work of Semenza (2002).

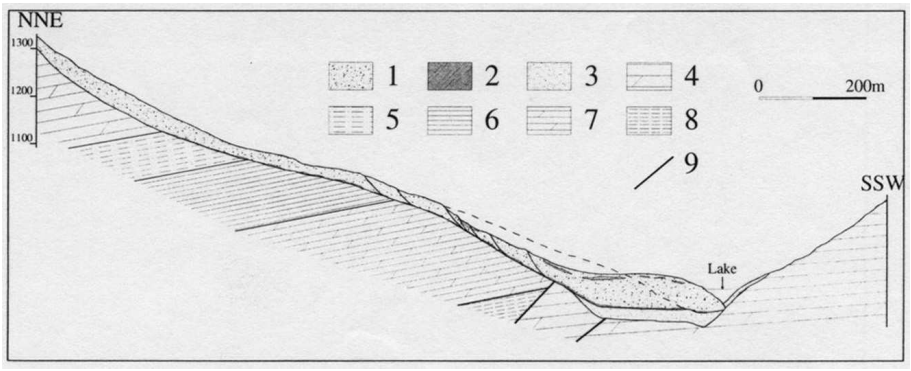

Figure 5.3: Geologic profile of the 1959 landslide felt into the Pontesei artificial reservoir. 1) Slope debris; 2) Clayey deposit; 3) Alluvial deposit; 4) Noric; 5) Upper Carnic; 6) Carnic; 7) Carnic; 8) Upper Ladinic; 9) Fault (Caratto et al., 2002).

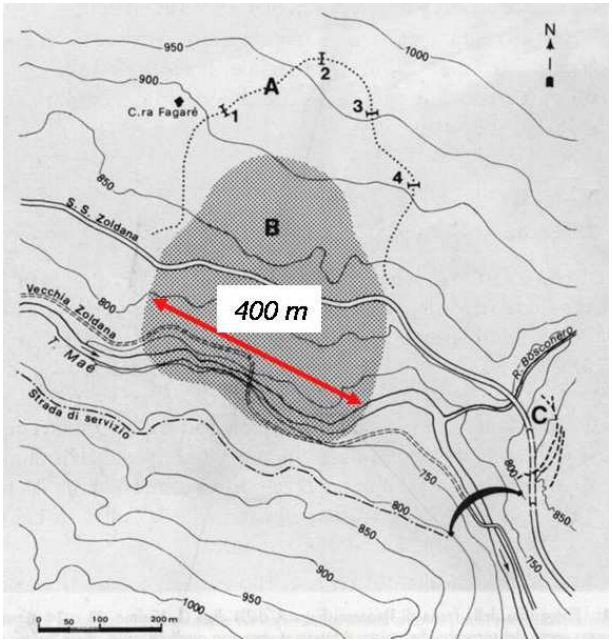

Figure 5.4: Estimate of the landslide width of the landslide occurred on the March 22, 1959, at the Pontesei reservoir (Semenza, 2002).

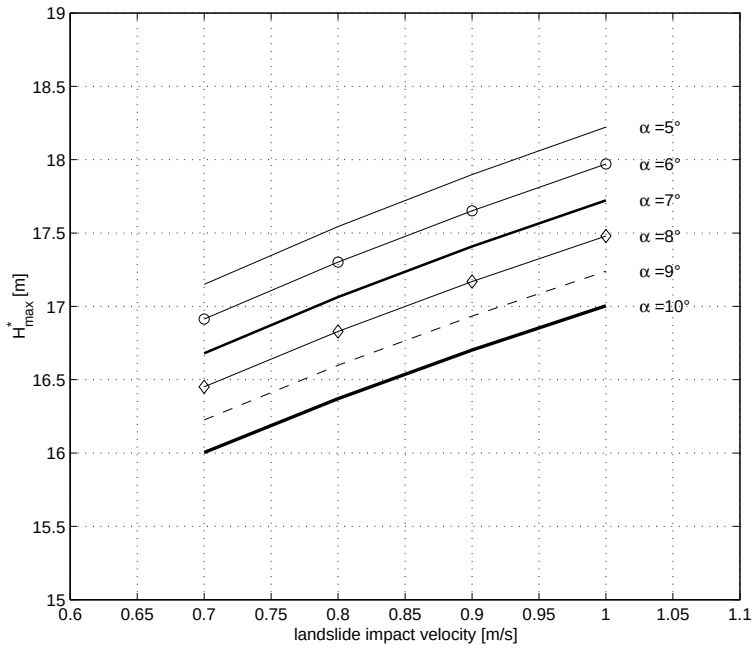

Figure 5.5: Estimated maximum wave height generated during the event of the March 22, 1959, at the Pontesei reservoir.

5.3 1960 and 1963 events at the Vajont reservoir, Italy

The realization of the artificial reservoir in the Vajont valley triggered two landslides which felt into the water on November 4, 1960 and on October 9, 1963. In particular, the latter is one of the worst documented event of subaerial landslide generated waves, which caused more than 2000 deaths.

The first event occurred at the Vajont reservoir during the first year of the filling up of the artificial basin. On November 4, 1960 a rock landslide, with a volume equal to 700.000 m^3, felt into water causing an impulse water wave which was 2.0 m high and caused a wave runup on the dam equal to 10 m (Semenza, 2002). At that moment, the reservoir surface was at 652.00 m over the m.s.l. (mean water depth equal to 160 m), and contained 40.000.000 m^3 of water. Figure 5.6 reports the time series of the water level of the Vajont artificial reservoir (the picture is taken from Selli and Trevisan, 1964). Figure 5.7 shows a map of the Vajont reservoir, reporting the shape and dimensions of the landslides occurred on November 4, 1960 and on October 9, 1963. Concerning the 1960 event, the analysis of the map indicates a landslide width equal to 250 m. Moreover, Figure 5.8 shows that the landslide height h was equal to 10 m, while the slope inclination angle α can be considered variable in the range [30°; 35 °]. Then, according to the work of Semenza (2002), the landslide movement was very fast, and the impact velocity can be assumed variable in the range [5 m/s; 10 m/s]. The value of the observed maximum wave height reported in the work of Semenza (2002), equal to 2.0 m, is to be intended close to the dam: for this reason, the experimental formulation defined in Chapter 3 has been applied considering $\theta = 90°$ and a distance from the impact point $r = 480.0$ m. These values have been defined analyzing the map of the Vajont valley reported in Figure 5.7. Obtained results of the forecasted value of H_{max} are plotted considering a given uncertainty on the landslide impact velocity, assumed to vary in the range [5.0; 10.0] m/s, and the slope inclination angle, variable in the range [30; 35] °. It can be noticed that the maximum generated wave height is estimated to be satisfactorily close to that reported by Semenza (2002).

The event occurred the 9th October, 1963 is one of the most dangerous ever documented phenomenon of subaerial landslide generated waves. A 300 million m^3 landslide felt into the Vajont artificial reservoir, which had been filled up during the previous years (see Figure 5.6). The landslide movement was not a sudden surprise, but was an ancient slow mechanism, which was accelerated by the filling up of the artificial basin. In the years preceding the disaster,

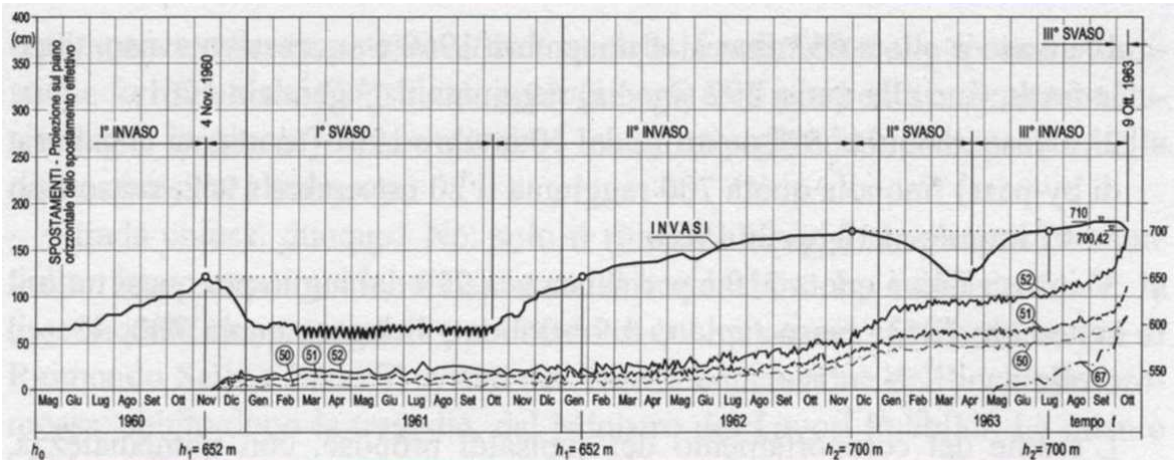

Figure 5.6: Time series of the water level of the Vajont artificial reservoir, plotted using a continuous line with label "invasi", and the 1963 landslide event movements, plotted using a continuous line with label "52", over a time window of 4 years (figure taken from Selli and Trevisan, 1964).

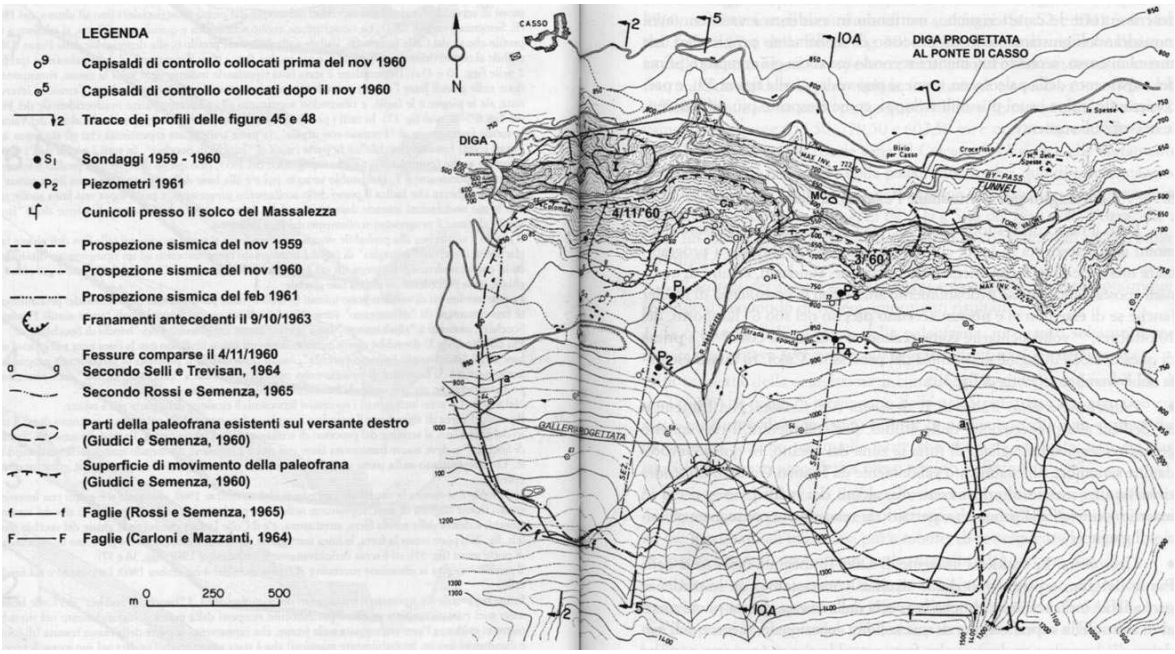

Figure 5.7: Map of the Vajont reservoir showing the shape of the landslides occurred on November 4, 1960 and on October 9, 1963 (figure taken from Semenza, 2002).

some geologists studied the landslide and realized that it was a giant M-shaped mechanism (see Figures 5.7 and 5.10). The 9th October, 1963 the basin surface was at 700.0 m over

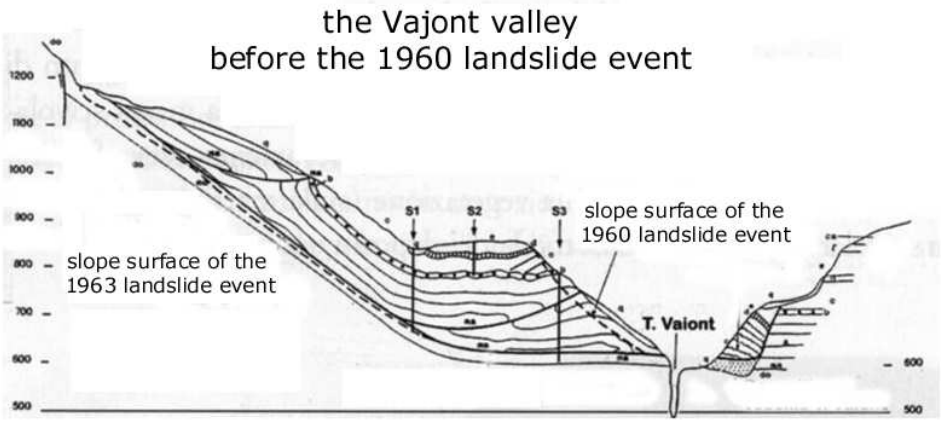

Figure 5.8: Geological section reporting the 1960 and 1963 landslide events occurred at the Vajont valley (figure taken from Semenza, 2002).

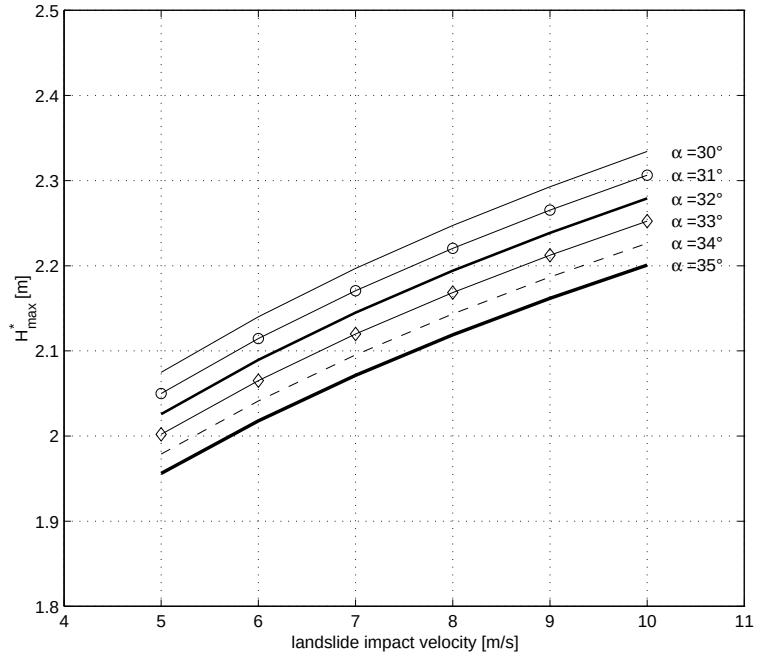

Figure 5.9: Estimated maximum wave height H_{max} generated during the event of the November 4, 1960 occurred at the Vajont reservoir.

the m.s.l., corresponding to a mean water depth equal to 200.0 m, and contained about 120 millions m^3 of water. The landslide generated a high impulse wave which runupped the opposite slope, reaching the height of 235 m above the basin water surface, and subsequently

propagated upstream the Vajont valley, and downstream, overtopping the dam and then destroying the city of Longarone. Figure 5.11 presents a picture of the Vajont valley just after the October 9, 1963 landslide. While the Vajont disaster is still frequently discussed trying to understand what happened and who were people responsible of so many deaths, in the present work the experimental formulation to forecast the maximum wave height generated by a landslide falling into water is applied using physical parameters of the 1963 Vajont event. It is to be stressed that the considered event presented values of physical parameters which are outside the ranges experimented in the present work on physical models. However, the application of the forecasting experimental formulation defined in Chapter 3 can still provide useful and reliable information about the generated impulse wave.

It is well known that the landslide mechanism was 2000 m wide, as it can be deduced by analyzing Figure 5.7. This value is also confirmed by Datei (2003). As far as the landslide height is concerned, a reasonable assumption is to consider a value of 140.0 m, as it can be deduced by analyzing Figure 5.8. The seismic waves time series recorded at the Pieve di Cadore measuring station demonstrates that the landslide mechanism took about 20.0–25.0 s to fall into the water (see Figure 5.12). Assuming this hypothesis, the landslide impact velocity can be taken in the range [20.0; 25.0] m/s, as proposed also by Datei (2003). Then, Figure 5.8 shows a low slope inclination angle close to the water, while it increases upstream. So, the value of the slope inclination angle can be taken in the range [6.0°; 10.0°]. Finally, Semenza (2002) reports a value of the maximum generated wave equal to 210.0 m in correspondence of the dam, which can be assumed to be at θ=0.0 ° and at a distance r=130.0 m from the impact point. With these assumptions, the application of the forecasting formulation gives the estimates of H_{max} reported in Figure 5.13. It can be deduced that, even if the considered values are pretty outside the experimented ranges, reasonable assumptions give consistence to H_{max} estimates, which are in a very satisfactorily agreement with the value of 210.0 m reported by Semenza (2002).

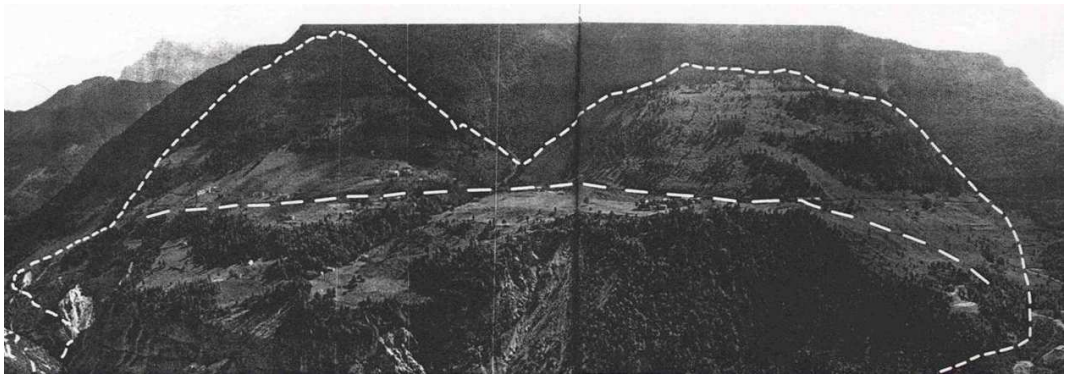

Figure 5.10: Picture of the Toc mountain, taken by E. Semenza in 1959, reporting the first hypothesis about dimensions and shape of the landslide mechanism interesting the Vajont reservoir (picture taken from Semenza, 2002).

Figure 5.11: The Vajont valley just after the October 9, 1963, landslide event.

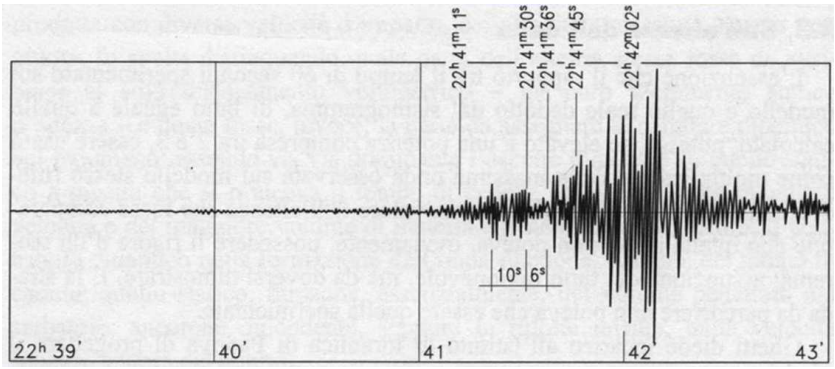

Figure 5.12: Seismic wave record from the Pieve di Cadore measuring station showing the time the 1963 landslide mechanism took to fall into water, equal to 20.0–25.0 s.

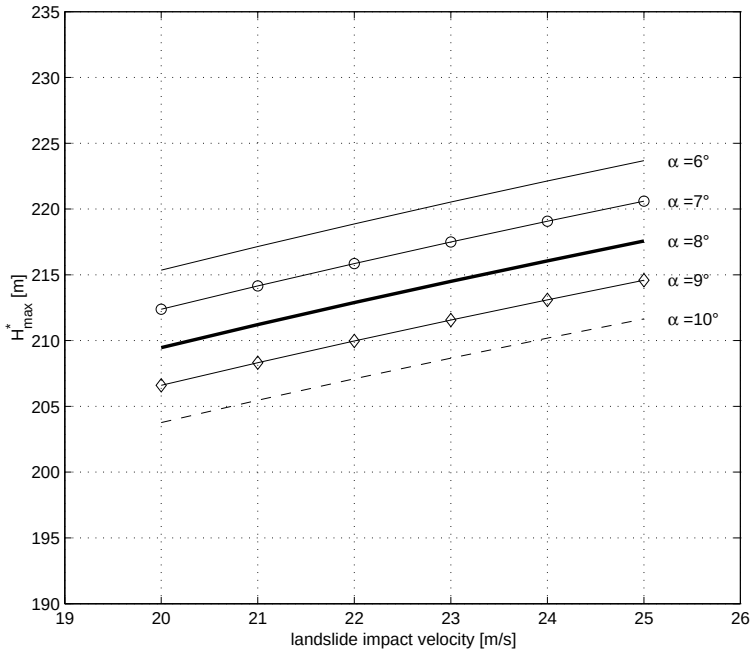

Figure 5.13: Estimated maximum wave height H_{max} generated by the 1963 event occurred at the Vajont reservoir.

Chapter 6

Conclusions and ongoing research

This work has introduced the characterization of subaerial landslide generated waves employing physical and numerical models.

Experiments carried out on a two dimensional model, which was realized in a wave flume, have been used to study the generated impulse waves applying the Wavelet Transform (WT) analysis of wave records. For the first time in literature, WT has been used to define impulse waves dispersive features while propagating in a two dimensional wave flume, recognizing different types of generated waves. The reflection coefficient from an overflow structure and seiche waves of the flume have been studied. Some of results were published in the paper "Application of wavelet transform analysis to landslide generated waves", Panizzo et al. (2002).

Experimental results from the three dimensional model have been analyzed in order to gain forecasting formulations, following two different strategies. The former, which is the classic regression approach, was used to define forecasting formulations relating the principal features of impulse waves with the experimental parameters of the landslide model kinematic and geometry. The latter, which is a Neural Network approach, was used to improve the correlation between the considered experimental parameters.
Forecasting formulations defined with the classic regression approach showed very satisfactorily correlations R^2 between observed and forecasted parameters. As far as the maximum generated wave height is concerned, it has been demonstrated that the dimensions of the landslide front play a predominant role, while impulse waves height considerably vary over directions and distances from the impact point. Highest waves are obtained with increasing the impact velocity v and decreasing the angle α of the sliding slope with the horizontal.
As far as ANN models are concerned, they present higher fits with experimental data if com-

pared to the classic regression approach. However, no information about the physics of the considered phenomenon can be provided using ANN models.
The comparison of obtained results with those presented by past studies show a substantial agreement with the work of Kamphuis and Bowering (1972), while some discrepancies exist with the work of Huber and Hager (1997). While Huber and Hager (1997) generated impulse waves in a three dimensional water body considering granular landslides, in the present work, with the aim of obtaining the highest possible effects, solid landslides with zero porosity have been considered in the physical model study. Contrarily to what expected, the application of Huber and Hager (1997) formulation to experimental data carried out in the present work showed marked overestimations of forecasted values, demonstrating the limits of Huber and Hager (1997) approach. The application of experimental formulations defined in the present work to case studies demonstrates that they can be used in real cases with a satisfactorily accuracy.
At present, the ongoing research involves physical experiments on a two dimensional model aiming at generating impulse waves and investigating the wave runup on sloped shorelines and the overtopping over artificial dams.

The SPH numerical model has been chosen to simulate subaerial landslide generated waves. In particular, a parallel version of the original SPH algorithm was implemented using the FORTRAN computer language. An original technique to solve the problem of the neighbors particles research has been proposed. The parallelization of the algorithm and the introduced technique for the neighbors research strongly reduce the computational time of the SPH model. The implemented code has been firstly tested using physical model experiments found in the literature, and then it has been applied to simulate two dimensional physical model experiments on subaerial landslide generated waves, which had been performed within the present work. Results demonstrate that SPH provides very satisfactorily simulations of the considered phenomenon.
At present a three dimensional version of the implemented SPH model is under construction, with the aim to gain direct simulations and reproduce possible real different scenarios.

Appendix A

Wavelet analysis

A.1 Fundamentals

In the present appendix, few details about the mathematical properties of the Wavelet Transform analysis are provided, focusing on the relationship between the wavelet and the Fourier transform, and the related energy density spectra. A detailed description of WT can be found in the works of Grossmann and Morlet (1984), Daubechies (1992), and Mallat (1992).
WT can be considered as an extension of the well known Fourier Transform (FT hereinafter). While FT considers basis functions (sines and cosines) defined in the frequency domain, WT is obtained by means of time and frequency localized basis functions.

For a given data signal $X(t)$ the FT is defined by:

$$\hat{X}(\omega) = \int_{-\infty}^{+\infty} X(t) e^{-i\omega t} dt \tag{A.1}$$

From this, the frequency energy spectrum can be obtained as:

$$S_X(\omega) = \frac{1}{\pi} \left| \hat{X}(\omega) \right|^2 \tag{A.2}$$

while total energy can be calculated using the Parseval relation:

$$E = \int_{-\infty}^{+\infty} X(t)^2 dt = \frac{1}{2\pi} \int_{-\infty}^{+\infty} \left| \hat{X}(\omega) \right|^2 d\omega = \int_0^{+\infty} S_X(\omega) d\omega \tag{A.3}$$

A WT analysis examines the characteristics of a function $X(t)$ in both the time and the frequency domain: this can be attained by a convolution of (A.1) with a windowing function $g(t)$, such that:

$$\hat{X}(\omega, \tau) = \int_{-\infty}^{+\infty} X(t) g(t - \tau) e^{-i\omega t} dt \tag{A.4}$$

By setting the lag time τ and the frequency ω as $a\tau_o$ and $b\omega_o$ respectively, the window function $g(t)$ can be rewritten as:

$$g_{ab}(t) = g(t - a\tau_0) e^{-ib\omega_0 t} \tag{A.5}$$

Note that the coefficients a and b, with $a > 0$ and $-\infty < b < +\infty$, are used respectively to shift in time and to scale in frequency the function $g(t)$. Once set the values of τ_o and ω_o, $g(t)$ is defined only as a function of a and b, and therefore can be replaced by the family of functions ψ_{ab}, called *wavelet*:

$$\psi_{ab}(t) = |a|^{-1/2} \psi\left(\frac{t-b}{a}\right) \tag{A.6}$$

ψ_{ab} are obtained by scaling a basic function $\psi(t)$, called the *motherwavelet*. In Eq. A.6 $|a|^{-1/2}$ is a normalization factor (Liu, 1999). In this optic, (A.4) is termed the wavelet transform of the time series:

$$\tilde{X}(a,b) = \int_{-\infty}^{+\infty} X(t) |a|^{-1/2} \psi^*\left(\frac{t-b}{a}\right) dt \tag{A.7}$$

The requirement to be a mother wavelet is the *admissibility condition*:

$$C_\psi = \int_{-\infty}^{+\infty} \frac{\left|\hat{\psi}(\omega)\right|^2}{|\omega|} d\omega < \infty \tag{A.8}$$

The function of the given data signal $X(t)$ can be obtained from the wavelet ψ_{ab} and the wavelet transform $\tilde{X}(a,b)$, as:

$$X(t) = \frac{1}{C_\psi} \int_{-\infty}^{+\infty} \int_{-\infty}^{+\infty} \tilde{X}(a,b) \psi_{ab}(t) \frac{dadb}{a^2} \tag{A.9}$$

Similarly to Fourier transform, the total energy of the signal is defined as (Daubechies, 1992):

$$E = \int_{-\infty}^{+\infty} X(t)^2 dt = \frac{1}{C_\psi} \int_{-\infty}^{+\infty} \int_{-\infty}^{+\infty} \tilde{X}(s,\tau) \tilde{X}^*(s,\tau) \, ds d\tau \tag{A.10}$$

while the wavelet spectrum is defined as:

$$W_X(s,\tau) = \frac{1}{C_\psi} \left|\tilde{X}(s,\tau)\right|^2 \tag{A.11}$$

The wavelet spectrum describes the energy of the time series over the time-frequency domain: its average over the time period of observation, corresponds to the Fourier spectrum defined by eq (A.2). Moreover, by substituting $t = t_0$ in eq (A.11), a slice of the wavelet spectrum is obtained, and presents an energy spectrum defined in the frequency domain at the fixed time t_0 .

In this study the wavelet analysis of wave records has been performed using the Morlet wavemother: the Morlet wavelet (see left panel of Figure A.1) is a plane wave modulated by a Gaussian, and is described by the following equation (Liu, 1999),

$$\psi_o(t) = \pi^{-1/4}(e^{-imt} - e^{-m^2/2})e^{-t^2/2} \tag{A.12}$$

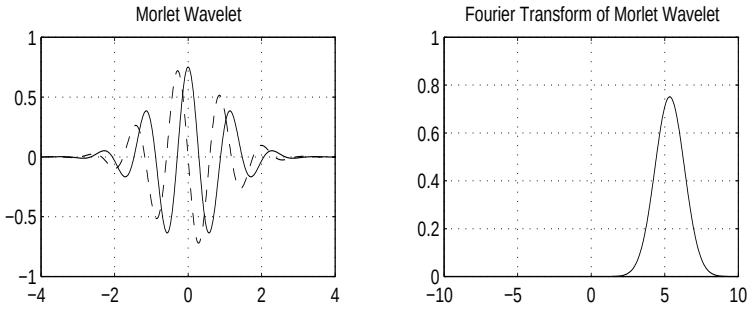

Figure A.1: Morlet wavelet and its Fourier transform

The Fourier transform of the Morlet wavemother (see right panel of Figure A.1) is defined by:

$$\hat{\psi}_0(\omega) = \pi^{-1/4}[e^{-(\omega-m)^2/2} - e^{-\left(-m^2+\omega^2\right)}] \tag{A.13}$$

where in this case $m = \pi\sqrt{2/\ln 2}$ is the basic frequency ω_0. Note that if m is chosen to be greater than 5, the second term in eq (A.13) becomes negligible: infact some authors present the Morlet wavelet as:

$$\psi_o(t) = \pi^{-1/4}(e^{-imt})e^{-t^2/2} \tag{A.14}$$

A.2 Wavelet Transform analysis of ocean wave records

Following the tips presented in the work of Torrence and Compo (1998), a code for the numerical computation of the Wavelet Transform analysis was implemented. In this application, water level oscillations recorded at the buoy station set off Pescara (Italy) have been considered. The buoy station is part of the Sea WAve measurement Network (SWAN), owned by the Italian National Hydrological and Marine Survey. The buoy takes 8 wave records a day, every 3 hours, with a sampling frequency equal to 1.28 Hz and a time window of 1000.0 s.
Figure A.2 presents the performed application of the WT analysis to ocean wave records. The top panel of the Figure reports the water level oscillations, and, in correspondence, the lower panel reports the WT power spectrum, which is plotted by means of contour lines of constant energy density. The right lower panel shows that the same information on the energy distribution over the frequency domain can be obtained analyzing both the FT spectrum and the time integrated WT power spectrum. It is clear that the time integrated WT energy spectrum presents a function which is smoother if compared to that of the FT spectrum, due to an acquired information of WT over the time domain. On the basis of the WT power spectrum, Liu (1999) introduced a practical criterion for the identification of group waves.

According to this criterion, it is sufficient defining a threshold level of the wavelet energy density (say f.i. 1/3 of the maximum value) to have a time-frequency localization of wave groups. Indeed, the left bottom panel of Figure A.2 plots the WT spectrum by means of lines of constant energy density, thus showing the time localization of wave groups. In this optic, it is straightforward defining the peak frequency, the energy, and the time window of each wave group.

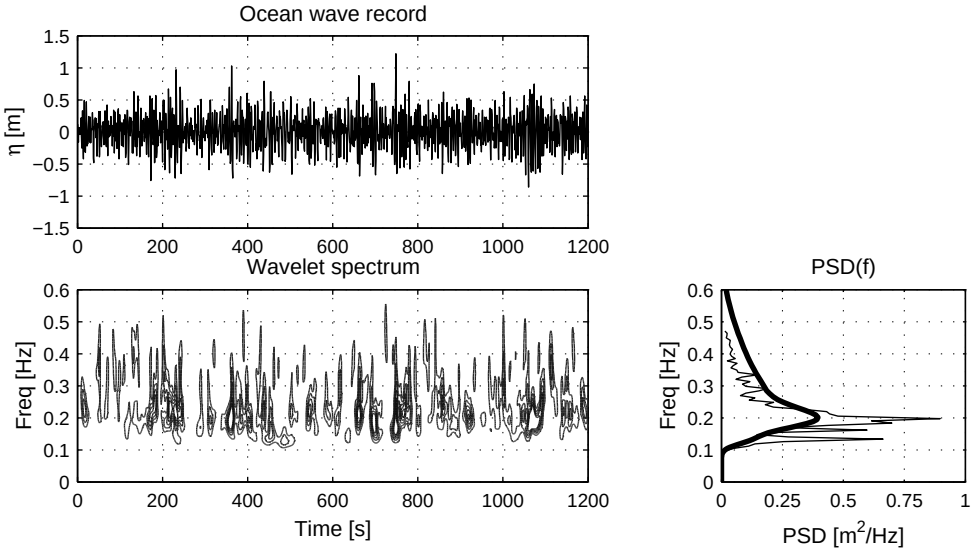

Figure A.2: Wavelet analysis of the water level oscillations recorded at the SWAN (Sea WAve measurement Network) buoy off Pescara the 26^{th} March, 1992. The upper panel shows the recorded wave signal. The lower left panel shows the wavelet power spectrum. The lower right panel shows both the Fourier power spectrum (thin line), and the time integrated wavelet power spectrum (thick line).

Appendix B

The Gauss Newton optimization method

Regression formulas between *input* and *output* vectors were defined employing firstly the classic regression technique, and then the Gauss-Newton method (also called the Newton-Raphson method). In this section few insights on the Gauss-Newton method are given. Let us consider a generic nonlinear regression model defined as:

$$Y_t = f\left(X_t, \tilde{\theta}\right) + \varepsilon_t \tag{B.1}$$

where $\tilde{\theta} = (\theta_1, \theta_2, \ldots, \theta_p)^T$ is the vector of parameters which are the model variable (which values are going to be optimized), $X_t\,(t = 1, 2, \ldots, n)$ are n vectors of the *input* variables, Y_t are the values of the *output* variable, and $\varepsilon_t\,(t = 1, 2, \ldots, n)$ are the errors of the model. The sum of the squares to be minimized is

$$S(\theta) = \sum_t \left[Y_t - f\left(X_t, \tilde{\theta}\right)\right]^2 \tag{B.2}$$

In order to simplify the notation, in the following $f\left(X_t, \tilde{\theta}\right)$ will be replaced by $f\left(\tilde{\theta}\right)$. The Jacobian matrix of the nonlinear model is defined as:

$$\mathbf{J}\left(\tilde{\theta}^*\right) = \left[\begin{array}{cccc} \frac{\partial f_1\left(\tilde{\theta}\right)}{\partial \theta_1} & \frac{\partial f_1\left(\tilde{\theta}\right)}{\partial \theta_2} & \cdots & \frac{\partial f_1\left(\tilde{\theta}\right)}{\partial \theta_p} \\ \vdots & & & \vdots \\ \vdots & & & \vdots \\ \frac{\partial f_n\left(\tilde{\theta}\right)}{\partial \theta_1} & \frac{\partial f_n\left(\tilde{\theta}\right)}{\partial \theta_2} & \cdots & \frac{\partial f_n\left(\tilde{\theta}\right)}{\partial \theta_p} \end{array}\right]_{\tilde{\theta}=\tilde{\theta}^*} \tag{B.3}$$

It is clear that the Jacobian matrix has dimensions p, being the number of parameters to be estimated, and n, being the number of available observation of the considered phenomenon.

By means of $\mathbf{J}$ it is possible to expand $f\left(\tilde{\theta}\right)$ in the Taylor series about a given $\tilde{\theta}_i$, and, if only the first two terms are retained, the approximation of the defined model is:

$$\tilde{f}\left(\tilde{\theta}\right) = \tilde{f}\left(\tilde{\theta}_i\right) + \mathbf{J}\left(\tilde{\theta}_i\right)\left(\tilde{\theta} - \tilde{\theta}_i\right) \tag{B.4}$$

with

$$\tilde{f}\left(\tilde{\theta}\right) = \left[f_1\left(\tilde{\theta}\right), f_2\left(\tilde{\theta}\right), \ldots, f_n\left(\tilde{\theta}\right)\right]^T \tag{B.5}$$

Considering the output vector as $\tilde{Y} = [Y_1, Y_2, \ldots, Y_n]^T$, it is possible to write the sum of squares as:

$$S\left(\theta\right) = \left[\tilde{Y} - \tilde{f}\left(\tilde{\theta}\right)\right]^T \left[\tilde{Y} - \tilde{f}\left(\tilde{\theta}\right)\right] \tag{B.6}$$

while introducing eq. B.4, it is possible to write

$$\begin{aligned} S\left(\theta\right) \cong & \left[\tilde{Y} - \tilde{f}\left(\tilde{\theta}_i\right)\right]^T \left[\tilde{Y} - \tilde{f}\left(\tilde{\theta}_i\right)\right] + \\ & - 2\left[\tilde{Y} - \tilde{f}\left(\tilde{\theta}_i\right)\right]^T \mathbf{J}\left(\tilde{\theta}_i\right)\left(\tilde{\theta} - \tilde{\theta}_i\right) + \left(\tilde{\theta} - \tilde{\theta}_i\right)^T \mathbf{J}^T\left(\tilde{\theta}_i\right)\mathbf{J}\left(\tilde{\theta}_i\right)\left(\tilde{\theta} - \tilde{\theta}_i\right) \end{aligned} \tag{B.7}$$

At this point, the optimum set of parameters $\tilde{\theta} = (\theta_1, \theta_2, \ldots, \theta_p)^T$ is that one minimizing the sum of squares defined by eq. B.7, and this can be obtained by setting the derivative of the function $S\left(\theta\right)$ equal to zero. The gradient vector of the sum of squares $g\left(\tilde{\theta}\right) = \left[\partial S/\partial\theta_1, \partial S/\partial\theta_2, \ldots, \partial S/\partial\theta_p\right]^T$ can be expressed on the basis of equation B.7 as:

$$g\left(\tilde{\theta}\right) = -2\mathbf{J}^T\left(\tilde{\theta}_i\right)\left[\tilde{Y} - \tilde{f}\left(\tilde{\theta}_i\right)\right] + 2\mathbf{J}^T\left(\tilde{\theta}_i\right)\mathbf{J}\left(\tilde{\theta}_i\right)\left(\tilde{\theta} - \tilde{\theta}_i\right) \tag{B.8}$$

By setting equation B.8 equal to zero and rearranging, we obtain the updated value of the parameter vector $\tilde{\theta}$, as:

$$\tilde{\theta}_{i+1} = \tilde{\theta}_i + \left[\mathbf{J}^T\left(\tilde{\theta}_i\right)\mathbf{J}\left(\tilde{\theta}_i\right)\right]^{-1}\mathbf{J}^T\left(\tilde{\theta}_i\right)\left[\tilde{Y} - \tilde{f}\left(\tilde{\theta}_i\right)\right] \tag{B.9}$$

In an iterative numerical scheme, the loop expressed by eq. B.9 stops when the following expression is satisfied:

$$f\left(\tilde{\theta}_{i+1}\right) - f\left(\tilde{\theta}_i\right) \leq e_r \tag{B.10}$$

begin e_r a given tolerance. So that, the Gauss-Newton method was applied to optimize the values of parameters involved in regression formulas forecasting impulse waves principal

features. It is to be stressed that the choice of the starting value $f\left(\tilde{\theta}_0\right)$ is a crucial point for the method convergence and success. In fact, the optimum set of parameters values which optimize the model is very close to the starting values. In the herein presented application, the method has been applied starting from parameters values defined using the classic multiple regression approach.

Bibliography

Batchelor, G. K. (1999). *An Introduction to Fluid Dynamics.* Cambridge University Press.

Belytschko, T., Y. Krongauz, J. Dolbow, and C. Gerlach (1998). On the completeness of meshfree particle methods. *Int. J. Numer. Mech. Engng. 43*, 785–819.

Bonet, J. and S. Kulasegaram (2002). A simplified approach to enhance the performance of smooth particle hydrodynamics methods. *Applied mathematics and comp,utations*, 135–155.

Bonet, J. and T. S. L. Lok (1999). Variational and momentum preservation aspects of smooth particle hydrodynamics formulations. *Comput. Methods Appl. Mech. Engrg.*, 97–115.

Caratto, M., E. Semenza, and M. Turrini (2002). Study of bank instability of the pontesei hydraulic reservoir (belluno province - n.e. italy.). In *Proceedings of the first European Conference on Landslides, Prague.*

Colagrossi, A. and M. Landrini (2003). Numerical simulation of interfacial flows by smoothed particle hydrodynamics. *Journal of Computational Physics*, 448–475.

Cruden, D. M. and D. J. Varnes (1996). *Landslide types and processes. In Landslides: Investigation and Mitigation.* Report 247, National Academy Press, Washington, D.C., 1996.

Dalrymple, R. A., O. Knio, D. T. Cox, M. Gesteira, and S. Zou (2001). Using a lagrangian particle method for wave overtopping. In *Proc. of WAVES 2001, ASCE.*

Datei, C. (2003). *Vajont, La storia idraulica.* Cortina, Padova 2003.

Daubechies, I. (1992). *Ten lectures on wavelets.* Society for industrial and applied mathematics, Philadelphia.

Gallati, M. and G. Braschi (2000). Simulazione lagrangiana di flussi con superficie libera in problemi di idraulica. *L'Acqua*, 7.

Gingold, R. and J. Monaghan (1977). Smoothed particle hydrodynamics: theory and application to non-spherical stars. *375–389 181.*

Gingold, R. and J. Monaghan (1983). On the fragmentation of Differentially Rotating Clouds. *715–733 204.*

Goda, Y. and Y. Suzuki (1976). Estimation of incident and reflected waves in random wave experiments. In *Proc. of 15th ICCE, ASCE*, pp. 828–845.

Grilli, S. and J. Horrillo (1997). Numerical generation and absorption of fully nonlinear periodic waves. *ASCE J. of Engineering Mechanics 123 (10)*, 1060–1069.

Grilli, S. T., R. Subramanya, I. A. Svendsen, and J. Veeramony (1994). Shoaling of solitary waves on plane beaches. *ASCE J. Waterway, Port, Coastal and Ocean Engng. 120 (6)*, 609–628.

Grossmann, A. and J. Morlet (1984). Decomposition of hardy functions into square integrable wavelet of constant shape. *SIAM J. Math. Anal.*, 723–736.

Hammack, J. (1973). A note on tsunamis: their generation and propagation in an ocean of uniform depth. *J. Fluid Mech. 60 (4)*, 769–799.

Heinrich, P. (1992). Nonlinear water waves generated by submarine and aerial landslides. *ASCE J. of Waterways, Port, Coastal and Oc. Eng. 118 (3)*, 249–266.

Hirt, C. W. and B. D. Nichols (1981). Volume of fluid (vof) method for the dynamics of free boundaries. *J. Comput. Physics*, 201.

Huber, A. (1982). Quantifying impulse wave effects in reservoirs. In *Commission internationale des grands barrages, Quatorzime Congrs des Grands Barrages, Rio de Janeiro.*

Huber, A. (1997). Quantifying impulse wave effects in reservoirs. In *Commission internationale des grands barrages, Dix-neuvime Congrs des Grands Barrages, Florence.*

Huber, A. and W. K. Hager (1997). Forecasting impulse waves in reservoirs. In *Commission internationale des grands barrages, Dix-neuvime Congrs des Grands Barrages, Florence*, pp. 993–1005.

Johnson, G., R. Stryk, and S. Beissel (1996). Sph for high velocity impact computations. *Comput. Methods Appl. Mech. Engrg. 139*, 347–373.

Kamphuis, J. W. and R. J. Bowering (1972). Impulse waves generated by landslides. In *Proc. of 12th ICCE, ASCE*, pp. 575–588.

Kranzer, H. C. and J. B. Keller (1960). Water waves produced by explosions. *Journal of applied physics*, 398–407.

Le Méhauté, B. and S. Wang (1996). *Water waves generated by underwater explosion.* World Scientific.

Levenberg, K. (1944). A method for the solution of certain problems in least squares. *Quart. Appl. Math.*, 164–168.

Li, S. F. and W. K. Liu (1996). Moving least squares galerkin methods (ii) fourier analysis. *Comput. Methods Appl. Mech. Engrg.*, 159–193.

Liu, P. (1999). *Wavelet transform and new perspective on coastal and ocean engineering data analysis. In Advances in coastal and ocean engineering.* World Scientific.

Liu, P.-F. and P. Lin (1997). A numerical model for breaking wave: the volume of fluid method. *Research Rep.CACR-97- 02 .Center for Applied Coastal Research,Ocean Eng.Lab., Univ.of Delaware,Newark,Delaware 19716*.

Liu, W. K., S. F. Li, and T. Belytschko (1997). Moving least squares galerkin methods (i) methodology and convergence. *Comput. Methods Appl. Mech. Engrg.*, 113–154.

Lucy, L. B. (1977). A numerical approach to testing the fission hypothesis. *December 82*(12), 1013–1924.

Mallat, S. (1992). *A wavelet tour of signal processing.* Academic Press, New York.

Marquardt, D. (1963). An algorithm for least-squares estimation of nonlinear parameters. *SIAM J. Appl. Math.*, 431–441.

Martin, J. C. and W. J. Moyce (1952). An experimental study of the collapse of liquid columns on a rigid horizontal plane. *Philos. Trans. R. Soc. London*, 244–312.

Massel, S. R. (2001). Wavelet analysis for processing of ocean surface wave records. *Ocean Engineering*, 957–987.

Monaghan, J. (1985). Particle methods for hydrodynamics. *Phys. Repts. 3*, 71–124.

Monaghan, J. (1994). Simulating free surface flows with sph. *J. Comp. Phys. 110*, 399–406.

Monaghan, J. and A. Kos (1999). Solitary waves on a cretan beach. *ASCE J. of Waterways, Port, Coastal and Oc. Eng. 125 (3)*, 145–154.

Monaghan, J. and A. Kos (2000). Scott Russell's wave generator. *Physics of Fluids 12*, 622–630.

Monaghan, J., A. Kos, and N. Issa (2003). Fluid motion generated by impact. *ASCE J. of Waterways, Port, Coastal and Oc. Eng. 129 (6)*, 250–259.

Morris, J. (1996). *Analysis of smoothed particle hydrodynamics with applications.* Ph. D. thesis, Monash University.

Morris, J. P., Y. Zhu, and P. J. Fox (1999). Parallel simulations of pore-scale flow through porous media. *Computers and Geotechnics*, 227–246.

Noda, E. (1970). Water waves generated by landslides. *ASCE J.Waterways, Harbours, and Coastal Engineering Division*, 835–855.

Panizzo, A., G. Bellotti, and P. De Girolamo (2002). Application of wavelet transform analysis to landslide generated waves. *Coastal Engng. 44-4*, 321–338.

Pezzoli, G. (1966). Sulla teoria delle onde d'emersione e di impulso. una soluzione rigorosa ad energia finita del problema di cauchy e poisson per moto piano (in italian). *Lincei - Rend. Sc. fis. mat. e nat.*, 660–669.

Pezzoli, G. (1972). Perturbazioni impulsive in bacini di profondit limitata (in italian). *Lincei - Rend. Sc. fis. mat. e nat.*, 903–911.

Prins, J. E. (1958). Characteristics of waves generated by a local disturbance. *Transactions, American Geophysical Union*, 865–874.

Randles, P. W. and L. D. Libersky (1996). Smoothed particle hydrodynamics: some recent improvements and applications. *Comput. Methods Appl. Mech. Engrg.*, 375–408.

Schlatter, B. (1999). *A Pedagogical Tool Using Smoothed Particle Hydrodynamics to Model Fluid Flow Past a System of Cylinders.* Ph. D. thesis, Dual MS Project, Oregon State University.

Selli, R. and L. Trevisan (1964). La frana del vajont. *Giornale di Geologia*.

Semenza, E. (2002). *La storia del Vaiont.* Tecomproject, Ferrara.

Shepard, D. (1968). A two dimensional function for irregularly spaced data. In *ACM National Conference*.

Stamos, D. G. and M. R. Hajj (2001). Reflection and transmission of waves over submerged breakwaters. *ASCE Journal of engineering mechanics.*, 99–105.

Stoker, J. J. (1957). *Water waves*. Interscience: New York.

Takeda, H., S. M. Miyama, and M. Sekiya (1994). Numerical simulation of viscous flow by smoothed particle hydrodynamics. *Prog. Theoretical physics*, 939.

Tinti, S., E. Bortolucci, and C. Romagnoli (1999). Modeling a possible holocenic landslide-induced tsunami at stromboli volcano, italy. *Phys. Chem. Earth*, 423–429.

Tinti, S., I. Gavagni, and A. Piatanesi (1994). A finite element numerical approach for modelling tsunamis. *Annali di Geofisica*, 193–212.

Tinti, S. and A. Maramai (1996). Catalogue of tsunamis generated in italy and in cote d'azur, france: a step towards a unified catalogue of tsunamis in europe. *Annali di geofisica*, 1253–1299.

Torrence, C. and G. P. Compo (1998). A practical guide to wavelet analysis. *Bulletin of the American Meteorological Society*, 61–78.

Walder, J. S., P. Watts, O. E. Sorensen, and K. Jannsen (2003). Tsunamis generated by subaerial mass flows. *Journal of Geophysical Research 108, B5*, 2236.

Watts, P. (1997). *Water waves generated by underwater landslides*. Ph. D. thesis, California Inst. of Tech., Pasadena, CA.

Watts, P. (1998). Wavemaker curves for tsunamis generated by underwater landslides. *ASCE J. of Waterways, Port, Coastal and Oc. Eng. 124*, 127–137.

Watts, P. (2000). Tsunami features of solid block underwater landslides. *ASCE J. of Waterways, Port, Coastal and Oc. Eng. 126*, 144–152.

Watts, P., F. Imamura, A. Bengston, and S. Grilli (2001). Benchmark cases for tsunamis generated by underwater landslides. In *Proc. Ocean Wave Measurements and Analysis - ASCE*, Volume 2, pp. 1505–1514.

Wiegel, R. L. (1955). Laboratory studies of gravity waves generated by the movement of a submarine body. *Trans. Am. Geophys. Union 36*(5), 759–774.

Wiegel, R. L., E. K. Noda, E. M. Kuba, D. M. Gee, and G. Tornberg (1970). Water waves generated by landslides in reservoirs. *ASCE J. of Waterways, Port, Coastal and Oc. Eng. ww2*(96), 307–333.